الجمهورية الجزائرية الديمقراطية الشعبية

PEOPLE'S DEMOCRATIC REPUBLIC OF ALGERIA

وزارة التعليم العالي و البحث العلمي

MINISTRY OF HIGHER EDUCATION AND SCIENTIFIC RESEARCH

جامعة أبو بكر بلقايد - تلمسان -

UNIVERSITY OF ABOU BAKR BELKAID - TLEMCEN -

FACULTY OF TECHNOLOGY

DEPARTMENT OF MECHANICAL ENGINEERING

MECHANICAL SYSTEMS AND MATERIALS ENGINEERING LABORATORY

A Thesis

Presented for obtaining the degree of:

DOCTORATE

In: Mechanical Engineering

Specialty: Mechanical and production manufacturing

By: **Besma KHOUANI**

Dynamic behavior of a Micro/Nano-beam made of smart piezoelectric material with property gradient

Comportement en dynamique d'une Micro/Nano-poutre en matériau piézoélectrique intelligent à gradient de propriété

Thesis defended on June 04, 2025 at Tlemcen in front of the jury composed of:

Mr Abdelmadjid CHEIKH	Full Prof	Univ Tlemcen	President
Mr Ahmed SAIMI	Associate Prof	Univ Ain Temouchent	Supervisor
Mr Ismail BENSAID	Associate Prof	Univ Tlemcen	Co-Supervisor
Mr Abdelkrim BOUKHALFA	Full Prof	Univ Tlemcen	Examiner
Mr Sidi Mohammed NADJIB SERDOUN	Associate Prof	ESSAT	Examiner

Academic Year 2025/2026

Dedication

It is with love, respect, and immense gratitude that I proudly dedicate this thesis to: To my beloved country, Algeria, the land of my roots and my heart. In tribute to my dear father Moussa, may the Almighty grant you His infinite mercy and welcome you into His eternal paradise. Your absence is always present in my heart. To the most precious treasure in my life, my dear mother Cherifa, in gratitude for your infinite love, your invaluable sacrifices, and your precious advice that has always guided me to success. I love you, Mom... You are a true diamond in the eyes of your children. To my dear aunt Rahma, you are like a second mother to me. I love you deeply. To my dear companion, confidante, and only sister Abia. This long journey has been made lighter and more enjoyable thanks to your presence and support. To my beloved brothers, Iheb and Redouane, models of tenacity, courage, and generosity, it is thanks to your brotherly support that I have been able to overcome obstacles. To my dear aunts Hadja Yamina, Halima, and her daughter Saliha, thank you for your constant presence and unwavering support. I love you very much and I wish you a life filled with health and happiness.

Besma KHOUANI

Acknowledgements

Firstly, all praise and thanks go to Allah who gave me the power and courage to conquer life challenges in general and to pursue my higher studies in particular; I am thankful. I would like to express my deep gratitude to my thesis supervisor, Dr. SAIMI Ahmed, and my co-supervisor, Dr. BENSAID Ismail, for the kindness, availability, and spontaneity with which you agreed to supervise this work. It has been a real honor to work under your guidance. I found much more than academic supervision: I found an attentive advisor, an enlightened guide, always present with kindness, a smile, and goodwill. Your scientific rigor, your exemplary professionalism, and your great human qualities command admiration and respect. You are, and will remain for me, a model of integrity and high standards in the exercise of your noble profession. Please accept, Sirs, through this modest work, the expression of my deep gratitude, my sincere esteem, and my most respectful thanks. I would also like to thank Pr. BOUKHALFA Abdelkrim, and SERDOUN Nadjib, for agreeing to be part of the thesis evaluation committee. I am honored by your presence. I would like to express my sincere gratitude to my colleague MAZARI Mohammed Yassine for his constant availability and spirit of collaboration. I would like to thank all the members of the IS2M laboratory, where I had the privilege of conducting most of my research, surrounded by a dynamic, committed, and warm team. Finally, I would like to express my deep gratitude to the director of the laboratory, Pr. CHEIKH Abedelmadjid, and his entire team for their invaluable collaboration, whose scientific support was essential to the completion of this research. I would also like to thank all those who, in one way or another, contributed to the completion of this thesis. To each and every one of you, I say: thank you from the bottom of my heart. To my family, who have always supported me and been my biggest source of strength, this accomplishment is equal to yours and mine. My academic career has been built on your unwavering support, and I will always be appreciative of that.

Abstract

This thesis investigates the static bending and free vibration of functionally graded magneto-electro-elastic (FG-MEE) microbeams in sandwich, coated, and bi-coated forms. Refined higher-order and quasi-3D beam theories are combined with the Differential Quadrature Finite Element Method (DQ-FEM) to capture electromechanical coupling. Material gradation is modeled by a power-law distribution, ensuring smooth property transitions between MEE and non-MEE layers. The Modified Couple Stress Theory (MCST) is incorporated to account for size-dependent effects, and governing equations are derived via Lagrange's theorem and Gauss–Lobatto discretization. Validation with published results confirms the model's accuracy and efficiency. Results show that material composition, gradation index, and geometry strongly affect static and dynamic responses. Increasing $BaTiO_3$ enhances piezoelectric deflection, while $CoFe_2O_4$ strengthens magnetostrictive effects. Higher gradation indices and slenderness ratios increase stiffness but reduce electromechanical potentials. Natural frequencies are highly sensitive to boundary conditions. The framework offers an efficient tool for optimizing FG-MEE microbeams in smart microsystems.

Keywords: FGMs; magneto-electro-elastic microbeams; higher-order beam theories; MCST; DQ-FEM.

Résumé

Cette thèse analyse la flextion statique et les vibrations libres de micro-poutres magnéto-électro-élastiques (FG-MEE) en configurations sandwich, revêtues et bi-revêtues. Des théories de poutres d'ordre supérieur et quasi-3D sont combinées à la méthode DQ-FEM pour modéliser le couplage électromécanique. La gradation est décrite par la loi de puissance assurant une transition continue entre matériaux MEE et non-MEE. La théorie des contraintes de couple modifiée (MCST) intègre les effets de taille, et les équations gouvernantes sont établies via le théorème de Lagrange et la discrétisation de Gauss–Lobatto. La validation confirme la précision et l'efficacité du modèle. Les résultats montrent que la composition, l'indice de gradation et la géométrie influencent fortement la réponse. L'augmentation du $BaTiO_3$ amplifie la flexibilité piézoélectrique, tandis que $CoFe_2O_4$ renforce les effets magnétostrictifs. Des indices plus élevés accroissent la rigidité mais réduisent les potentiels électromagnétiques. Les fréquences naturelles sont sensibles aux conditions aux limites. Ce cadre offre un outil efficace pour optimiser les microstructures FG-MEE.

mots-clés: FGM ; micro-poutres magnéto-électro-élastiques ; théories de poutres d'ordre supérieur ; MCST ; DQ-FEM.

مُلخّص

تتناول هذه الأطروحة دراسة الانحناء الساكن والاهتزاز الحر للعوارض الميكروية المغناطوكهربائيةمرنة المتدرجة وظيفياً (FG-MEE) ، وذلك ضمن تراكيب مختلفة تشمل العوارض الساندويتشية، والعوارض المطلية، والعوارض ثنائية الطلاء. ولتحقيق هذا الهدف، تم توظيف نظريات عوارض مطوّرة من الرتبة العليا ونظرية شبه ثلاثية الأبعاد (quasi-3D) ، ودمجها مع طريقة العناصر المتهية بالتربيع التفاضلي (DQ-FEM) من أجل تمثيل الاقتران الكهروميكانيكي بدقة وفعالية.

تم وصف تدرج الخواص المادية باستعمال قانون القدرة، بما يسمح بانتقال تدريجي وسلس للخصائص بين الطبقات المغناطوكهربائيةمرنة (MEE) والطبقات غير المغناطوكهربائيةمرنة. كما أُدرجت نظرية إجهاد العزم المعدّلة (MCST) لأخذ التأثيرات المعتمدة على الحجم بعين الاعتبار، وهي تأثيرات تصبح مهمة عند الأبعاد الميكروية. وقد تم اشتقاق المعادلات الحاكمة بالاعتماد على مبرهنة لاغرانج، مع استعمال تقطيع Gauss–Lobatto في الصياغة العددية.

تم التحقق من صحة النموذج من خلال مقارنة النتائج المتحصل عليها مع نتائج منشورة في الأدبيات، حيث أظهرت المقارنات دقة النموذج وكفاءته. وقد بينت النتائج أن تركيب المادة، ومعامل التدرج، والأبعاد الهندسية تؤثر بشكل واضح في الاستجابات الساكنة والديناميكية. فزيادة نسبة $BaTiO_3$ تؤدي إلى تعزيز الانحراف الناتج عن التأثير الكهروضغطي، في حين يساهم $CoFe_2O_4$ في تقوية التأثيرات المغناطوتمددية. كما أن ارتفاع معامل التدرج ونسبة النحافة يؤدي إلى زيادة الصلابة، لكنه يسبب في المقابل انخفاضاً في الكمونات الكهروميكانيكية. إضافة إلى ذلك، أظهرت النتائج أن الترددات الطبيعية شديدة الحساسية للشروط الحدية.

يوفر هذا الإطار العددي أداة فعالة لتحليل وتحسين العوارض الميكروية \textLR ذجييي الموجهة للاستعمال في الأنظمة الميكروية الذكية.

الكلمات المفتاحيّة: المواد المتدرجة وظيفياً (FGMs) ؛ العوارض الميكروية المغناطوكهربائيةمرنة؛ نظريات العوارض من الرتبة العليا؛ نظرية إجهاد العزم المعدّلة (MCST) ؛ طريقة العناصر المتهية بالتربيع التفاضلي (DQ-FEM) .

List of Publications

Journal Publications

1) Besma Khouani, Ahmed Saimi, Ismail Bensaid. "Bending and Vibration Analysis of Magneto-Electro Bilaterally Coated Quasi-3D Microbeam via DQ-FEM". ACTA MECHANICA ET AUTOMATICA, acta mechanica et automatica, vol.19 no.3 (2025). 337-349 (B-Rank, IF=1.1).

https://doi.org/10.2478/ama-2025-0041

2) Saimi Ahmed, Bensaid smail, Khouani Besma, Mazari Med Yassin, Houalef Ihab Eddine, Cheikh Abdelmadjid . (2023). A Novel Differential Quadrature Galerkin Method for Dynamic and Stability Behaviour of Bi-directional Functionally Graded Porous Micro Beams. European Journal of Computational Mechanics, 32(04), 393–440. (B-Rank, IF=0.6).

https://doi.org/10.13052/ejcm2642-2085.3244

3) Ahmed Saimi, Ismail Bensaid, Ömer Civalek, Besma Khouani, Abdelmadjid Cheikh. (2026). Bending and vibration analysis of refined higher-order magneto-electro bi-coated functionally graded microbeam via DQ-FEM. Archive of Applied Mechanics, Vol.96,No.4,Pages.73.

Table of Contents

Dedication **ii**

Acknowledgements **iii**

Abstract **iv**

List of Publications **vii**

Table of Contents **viii**

List of Figures **xii**

List of Tables **xix**

Preamble **1**

1 General Introduction 1

2 Objectives & Contributions 6

2.1 Primary Objectives 6

2.2 Original Contributions 7

3 Thesis Outline 9

3.1 Chapter I: General Information on Advanced Materials 9

3.2 Chapter II: Knowledge of Functionally Graded Materials 10

3.3 Chapter III: Piezoelectric and Piezomagnetic Materials in Microbeam Applications 10

3.4 Chapter IV: Beam Theory Formulation 11

3.5 Chapter V: Variational Formulation for Magneto-Electro Functionally Graded Microbeams based on a Quasi-3D Beam Theory 11

3.6 Chapter VI: Numerical Implementation using the Differential Quadrature Finite Element Method (DQ-FEM) 12

3.7 Chapter VII: Numerical Results and Discussion 12

I PART ONE: LITERATURE REVIEW **14**

Chapter I: General Information on Advanced Materials **15**

1 Introduction 16
2 General Information on Advanced Materials 16
3 Composite Materials 17
4 Piezoelectric Materials 17
5 Carbon Nanotubes 18
6 Functionally Graded Materials (FGM) 19
7 Micro- and Nano-Beams 19
7.1 Motivation and Applications 20
7.2 Scale Effects in Micro/Nano Beams 20
7.3 Coupling with Advanced Materials 21
8 Conclusion 21

Chapter II:Knowledge of functionally graded materials **23**

1 Introduction 24
2 Historical Development of Functionally Graded Materials 25
3 The Concept of FGMs 27
4 Application Domains of FGMs 28
4.1 Aerospace Domain 29
4.2 Automotive Industry 29
4.3 Biomedical Domain 30
4.4 Defense and Armor 30
5 Governing Laws for Property Variation in FGM Beams 31
5.1 The Exponential Law (E-FGM) 33
5.2 The Sigmoid Law (S-FGM) 33
5.3 The Power Law (P-FGM) 34
6 Conclusion 35

Chapter III:Piezoelectric and Piezomagnetic Materials in Microbeam Applications **37**

1 Introduction to Smart Materials: Piezoelectricity and Piezomagnetism . 38
2 Application of Piezoelectric and Piezomagnetic Materials in Microbeams 38
3 Functionally Graded Magneto-Electro-Elastic (MEE-FGM) Microbeams 39
4 Constitutive Equations for Transversely Isotropic Magneto-Electro-Elastic Materials 39
5 Conclusion 41

Chapter IV:Beam Theory Formulation **42**

1 Introduction . . . 43
2 Classical and First-Order Beam Theories . . . 44
2.1 Classical Beam Theory (CBT) . . . 44
2.2 Timoshenko Beam Theory (TBT) . . . 45
3 Higher-Order Shear Deformation Theories (HSDT) . . . 47
4 Refined Beam Theory (RBT) . . . 50
5 Quasi-3D Beam Theory (Q3D) . . . 51
6 Modified couple stress theory . . . 53
6.1 Review of the modified couple stress theory . . . 53
6.2 Modified couple stress models via EBT . . . 54
6.3 Modified couple stress models via TBT . . . 55
6.4 Modified couple stress models via RBT . . . 56
6.5 Modified couple stress models via HSDTs . . . 57
7 Conclusion . . . 61

II PART TWO: SCIENTIFIC CONTRIBUTIONS **62**

Chapter V:Variational Formulation for Magneto-Electro Functionally Graded Microbeams based on a Quasi-3D Beam Theory **63**

1 Introduction . . . 64
2 General formulation . . . 64
3 Magneto-Electro Functionally Graded Sandwich (MEFGS) Microbeams. 70
4 Magneto-Electro Bilaterally Coated Functionally Graded (MEBCFG) Microbeams. . . . 73
5 Magneto-Electro Bi-Coated Functionally Graded (MEBiCFG) Microbeams. . . . 74
6 Conclusion . . . 76

Chapter VI:Numerical Implementation using the Differential Quadrature Finite Element Method (DQ-FEM) **77**

1 Introduction . . . 78
2 Formulation of the DQ-FEM . . . 78
2.1 Differential Quadrature Approximation . . . 78
2.2 Weighting Coefficients . . . 79
2.3 Gauss–Lobatto Quadrature Rule . . . 79
2.4 Transformation Matrix and Nodal Relations . . . 80
3 Element Matrices . . . 80
4 Boundary Conditions . . . 86

5 Concluding Remarks 86

Chapter VII:Numerical results and discussion **87**

1 Introduction 88

2 Model Validation and Convergence Study 89

2.1 convergence analysis 89

2.2 validation 95

3 Parametric Analysis of the Sandwich MEE-FGM Microbeam 97

4 Parametric Analysis of the Bilaterally Coated MEE-FGM Microbeam . 110

5 Parametric Analysis of the Bi-Coated MEE-FGM Microbeam 122

General Conclusion **134**

References **137**

List of Figures

1 Conceptual illustration of the FGM solution: (a) A conventional laminated composite showing stress concentration and delamination at the sharp interface under a thermal gradient. (b) An FGM with a smooth property transition, enabling a much smoother stress distribution. 25

2 A timeline highlighting the key milestones in the historical development of Functionally Graded Materials, from the initial concept in the Japanese space program (1984) to global research expansion and diversification of applications. 27

3 A detailed schematic illustrating the FGM concept. The diagram shows the continuous change in microstructure and the corresponding smooth gradient in properties (e.g., Young's Modulus, Temperature) across the material's thickness. 28

4 Illustration of an FGM thermal barrier coating on a jet engine turbine blade, showing the gradient from a ceramic outer layer (resisting heat) to a metallic superalloy substrate (providing strength). 29

5 FGM based on copper–alumina composites for brake disc applications [90]. 29

6 Concept of an FGM hip implant, showcasing the gradient from a bioactive outer surface to a high-strength metallic core, designed to improve biocompatibility and mechanical performance. 30

7 Illustration of a projectile impacting an FGM armor plate. The diagram shows how the hard ceramic front face breaks up the projectile, while the graded and ductile rear layers absorb the kinetic energy. 31

8 FGM material Gradation. 32

9 Variation of an effective material property across the thickness of an E-FGM beam. 33

10 S-shaped distribution of the volume fraction in an S-FGM 34

11 Variation of the ceramic volume fraction V_c through the thickness of a P-FGM beam for different values of the power-law index p. 35

12 Kinematic assumption of Classical Beam Theory (Euler-Bernoulli), where a plane section remains plane and normal to the deformed neutral axis, implying zero transverse shear strain ($\gamma_{xz} = 0$). 44

13 Kinematic assumption of Timoshenko Beam Theory (First-Order Shear Deformation), where a plane section remains plane but is no longer normal to the deformed neutral axis, allowing for a constant transverse shear strain ($\gamma_{xz} \neq 0$). 46

14 Sandwich FG microbeam model with MEE core 70

15 MEBCFG microbeam model 73

16 MEBiCFG microbeam model 75

17 FG distribution pattern 75

18 Convergence of the 1st frequency for a simply supported ME bilaterally coated FG microbeam,$k = 1, h = 20\mu m, b = 2h, L = 20h, BaTiO_3(50\%) - CoFe_2O_4(50\%)$ 90

19 Convergence of the mid span deflection for a simply supported ME bilaterally coated FG microbeam,$k = 1, h = 20\mu m, b = 2h, L = 20h, BaTiO_3(50\%) - CoFe_2O_4(50\%)$ 90

20 Convergence of the mid span electric potential for a simply supported ME bilaterally coated FG microbeam,$k = 1, h = 20\mu m, b = 2h, L = 20h, BaTiO_3(50\%) - CoFe_2O_4(50\%)$ 91

21 Convergence of the mid span magnetic potential for a simply supported ME bilaterally coated FG microbeam,$k = 1, h = 20\mu m, b = 2h, L = 20h, BaTiO_3(50\%) - CoFe_2O_4(50\%)$ 91

22 Comparative analysis of the bending of a doubly S-S microbeam exposed to an even distribution of load 95

23 Comparative analysis of electrical potential of a doubly S-S microbeam exposed to an even distribution of load 96

24 Comparative analysis of magnetic potential of a doubly S-S microbeam exposed to an even distribution of load 96

25 Deflection of MEE sandwich microbeam with various boundary conditions,$k = 1, h = 20\mu m, b = 2h, L = 20h, (1{-}1{-}1), BaTiO_3(50\%) - CoFe_2O_4(50\%)$ 98

26 Electric potential of MEE sandwich microbeam with various boundary conditions,$k = 1, h = 20\mu m, b = 2h, L = 20h, (1{-}1{-}1), BaTiO_3(50\%) - CoFe_2O_4(50\%)$ 98

27 Magnetic potential of MEE sandwich microbeam with various boundary conditions,$k = 1, h = 20\mu m, b = 2h, L = 20h, (1{-}1{-}1), BaTiO_3(50\%) - CoFe_2O_4(50\%)$ 99

28 Simply supported sandwich microbeam midspan deflection with various thickness and MEE core material mixture percentage $BaTiO_3 - CoFe_2O_4$ ($k_z = 1, \quad b = 2h, \quad L = 20h, \quad (1 - 1 - 1)$) 103

29 Simply supported sandwich microbeam midspan Electric potential with various thickness and MEE core material mixture percentage $BaTiO_3 - CoFe_2O_4$ ($k_z = 1, \quad b = 2h, \quad L = 20h, \quad (1 - 1 - 1)$) 103

30 Simply supported sandwich microbeam midspan Magnetic potential with various thickness and MEE core material mixture percentage $BaTiO_3 - CoFe_2O_4$ ($k_z = 1, \quad b = 2h, \quad L = 20h, \quad (1 - 1 - 1)$) 104

31 Simply supported sandwich microbeam midspan deflection with various FG fraction index and MEE core material mixture percentage $BaTiO_3 - CoFe_2O_4$ ($h = 20\mu m, \quad b = 2h, \quad L = 20h, \quad (1 - 1 - 1)$) 105

32 Simply supported sandwich microbeam midspan Electric potential with various FG fraction index and MEE core material mixture percentage $BaTiO_3 - CoFe_2O_4$ ($h = 20\mu m, \quad b = 2h, \quad L = 20h, \quad (1 - 1 - 1)$) . . 105

33 Simply supported sandwich microbeam midspan Magnetic potential with various FG fraction index and MEE core material mixture percentage $BaTiO_3$ – $CoFe_2O_4$ ($h = 20\mu m$, $b = 2h$, $L = 20h$, $(1 - 1 - 1)$) 106

34 Electric potential at simply supported microbeam midspan with various FG fraction index and MEE inner material mixture percentage $BaTiO_3 - CoFe_2O_4$ ($h = 20\mu m$, $b = 2h$, $L = 20h$, $(1 - 1 - 1)$) . . 107

35 Magnetic potential at simply supported microbeam midspan with various FG fraction index and MEE inner material mixture percentage $BaTiO_3 - CoFe_2O_4$ ($h = 20\mu m$, $b = 2h$, $L = 20h$, $(1 - 1 - 1)$) . . 107

36 Deflection of MEE bilaterally microbeam with various boundary conditions ($k_z = 1$, $h = 20\mu m$, $b = 2h$, $L = 20h$, $BaTiO_3$ (50%)-$CoFe_2O_4$(50%) 110

37 Deflection of MEE bilaterally microbeam with CF boundary conditions ($k_z = 1$, $h = 20\mu m$, $b = 2h$, $L = 20h$, $BaTiO_3$ (50%)-$CoFe_2O_4$(50%) . . 111

38 Electric potential of MEE bilaterally microbeam with various boundary conditions ($k_z = 1$, $h = 20\mu m$, $b = 2h$, $L = 20h$, $BaTiO_3$ (50%)-$CoFe_2O_4$(50%) 111

39 Magnetic potential of MEE bilaterally microbeam with CF boundary conditions ($k_z = 1$, $h = 20\mu m$, $b = 2h$, $L = 20h$, $BaTiO_3$ (50%)-$CoFe_2O_4$(50%) 112

40 Simply supported microbeam midspan deflection with various thickness and MEE inner material mixture percentage $BaTiO_3$ – $CoFe_2O_4$ ($k_z = 1$, $b = 2h$, $L = 20h$,) 113

41 Electric potential at simply supported microbeam midspan with various thickness and MEE inner material mixture percentage $BaTiO_3$ – $CoFe_2O_4$ ($k_z = 1$, $b = 2h$, $L = 20h$,) 113

42 Magnetic potential at simply supported microbeam midspan with various thickness and MEE inner material mixture percentage $BaTiO_3$ – $CoFe_2O_4$ ($k_z = 1$, $b = 2h$, $L = 20h$,) 114

43 Simply supported microbeam midspan deflection with various FG fraction index and MEE inner material mixture percentage $BaTiO_3 - CoFe_2O_4\,(h = 20\mu m,\ \ b = 2h,\ \ L = 20h,)$ 115

44 Electric potential at simply supported microbeam midspan with various FG fraction index and MEE inner material mixture percentage $BaTiO_3 - CoFe_2O_4\,(h = 20\mu m,\ \ b = 2h,\ \ L = 20h,)$ 115

45 Magnetic potential at simply supported microbeam midspan with various FG fraction index and MEE inner material mixture percentage $BaTiO_3 - CoFe_2O_4\,(h = 20\mu m,\ \ b = 2h,\ \ L = 20h,)$ 116

46 Electric and magnetic potentials distribution of simply supported microbeam with $k_z = 5,\ \ h = 20\mu m,\ \ b = 2h,\ \ L = 20h,\ \ BaTiO_3\,(50\%) - CoFe_2O_4\,(50\%)$ 117

47 Electric and magnetic potentials distribution of clamped microbeam with $k_z = 5,\ \ h = 20\mu m,\ \ b = 2h,\ \ L = 20h,\ \ BaTiO_3\,(50\%) - CoFe_2O_4\,(50\%)$ 117

48 Electric and magnetic potentials distribution of clamped free microbeam with $k_z = 5,\ \ h = 20\mu m,\ \ b = 2h,\ \ L = 20h,\ \ BaTiO_3\,(50\%) - CoFe_2O_4\,(50\%)$ 118

49 Deflection with respect to length-thickness ratio of simply supported microbeam with $k_z = 5,\ b = 2h$ 119

50 Electric potential with respect to length-thickness ratio of simply supported microbeam with $k_z = 5,\ b = 2h$ 120

51 Magnetic potential with respect to length-thickness ratio of simply supported microbeam with $k_z = 5,\ b = 2h$ 120

52 Natural frequencies with respect to length-thickness ratio of simply supported microbeam with $k_z = 5,\ b = 2h$ 121

53 Deflection, electric potential and magnetic potential along the length of Simply supported microbeam with various FG fraction index and $50\% - 50\%\ BaTiO_3 - CoFe_2O_4\ (\ b = 2h,\ \ L = 20h)$ 123

54 Deflection, electric potential and magnetic potential along the length of clamped microbeam with various FG fraction index and $50\% - 50\%$ $BaTiO_3 - CoFe_2O_4$ ($b = 2h$, $L = 20h$) 124

55 Deflection, electric potential and magnetic potential along the length of clamped free microbeam with various FG fraction index and $50\% - 50\%$ $BaTiO_3 - CoFe_2O_4$ ($b = 2h$, $L = 20h$) 124

56 Simply supported microbeam midspan deflection, electric potential and magnetic potential with respect to the thickness, FG fraction index and $50\% - 50\%$ $BaTiO_3 - CoFe_2O_4$ ($b = 2h$, $L = 20h$) 125

57 clamped microbeam midspan deflection, electric potential and magnetic potential with respect to the thickness, FG fraction index and $50\% - 50\% BaTiO_3 - CoFe_2O_4$ ($b = 2h$, $L = 20h$) 126

58 Clamped free microbeam midspan deflection, electric potential and magnetic potential with respect to the thickness, FG fraction index and $50\% - 50\% BaTiO_3 - CoFe_2O_4$ ($b = 2h$, $L = 20h$) 126

59 Electric and magnetic potentials at simply supported microbeam midspan with various FG fraction index and $50\% - 50\% BaTiO_3 - CoFe_2O_4$ ($h = 20\mu m$, $b = 2h$, $L = 20h$) 130

60 Electric and magnetic potentials at clamped microbeam midspan with various FG fraction index and $50\% - 50\% BaTiO_3 - CoFe_2O_4$ ($h = 20\mu m$, $b = 2h$, $L = 20h$) 130

61 Electric and magnetic potentials at clamped microbeam midspan with various FG fraction index and $50\% - 50\% BaTiO_3 - CoFe_2O_4$ ($h = 20\mu m$, $b = 2h$, $L = 20h$) 131

62 Electric and magnetic potentials at simply supported microbeam midspan with various FG fraction index and MEE inner material mixture percentage $BaTiO_3 - CoFe_2O_4$ ($h = 20\mu m$, $b = 2h$, $L = 20h$) 131

63 Electric and magnetic potentials at clamped microbeam midspan with various FG fraction index and MEE inner material mixture percentage $BaTiO_3 - CoFe_2O_4$ ($h = 20\mu m$, $b = 2h$, $L = 20h$) 132

64 Electric and magnetic potentials at clamped free microbeam third-span with various FG fraction index and MEE inner material mixture percentage $BaTiO_3 - CoFe_2O_4$ $(h = 20\mu m, \quad b = 2h, \quad L = 20h)$ 132

List of Tables

1 Examples of warping functions $f(z)$ used in various HSDT beam theories. For comparison, the implied functions for CBT and FSDT are also included. 50

2 HSDT shape functions and corresponding displacement fields. 59

3 Q3D shape functions and corresponding displacement fields. 60

4 Material properties of $BaTiO_3 - CoFe_2O_4$ and epoxy. 89

5 Convergence results for the simply supported beam (SS) with respect to the number of sampling points N_s. 92

6 Convergence results for the clamped–clamped beam (CC) with respect to the number of sampling points N_s. 93

7 Convergence results for the clamped–free beam (CF) with respect to the number of sampling points N_s. 94

8 Comparison of numerical results ($b = 2h,\ L = 20h$), $50\% - 50\%$ $BaTiO_3$–$CoFe_2O_4$ 97

9 S–S sandwich microbeam midspan deflection with various layers thickness ratio and MEE core material mixture percentage $BaTiO_3$–$CoFe_2O_4$ ($h = 20\,\mu m,\ b = 2h,\ L = 20h$). 100

10 S–S sandwich microbeam midspan electric potential with various layer thickness ratios and MEE core material mixture percentage $BaTiO_3$–$CoFe_2O_4$ ($h = 20\,\mu m,\ b = 2h,\ L = 20h$). 101

11 S–S sandwich microbeam midspan magnetic potential with various layer thickness ratios and MEE core material mixture percentage $BaTiO_3$–$CoFe_2O_4$ ($h = 20\,\mu m,\ b = 2h,\ L = 20h$). 102

12 Natural frequency (MHz) of S–S sandwich MEE FG microbeam ($h = 20\,\mu m,\ b = 2h,\ L = 20h$). 108

13 Natural frequency (MHz) of S–S sandwich MEE FG microbeam ($h = 20\,\mu m,\ b = 2h,\ L = 5h$). 109

14 Natural frequency (MHz) of simply supported MEE FG microbeam ($b = 2h,\ \ L = 20h$) 122

15 Midspan deflection with various FG fraction index and MEE core material mixture percentage $BaTiO_3 - CoFe_2O_4$ ($h = 20\mu m,\ b = 2h,\ L = 20h$). 127

16 Midspan Electric potential with various FG fraction index and MEE core material mixture percentage $BaTiO_3 - CoFe_2O_4$ ($h = 20\mu m,\ b = 2h,\ L = 20h$). 128

17 Midspan Magnetic potential with various FG fraction index and MEE core material mixture percentage $BaTiO_3 - CoFe_2O_4$ ($h = 20\mu m,\ b = 2h,\ L = 20h$). 129

18 Natural frequency (MHz) with various FG fraction index and MEE core material mixture percentage $BaTiO_3 - CoFe_2O_4\,(h = 20\mu m,\ b = 2h,\ \ L = 20h,)$ 133

19 Natural frequency (MHz) with various FG fraction index and MEE core material mixture percentage $BaTiO_3 - CoFe_2O_4\,(h = 20\mu m,\ b = 2h,\ \ L = 5h,)$ 133

Preamble

1 General Introduction

Magneto-electro-elastic (MEE) materials have garnered widespread attention due to their multifunctional capabilities, which arise from the coupling of mechanical, electrical, and magnetic fields. These smart materials are integral to advanced engineering applications, including sensors, actuators, and energy harvesters. A thorough understanding of their mechanical behavior, particularly within microbeam structures, is crucial for optimizing their performance and reliability in practical applications [1, 2, 3, 4].

Further enhancing the capabilities of these materials, the concept of functionally graded materials (FGMs) allows for the continuous variation of material properties in specific directions. FGMs offer significant advantages such as enhanced thermal protection, sound insulation, and the absorption of energy and electromagnetic waves [5, 6]. The integration of MEE properties with functionally graded structures (MEE-FGMs) in thin beams and plates has become a prominent area of research. Bhangale and Ganesan [7] initiated work in this domain by investigating the free vibration of anisotropic and linear MEE-FGM plates. Subsequent research has explored various facets of these materials. Sladek et al. [8] proposed a meshless method for the bending analysis of circular MEE-FGM plates. Mahesh [9] examined the impact of porosity on the nonlinear deformation of MEE-FGM smart shells under combined loads. Zhang

et al. [10] analyzed the static bending and free vibration of transversely isotropic MEE beams by considering microstructure and foundation effects. Hong et al. [11] studied the bending and vibration of FG MEE Timoshenko microbeams and later extended this work to wave propagation analysis [12]. Qu et al. [13] developed a microstructure-dependent anisotropic MEE Mindlin plate model using a modified couple stress theory.

Experimental evidence has consistently shown that thin beams and plates exhibit size-dependent behavior, a phenomenon that classical continuum theories cannot predict at the micro and nano scales due to the absence of material length scale parameters [14, 15]. To address this, various non-classical continuum mechanics models have been developed. These include couple stress theories [16, 17, 18], strain gradient theories [19, 20, 21], and nonlocal elasticity [22]. These advanced theories have been instrumental in creating size-dependent structural models. For instance, nonlocal theories have been applied to develop MEE beam and plate models that capture non-local size effects [23, 24, 25, 26]. Furthermore, Lim et al. [27] introduced a nonlocal strain gradient theory that incorporates both nonlocal and strain gradient effects, which has been used to solve bending, buckling, and free vibration problems in FGM beams [28, 29].

Recent advancements continue to refine the understanding of size effects in MEE structures. Wang et al. [30] introduced an isogeometric model to investigate size-dependent effects in MEE microbeams, emphasizing the role of gradient index variations. Zheng et al. [31] performed a nonlinear bending analysis of nonlocal MEE laminated nanobeams, highlighting the influence of boundary conditions and external potentials. Alibeigi et al. [32] explored the thermal buckling of MEE nanobeams using von Kármán's nonlinear equations. Ghobadi et al. [33] investigated the nonlinear vibrations of

flexoelectric functionally graded nano-plates under a magnetic field. Extending this, Zheng et al. [34] analyzed the nonlinear deformations of MEE nanobeams on an elastic foundation using a modified couple stress theory. Habibi et al. [35] studied the free vibration of MEE nanobeams in a thermal environment. In the realm of buckling, Alibeigi and Tadi Beni [36] focused on size-dependent magneto-electromechanical buckling using strain gradient theory. Zheng et al. [37] analyzed the nonlinear postbuckling behavior of MEE laminated microbeams. Further contributions include the continuum-based model for functionally graded conical nano/microshells proposed by Fattaheian Dehkordi and Tadi Beni [38] and the nonlinear dynamic model for geometrically imperfect MEE nanobeams developed by Lyu and Ma [39]. Recent models, such as the axially functionally graded (AFG) micro-beam based on the reformulated strain gradient elasticity theory (RSGET), have been developed to analyze static and dynamic responses at the micro-scale [40]. Isogeometric analysis (IGA) has also been applied to MEE-FG microplates to study microstructure effects [41], and a new IGA model for MEE curved microbeams considers size effects through the modified couple stress theory (MCST) [30]. The importance of size effects is further underscored by studies on non-circular nanorods [42], functionally graded porous nanotubes [43, 44], and the influence of the flexoelectric effect [33, 45]. The profound impact of microstructure effects, nonlocal elasticity, and flexoelectricity on vibration, band gap formation, and stability has been demonstrated in various studies [46, 47]. Civalek et al. [48] also highlighted the nonlinear stability of perforated nanobeams. Further research has delved into the thermal vibration and stability of MEE FG porous nanobeams [49], 3D thermal wave propagation in sandwich nanoplates [50], and the behavior of three-layer curved nanobeams in thermal MEE environments [51].

To accurately model the behavior of such complex structures, various beam theories have been employed. These range from the first-order shear deformable beam theory (FSBT) and higher-order shear deformable beam theory (HSBT) to the more comprehensive quasi-3D (Q3D) theory. While FSBT is the simplest, it requires a shear correction factor [52, 53]. HSBTs were developed to improve the transverse shear stress distribution, thereby eliminating the need for a shear correction factor [54]. However, for thick functionally graded beams where normal strain and stretch effects are significant, Q3D theories that account for these effects are more appropriate [55, 56].

In recent decades, numerical and semi-numerical methods like the finite element method (FEM) and the generalized differential quadrature method (GDQM) have become popular for solving the complex differential equations associated with these structural elements. These methods offer efficiency, flexibility, and precision in handling complex geometries, interactions, and boundary conditions. For example, Bensaid and Saimi [57] used GDQM to study the dynamics of functionally graded porous beams on a viscoelastic foundation. Dahmane et al. [58] employed FEM to investigate the influence of cracks on the dynamic behavior of bidirectional imperfect FG beams. The differential quadrature finite element method (DQFEM) has been used to study the dynamics of on-board shafts [59] and the vibration and buckling of nano-composite beams [60]. Combined approaches, such as DQFEM with MCST, have been utilized to analyze the dynamic behavior of microbeams [61, 62].

Coated beams with piezoelectric and magneto-electro-elastic functionally graded materials are finding increasing use in applications requiring controlled vibration, energy harvesting, and precise actuation. These include smart

vibration damping in aerospace, energy harvesting in remote sensing devices, and structural health monitoring in critical infrastructure. However, many existing studies rely on simplified beam theories and do not fully account for the complex interactions in bi-coated structures at the microscale. Specifically, the integration of quasi-3D beam theories with robust numerical methods like DQ-FEM for bi-coated MEE-FG microbeams remains an underexplored area.

To address these research gaps, this study aims to develop a comprehensive model for a bi-coated, multidirectional functionally graded MEE microbeam. The model will incorporate microstructural effects using the modified couple stress theory (MCST) and will be analyzed using a quasi-3D beam formulation in conjunction with the DQ-FEM. This novel approach is expected to provide more accurate predictions of the bending and vibration behavior of advanced microbeam structures. The insights gained will be critical for the design and optimization of next-generation MEMS/NEMS devices, smart sensors, precision actuators, and energy harvesters that operate under coupled magneto-electro-mechanical fields.

2 Objectives & Contributions

Building upon the gaps identified in the existing literature, this research is motivated by the need for a more accurate, efficient, and comprehensive modeling framework for Magneto-Electro-Elastic Functionally Graded (MEE-FGM) microbeams. Current models often rely on simplified beam theories, neglect microstructural size effects, or are limited to simple geometries, thereby failing to capture the full complexity of the multi-field coupling behavior in advanced micro-devices.

The primary goal of this thesis is to develop and validate a high-fidelity computational model to predict the static and dynamic behavior of MEE-FGM microbeams with complex configurations. To achieve this overarching aim, the following specific objectives have been established:

2.1 Primary Objectives

1. **To Develop a Comprehensive Mathematical Framework:** To formulate a unified mathematical model for the analysis of MEE-FGM microbeams, specifically including sandwich and bi-coated configurations. The framework will fully account for the coupled magneto-electro-mechanical fields inherent to the material.
2. **To Integrate Advanced Continuum and Structural Theories:** To synergistically combine a refined, high-order shear deformable (or quasi-3D) beam theory with the Modified Couple Stress Theory (MCST). This integration is intended to simultaneously and accurately capture both macroscopic shear deformation and thickness stretching effects, as well as microscopic, size-dependent stiffening phenomena.
3. **To Implement an Efficient and Accurate Numerical Solution**

Scheme: To develop and apply a robust numerical code based on the Differential Quadrature Finite Element Method (DQ-FEM) to solve the complex system of coupled governing differential equations derived from the model. The focus will be on achieving high accuracy and computational efficiency compared to conventional numerical methods.

4. **To Validate the Proposed Model Rigorously:** To verify the accuracy, convergence, and reliability of the developed model by comparing its numerical predictions with established results from the literature for simplified cases, such as isotropic beams or structures where magneto-electric coupling or size effects are neglected.

5. **To Conduct a Comprehensive Parametric Investigation:** To utilize the validated model to perform a systematic analysis of the static bending and free vibration responses of MEE-FGM microbeams. This investigation will aim to elucidate the influence of key parameters, including:

   - The material property gradation index.
   - The microstructural length scale parameter.
   - The beam's slenderness (length-to-thickness) ratio.
   - Various boundary conditions.
   - The composition and thickness of coating/sandwich layers.

2.2 Original Contributions

The successful completion of these objectives will result in several original contributions to the field of computational solid mechanics and smart materials modeling. The principal contributions of this thesis are anticipated to be:

1. **A Novel, High-Fidelity Computational Model:** The development

of a new, unified computational tool capable of analyzing the complex electromechanical behavior of MEE-FGM microbeams with advanced sandwich and coated architectures. This model represents a significant advancement over existing formulations that are often limited to simpler, single-layer MEE beams.

2. **A More Physically Realistic Formulation for Micro-Scale Analysis:** The synergistic integration of a refined beam theory with the Modified Couple Stress Theory provides a more physically accurate representation of microbeam behavior. This contribution bridges the gap between macro-scale structural mechanics and micro-scale material physics, leading to more reliable predictions for MEMS design.

3. **Demonstration of a Computationally Superior Solution Method:** The successful application of the DQ-FEM to this class of complex, multi-physics problems will highlight its advantages in terms of accuracy and efficiency. This work will serve as a benchmark for the method's effectiveness in solving the coupled, higher-order differential equations that govern smart microstructures.

4. **New Benchmark Results and Design Insights:** The parametric studies will generate a new set of benchmark data for the bending and vibration of MEE-FGM microbeams, which are currently scarce in the literature. These results will not only serve as a reference for future researchers but will also provide critical design insights for engineers working on the optimization of micro-sensors, actuators, energy harvesters, and other MEMS/NEMS devices.

3 Thesis Outline

This thesis is organized into a general introduction, two main parts, and is concluded with a synthesis of the findings alongside recommendations for future research. The structure aims not only to provide the necessary theoretical foundation but also to highlight the novel scientific contributions in a logical progression.

- **Part One** establishes the theoretical and conceptual background. It consists of three chapters that review the state of knowledge on Functionally Graded Materials (FGMs), Piezoelectric and Piezomagnetic Materials, and Beam Theory Formulations. Together, these chapters create the framework upon which the original contributions of this thesis are built.
- **Part Two** focuses on the author's original contributions. It includes the development of a theoretical model, its numerical implementation, and an in-depth discussion of numerical results. This progression reflects the methodological path of the research, moving from modeling to computation and finally to interpretation.

3.1 Chapter I: General Information on Advanced Materials

- The discussion begins with an overview of advanced materials such as composites, piezoelectric materials, carbon nanotubes, and FGMs. These materials are chosen due to their growing importance in high-performance engineering applications.
- Special attention is given to micro- and nano-beams, as they serve as essential structural components in MEMS/NEMS technologies. Their relevance highlights both the motivation and the practical scope of this

study.

- The chapter further examines critical size-dependent phenomena (scale effects) that arise at micro- and nano-scales, stressing how these effects interact with advanced materials to generate unique mechanical responses.

3.2 Chapter II: Knowledge of Functionally Graded Materials

- This chapter provides a critical review of the origins, conceptual foundations, and application domains of FGMs. Their use in aerospace, automotive, biomedical, and defense industries demonstrates their versatility and significance.
- Mathematical formulations of property gradation are then presented, emphasizing three widely used models: the Exponential Law (E-FGM), the Sigmoid Law (S-FGM), and the Power Law (P-FGM). The discussion highlights how these gradation laws impact structural performance.

3.3 Chapter III: Piezoelectric and Piezomagnetic Materials in Microbeam Applications

- Attention shifts to smart materials, particularly piezoelectricity and piezomagnetism, which offer multifunctional capabilities in microbeam systems.
- The notion of Functionally Graded Magneto-Electro-Elastic (MEE-FGM) composites is introduced, underscoring their potential in coupling mechanical, electrical, and magnetic fields.
- To provide a rigorous basis, the constitutive equations of transversely isotropic MEE materials are discussed, capturing the coupled behavior essential for modeling advanced microbeam structures.

3.4 Chapter IV: Beam Theory Formulation

- A thorough review of beam theories is presented, moving from the classical models (CBT, TBT) to advanced formulations such as Higher-Order Shear Deformation Theories (HSDTs), Refined Beam Theories (RBT), and Quasi-3D (Q3D) approaches. Each theory is critically assessed in terms of its ability to capture deformation and stress distribution.
- The Modified Couple Stress Theory (MCST) is introduced as a key framework for incorporating size-dependent effects at micro-scales.
- The integration of MCST into different beam theories (EBT, TBT, RBT, HSDTs) is then explored, laying the foundation for the size-dependent models developed in the subsequent chapters.

3.5 Chapter V: Variational Formulation for Magneto-Electro Functionally Graded Microbeams based on a Quasi-3D Beam Theory

- The chapter begins with the application of variational principles to derive the governing equations of magneto-electro-elastic microbeam systems.
- Using a Quasi-3D formulation, detailed mathematical models are constructed for three configurations:
  1. Magneto-Electro Functionally Graded Sandwich Microbeams.
  2. Magneto-Electro Bilaterally Coated Functionally Graded Microbeams.
  3. Magneto-Electro Bi-Coated Functionally Graded Microbeams.
- This discussion emphasizes how each configuration captures different physical mechanisms and boundary-layer effects.

3.6 Chapter VI: Numerical Implementation using the Differential Quadrature Finite Element Method (DQ-FEM)

- The focus then turns to the numerical implementation. The rationale for adopting the DQ-FEM is first discussed, highlighting its efficiency and accuracy in solving high-order governing equations.
- The step-by-step implementation procedure is described for each microbeam configuration, covering discretization, interpolation, and the handling of coupled fields.
- The formulation of the elemental and global system matrices (mass, stiffness, and coupling terms) is presented, with attention to the role of boundary conditions in ensuring accurate solutions.

3.7 Chapter VII: Numerical Results and Discussion

- **Model Validation and Convergence Study:** The chapter begins with a convergence study to confirm the robustness of the DQ-FEM. Validation against published benchmarks ensures the credibility of the developed models.
- **Parametric Analysis of Sandwich MEE-FGM Microbeams:** The static and dynamic responses are investigated under varying material, geometric, and loading parameters.
- **Parametric Analysis of Bilaterally Coated MEE-FGM Microbeams:** The influence of external coatings is analyzed to understand their role in enhancing or modifying structural behavior.
- **Parametric Analysis of Bi-Coated MEE-FGM Microbeams:** The third configuration is examined in detail, followed by a comparative discussion across all three cases, synthesizing the main findings and trends.

General Conclusion and Future Work

- The thesis concludes by summarizing the major findings and highlighting the novel contributions to the modeling and analysis of advanced microbeams.
- The broader implications for the design and optimization of MEMS/NEMS devices are discussed, linking the theoretical framework to practical applications.
- Finally, the limitations of the present work are acknowledged, and concrete directions for future research are proposed, paving the way for further developments in the field.

Part I

PART ONE: LITERATURE REVIEW

Chapter I: General Information on Advanced Materials

Chapter II: Knowledge of Functionally Graded Materials

Chapter III: Piezoelectric and Piezomagnetic Materials in Microbeam Applications

Chapter IV: Beam Theory Formulation

Chapter I: General Information on Advanced Materials

1 Introduction

The last decades have witnessed remarkable progress in the development of advanced materials, which have been designed to meet the ever-increasing demands of engineering, biomedical, and defense applications. Unlike traditional materials such as steels and aluminum alloys, advanced materials are distinguished by their engineered microstructures, multifunctionality, and adaptability to extreme environments. These advances have been made possible thanks to progress in metallurgy, polymer science, nanotechnology, and processing techniques [63, 64].

Historically, the study of metals and alloys has been central to materials science. Henri Godfroid [63], in his seminal book Métallurgie pour mécaniciens (1950), outlined the fundamental properties of alloys and their heat treatments, laying the groundwork for the controlled modification of material performance. Later, B. Craig [65] discussed the limitations of alloying in steels and the critical role of hydrogen effects, emphasizing the importance of microstructural integrity in demanding environments. Similarly, Rajput [64], in Manufacturing Technology (2008), detailed industrial processes for shaping and treating materials, underscoring the link between processing and final performance.

The continuous search for materials that could outperform conventional alloys has resulted in the development of composites, smart materials, nanomaterials, and functionally graded materials (FGMs). These innovations have progressively expanded the application domains of materials science, from the aerospace sector to biomedicine and microelectronics.

2 General Information on Advanced Materials

Advanced materials can be defined as materials with superior or specifically tailored properties, designed for critical applications where conventional materials are inadequate. They can be metallic, ceramic, polymeric, or hybrid in nature, and they often integrate nanoscale or microscale engineering. Pantelakis and Alexopoulos [66] emphasized that lightweight aluminum alloys have been re-engineered to meet the stringent mechanical performance requirements in automotive and aerospace sectors. Their review highlighted how advanced wrought alloys provide improved fatigue life and mechanical stability.

What differentiates advanced materials from traditional ones is not only their higher strength-to-weight ratio but also their multifunctionality. Some, such as piezoelectric ceramics, combine sensing and actuation; others, like carbon nanotubes, simultaneously provide extraordinary electrical, thermal, and mechanical performance. This multifunctionality is particularly relevant in modern engineering, where one component is often expected to perform several functions at once.

3 Composite Materials

Composite materials represent one of the earliest and most impactful classes of advanced materials. They are defined as engineered combinations of two or more phases, typically a matrix and a reinforcement, that together provide superior performance. Early theories of composite mechanics were rigorously treated by Jones [67] in Mechanics of Composite Materials (1999), a cornerstone text in the field. Reddy [68], in his authoritative work Mechanics of Laminated Composite Plates and Shells, extended the analysis of composites to plates and shells, providing theoretical and analytical models for aerospace and structural applications.

The importance of composites lies in their design flexibility. Gibson [69] emphasized in Principles of Composite Material Mechanics (1994) that by adjusting fiber orientation, stacking sequence, and matrix properties, engineers can create materials tailored for stiffness, damping, or thermal resistance. Chen and Davalos [70], in a key article published in International Journal of Solids and Structures (2005), studied sandwich honeycomb structures, which have become essential in lightweight designs due to their excellent stiffness-to-weight ratio.

4 Piezoelectric Materials

Piezoelectric materials are smart materials that couple mechanical and electrical phenomena. They can sense deformations (acting as sensors) or generate deformations under an applied electric field (acting as actuators). Rao and Sunar [71], in a comprehensive survey in Applied Mechanics Reviews (1994), analyzed the role of piezoelectricity in disturbance sensing and control of flexible structures, marking a turning point in the integration of smart materials into engineering systems.

The growing interest in piezoelectric materials is further illustrated by the work of Lee, Zhang, Bar-Cohen, and Sherrit [72], who reviewed sensors and actuator

technologies in the journal Sensors (2014). Their study emphasized the versatility of piezoelectrics in applications ranging from aerospace to medical devices, where miniaturized and efficient sensing/actuation are critical.

Today, piezoelectric ceramics and polymers are extensively used in aerospace vibration suppression, biomedical ultrasound imaging, robotics actuation systems, and energy harvesting devices. Their ability to provide both mechanical and electrical functionality makes them indispensable in the development of next-generation smart structures.

Applications of composites span a wide range: from aerospace structures (aircraft fuselage, turbine blades) to civil engineering (bridges, buildings) and biomedical devices. Their success stems from their ability to combine the strengths of different materials while mitigating their individual weaknesses.

5 Carbon Nanotubes

The discovery of carbon nanotubes (CNTs) by Sumio Iijima in Nature (1991) [73] represented a revolution in nanotechnology. CNTs are cylindrical structures made of rolled graphene sheets, existing in single-wall (SWCNT) or multi-wall (MWCNT) forms. Their exceptional mechanical, thermal, and electrical properties have since attracted intense research attention.

Sandler et al. [74], in Composites Part A (2002), studied CNT-reinforced polyether ether ketone (PEEK) composites and demonstrated significant enhancements in stiffness and toughness. Gong et al. [75], in Chemistry of Materials (2000), proposed surfactant-assisted methods to improve CNT dispersion in polymer matrices, addressing one of the major challenges in nanocomposite fabrication.

Fundamental studies by Wong, Sheehan, and Lieber [76] in Science (1997) revealed the elasticity, strength, and toughness of nanorods and nanotubes, while Wang and colleagues [77, 78] investigated their torsional buckling and resonance phenomena. These works provided insights into the unique nanomechanical behavior of CNTs.

CNTs are currently being applied in nanocomposites, nanoelectronics, energy storage systems, sensors, and actuators, demonstrating their dual role as both structural reinforcements and functional nanoscale devices.

6 Functionally Graded Materials (FGM)

Functionally graded materials (FGMs) represent an innovative class of materials with gradually varying composition and properties across their volume. This concept was first developed in Japan during the 1980s for aerospace and nuclear applications, where materials needed to withstand extreme thermal gradients.

Suresh and Mortensen [79], in their pioneering monograph Fundamentals of Functionally Graded Materials (1998), outlined the processing routes and thermomechanical behavior of FGMs, focusing particularly on graded metals and metal-ceramic composites. Pindera, Arnold, Aboudi, and Hui [80] provided an extensive review in Composites Engineering (1994), examining the use of composites as precursors to FGMs and highlighting their potential in high-performance structures. More recently, Birman and Byrd [81], in Applied Mechanics Reviews (2007), synthesized modeling approaches and structural applications, providing a comprehensive framework for understanding FGM behavior.

FGMs address a major limitation of conventional laminated composites: the sharp material interface, which often leads to stress concentrations and delamination [67, 68]. By ensuring a smooth property transition, FGMs significantly improve durability and thermal resistance. Applications are found in:

- Aerospace: thermal barrier coatings in turbine blades and re-entry vehicles.
- Biomedical engineering: implants with graded porosity for enhanced biocompatibility.
- Defense: graded armor systems combining hardness and energy absorption.

7 Micro- and Nano-Beams

The rapid development of microelectromechanical systems (MEMS) and nanoelectromechanical systems (NEMS) has brought significant attention to the study of structural elements at small scales, particularly micro- and nano-beams. These beams, often fabricated from advanced materials such as silicon, carbon nanotubes (CNTs), or functionally graded composites, exhibit mechanical behaviors that differ fundamentally from their macroscale counterparts.

7.1 Motivation and Applications

Micro- and nano-beams are essential components in:

Sensors and actuators: for detecting pressure, acceleration, or chemical environments.

Resonators and oscillators: used in time-keeping devices and communication systems.

Energy harvesting devices: converting mechanical vibrations into electrical energy at micro/nano scales.

Biomedical devices: including drug delivery systems and microsurgical tools.

For instance, CNT-based nano-beams have demonstrated exceptional stiffness and unique vibrational properties [73]-[78], making them attractive in NEMS applications. Similarly, functionally graded micro-beams are increasingly studied for their ability to handle thermal gradients and complex boundary conditions.

7.2 Scale Effects in Micro/Nano Beams

Unlike conventional beams, micro- and nano-beams exhibit size-dependent effects. Classical continuum theories (such as Euler–Bernoulli or Timoshenko beam theory) often fail to predict their behavior accurately because they neglect small-scale phenomena. Researchers have introduced non-classical continuum theories to capture these effects, including:

Nonlocal elasticity theory (Eringen): accounting for long-range interatomic interactions.

Strain gradient theories: incorporating higher-order deformation gradients to describe size effects.

Surface elasticity models: recognizing that at small scales, surface stresses significantly influence the overall response.

Wong, Sheehan, and Lieber [76] were among the first to experimentally demonstrate that the elasticity and toughness of nanotubes could not be explained by classical theories, motivating the adoption of nonlocal models. Later works by Wang and collaborators [77, 78] studied buckling and resonance behaviors of CNT-based nano-beams, further confirming the necessity of size-dependent models.

7.3 Coupling with Advanced Materials

The integration of advanced materials into micro/nano-beam structures further enhances their functionality:

Composite micro-beams: offer high stiffness-to-weight ratios and can be tailored for specific frequencies.

Piezoelectric micro-beams: enable simultaneous actuation and sensing in MEMS devices [71, 72].

CNT-reinforced beams: provide superior mechanical and electrical properties, crucial for NEMS [74, 75].

FGM micro-beams: mitigate stress concentrations and improve thermal resistance, essential in harsh environments [79]-[81].

The synergy between advanced materials and small-scale beam structures has opened up a wide spectrum of applications in smart systems, nanotechnology, and energy-efficient devices.

8 Conclusion

This chapter has provided a comprehensive overview of advanced materials, tracing their evolution from classical metallurgy to contemporary composites, piezoelectrics, carbon nanotubes , and functionally graded materials . An additional section was dedicated to micro- and nano-beams, highlighting their fundamental importance in MEMS and NEMS technologies.

While composites have revolutionized lightweight structures, piezoelectric materials have introduced smart functionality. CNTs have bridged the gap between nanotechnology and materials science, while FGMs have resolved issues related to stress concentrations and material interfaces. Micro- and nano-beams represent the structural embodiment of these advanced materials at small scales, where size effects and multifunctionality converge.

This foundation prepares the ground for the detailed exploration of functionally graded porous beams and tubes under thermomechanical environments, which will be the focus of the subsequent chapters.

The unique adaptability of FGMs makes them a focal point in current research,

particularly in the design of structures exposed to coupled thermomechanical and dynamic environments.

Chapter II: Knowledge of functionally graded materials

1 Introduction

The relentless demand for high-performance materials capable of operating under severe thermo-mechanical loading conditions has consistently driven innovation in materials science. Traditional composite materials, such as laminates, have offered significant advantages in terms of strength-to-weight ratio and stiffness. However, their layered structure, characterized by abrupt interfaces between dissimilar materials, creates inherent weaknesses. These interfaces act as sites for stress concentration, often leading to delamination, micro-cracking, and catastrophic failure, particularly under large thermal gradients [82].

To overcome these fundamental limitations, a new class of advanced composites, known as Functionally Graded Materials (FGMs), was developed. An FGM is a spatially inhomogeneous material where the volume fractions of the constituent phases vary continuously and smoothly in one or more directions. This gradual transition, from a ceramic-rich surface to a metal-rich core, for instance, eliminates the problematic interfaces found in conventional composites. The result is a monolithic component with a smooth gradient in its mechanical, thermal, and electrical properties, tailored to meet specific functional requirements (figure 1). This chapter presents a comprehensive review of FGMs, tracing their historical origins, explaining their core concept, exploring their diverse application domains, and detailing the principal mathematical laws used to model their unique property variations [82].

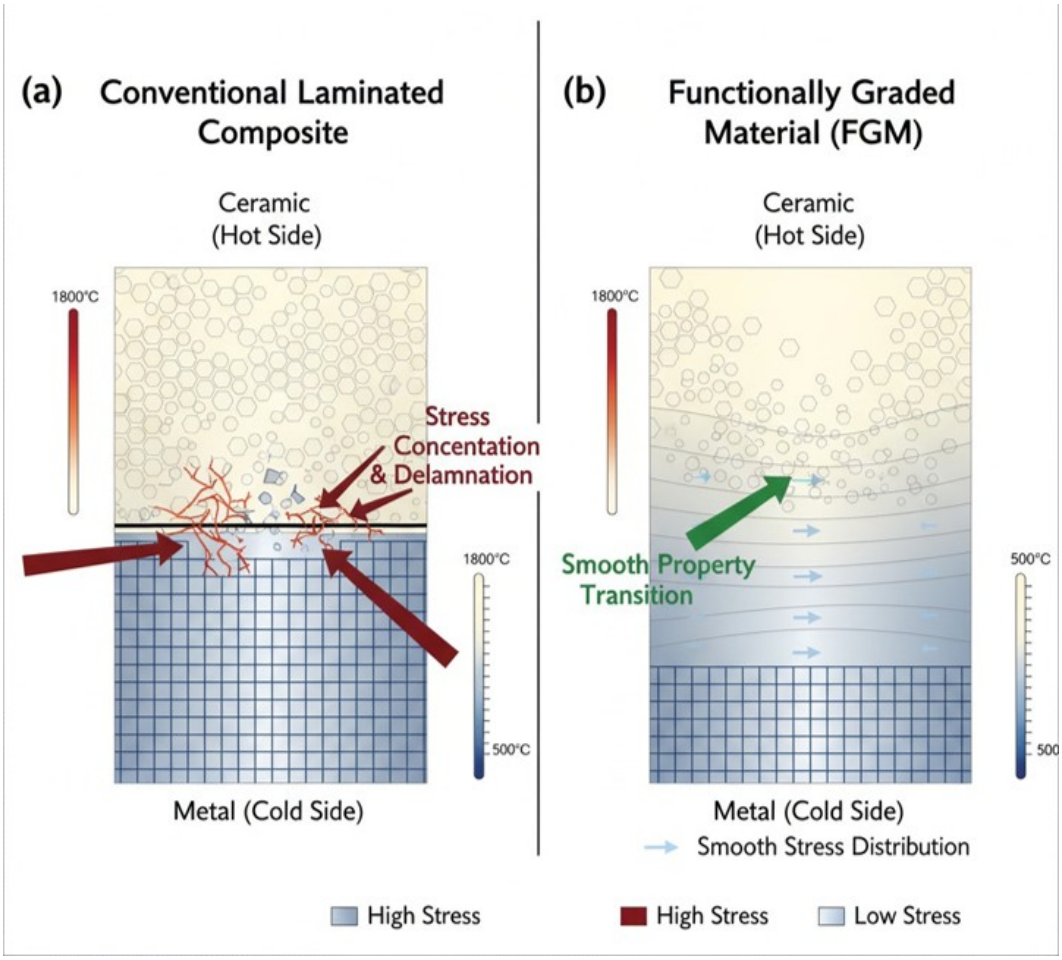


Figure 1: Conceptual illustration of the FGM solution: (a) A conventional laminated composite showing stress concentration and delamination at the sharp interface under a thermal gradient. (b) An FGM with a smooth property transition, enabling a much smoother stress distribution.

2 Historical Development of Functionally Graded Materials

The innovative concept of "Functionally Graded Materials" (FGMs) was born in 1984 at the Sendai National Aerospace Laboratory on Honshu Island, Japan [83, 84], through the work of M. Niino and his colleagues [85]. The initial idea was to engineer materials capable of serving as thermal barriers for space structures and fusion reactors. This new class of composite materials is characterized by continuous variations in composition, microstructure, and even porosity, which in turn create gradients in material properties like mechanical strength and thermal conductivity.The potential applications for these novel materials are vast, including thermal barrier coatings for ceramic engines, gas turbines, and optical thin films [86], (figure 2).

Recognizing the immense potential of this technology, the Japanese government

initiated a significant national project in 1987 titled, "Research on Basic Technology for the Development of Functionally Graded Materials and the Study of Thermal Stress Relaxation." The primary goal of this endeavor, which involved 17 national research laboratories, universities, and companies, was to develop materials with structured properties to act as thermal barriers in aerospace applications.[83, 84, 87]

The design of a material capable of withstanding a surface temperature of 1800°C and a temperature gradient of approximately 1300°C was guided by three key characteristics:

- High thermal resistance and oxidation resistance on the material's surface layer.
- Toughness on the lower-temperature side of the material.
- Effective relaxation of thermal stress throughout the material.

To achieve these demanding specifications, the foundational concept of FGM was to create a novel composite that capitalized on the properties of both ceramics (for the high-temperature side) and metals (for the low-temperature side). By the conclusion of the project's first phase (1987-1989), researchers had successfully produced small-scale experimental pieces, typically 1-10 mm thick and 30 mm in diameter. These samples demonstrated the ability to endure surface temperatures up to 2000K and a temperature gradient of 1000K. The fabrication of these materials with graded composition and structure was accomplished using four distinct techniques:

- Chemical vapor deposition (CVD) for the SiC/C system.
- Dry powder compaction for the PSZ/Mo system.
- High-temperature self-propagating synthesis for the TiB2/Cu system.
- Dual-torch plasma spraying for the (Ni-Cr-Al-Y)/(ZrO2-Y2O3) system.

The second phase of the project, from 1990 to 1991, focused on scaling up production to create larger parts with more intricate shapes than those developed in the initial phase [88].

Throughout the 1990s, the applications for FGMs expanded beyond high-temperature structural materials to include other fields such as biomechanics and optical sensor technology. This period saw the production of larger and more complex components for these new applications.

In 1992, significant advancements were made in enhancing the efficiency of FGMs in photoelectric, thermoelectric, and thermonuclear energy conservation [89]. These successes led to the launch of a new national project in 1993, known as "research on materials for energy conservation with the functional gradient structure plan," or "FGM Part II." This program, promoted by the Science and Technology Agency, aimed to apply FGM technology to improve the efficiency of various energy conservation methods, including solar, nuclear, photovoltaic, and thermoelectric energy.

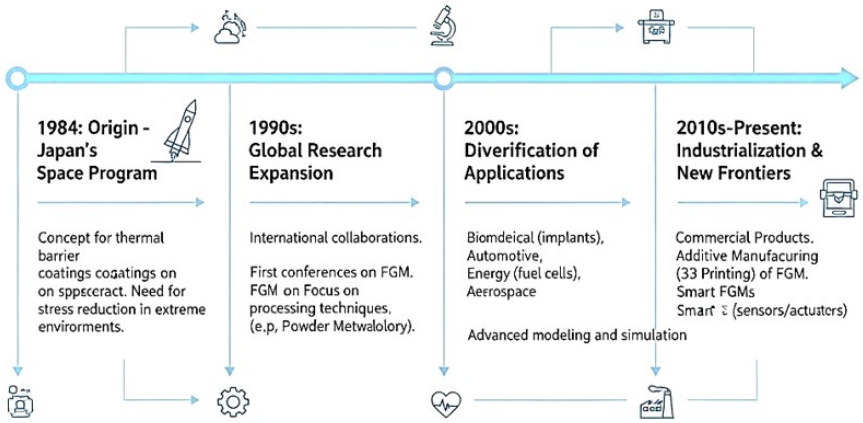


Figure 2: A timeline highlighting the key milestones in the historical development of Functionally Graded Materials, from the initial concept in the Japanese space program (1984) to global research expansion and diversification of applications.

3 The Concept of FGMs

The fundamental principle of an FGM lies in the deliberate engineering of its microstructure to produce a non-uniform macroscopic property distribution. Unlike homogeneous materials or composites with distinct phases, an FGM is a continuum of material properties. The transition between the constituent materials (e.g., a ceramic and a metal) is so smooth that no discrete interface exists. This eliminates interface-related failure modes and allows for the multifunctional optimization of a single component,(figure 3).

The key benefits derived from this graded concept are:

- **Stress Relaxation:** The primary advantage is the reduction of stress concentrations. In an FGM thermal barrier, the gradual change in the coefficient of thermal expansion (CTE) prevents the buildup of large internal thermal stresses.

- **Enhanced Bonding Strength:** The elimination of sharp interfaces leads to superior bonding and adhesion between the material constituents.
- **Tailored Functionality:** Properties like hardness, wear resistance, density, and thermal conductivity can be precisely controlled and located where they are most needed.
- **Improved Fracture Toughness:** The ductile metallic phase in a ceramic-metal FGM can act to arrest cracks that may initiate in the brittle ceramic phase, improving overall toughness and reliability.

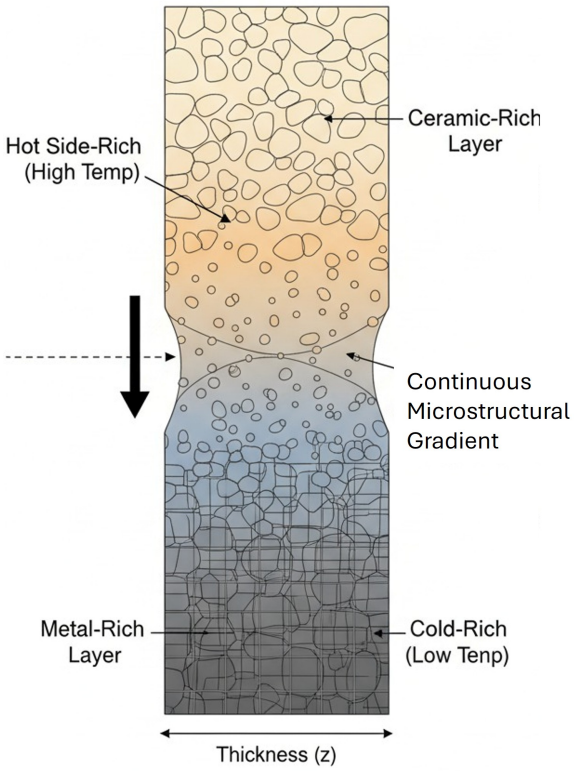


Figure 3: A detailed schematic illustrating the FGM concept. The diagram shows the continuous change in microstructure and the corresponding smooth gradient in properties (e.g., Young's Modulus, Temperature) across the material's thickness.

4 Application Domains of FGMs

The versatility and superior performance of FGMs have made them attractive for a wide array of high-technology applications.

4.1 Aerospace Domain

The aerospace industry remains the primary beneficiary of FGM technology. Applications include thermal barrier coatings (TBCs) on turbine blades and combustors, rocket nozzles, and leading edges of hypersonic vehicles. FGM TBCs provide superior protection against oxidation and high-temperature corrosion while minimizing thermal stresses, leading to longer component life and higher engine efficiency,(figure 4).

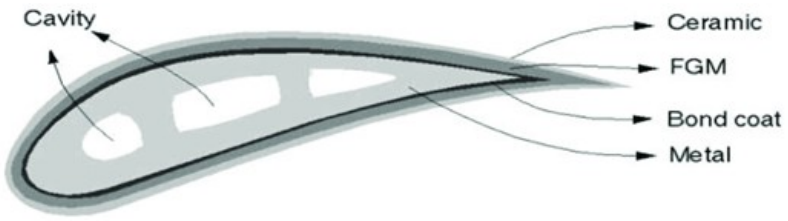


Figure 4: Illustration of an FGM thermal barrier coating on a jet engine turbine blade, showing the gradient from a ceramic outer layer (resisting heat) to a metallic superalloy substrate (providing strength).

4.2 Automotive Industry

In the automotive sector, FGMs are being explored for components that require high wear resistance and excellent thermal management. Examples include brake discs, pistons, valves, and cylinder liners. An FGM brake disc, for instance, could have a friction-resistant ceramic surface and a high-thermal-conductivity metal core to dissipate heat effectively, preventing brake fade and increasing durability,(figure 5).

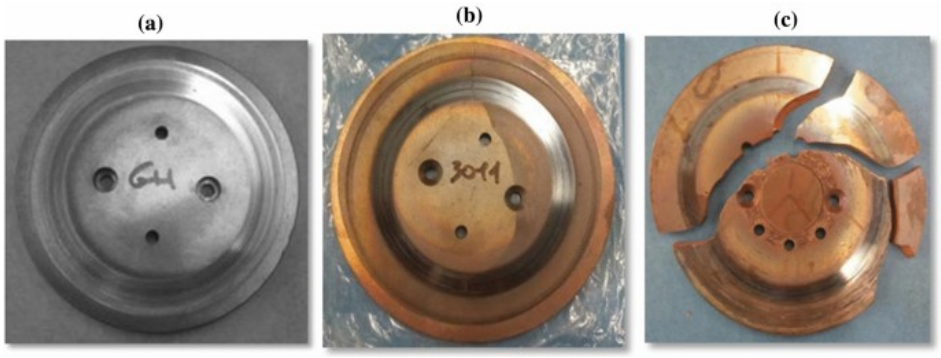


Figure 5: FGM based on copper–alumina composites for brake disc applications [90].

4.3 Biomedical Domain

FGMs offer revolutionary solutions for medical implants, such as orthopedic prostheses (hip and knee joints) and dental implants. The goal is to mimic the natural property gradients found in human bone. An FGM hip implant can feature a bioactive ceramic surface (like hydroxyapatite) to promote bone ingrowth (osseointegration), which transitions to a strong, inert metallic core (like titanium alloy) to bear physiological loads, reducing stress shielding and implant loosening,(figure 6).

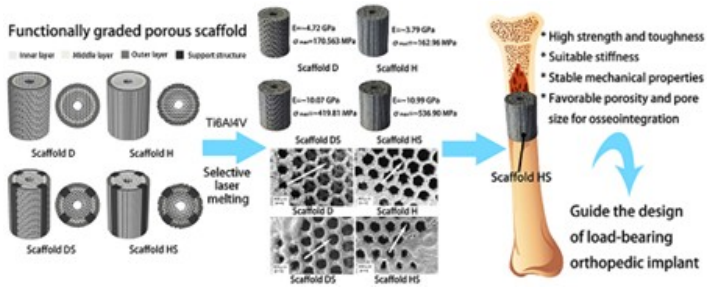


Figure 6: Concept of an FGM hip implant, showcasing the gradient from a bioactive outer surface to a high-strength metallic core, designed to improve biocompatibility and mechanical performance.

4.4 Defense and Armor

For defense applications, FGMs provide a promising avenue for developing next-generation armor systems with enhanced ballistic protection. An FGM armor plate can be designed with an extremely hard ceramic impact face that shatters incoming projectiles, followed by a graded layer that transitions to a tough, ductile metallic back plate. This configuration dissipates impact energy more effectively than traditional layered armor, offering superior protection at a lower weight,(figure 7).

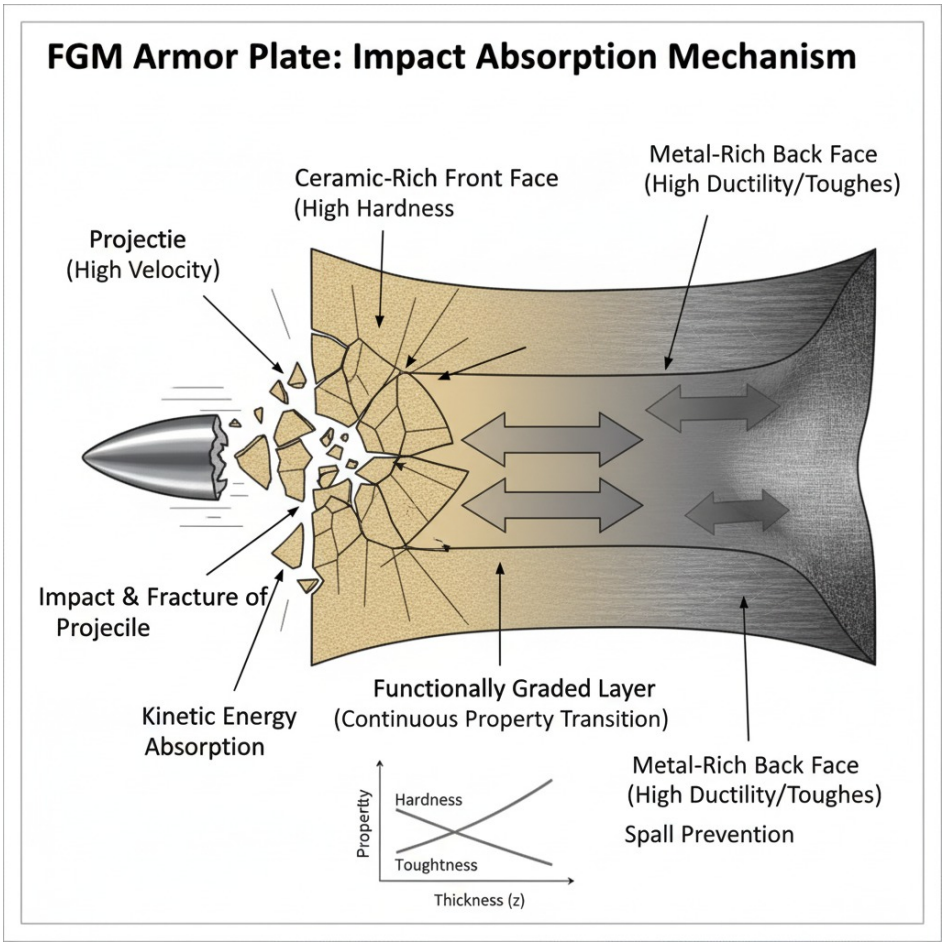


Figure 7: Illustration of a projectile impacting an FGM armor plate. The diagram shows how the hard ceramic front face breaks up the projectile, while the graded and ductile rear layers absorb the kinetic energy.

5 Governing Laws for Property Variation in FGM Beams

The exact gradation forms of FG material are not available. However, there are various mathematical laws that can be used to represent the volume fraction distribution in FG material. The material properties vary depending on the volume fraction distribution [91], which shows the continuously graded microstructure of an FG material. In the case of an FG shaft, the volume fraction varies in the radial direction [92], as shown in Figure 8.

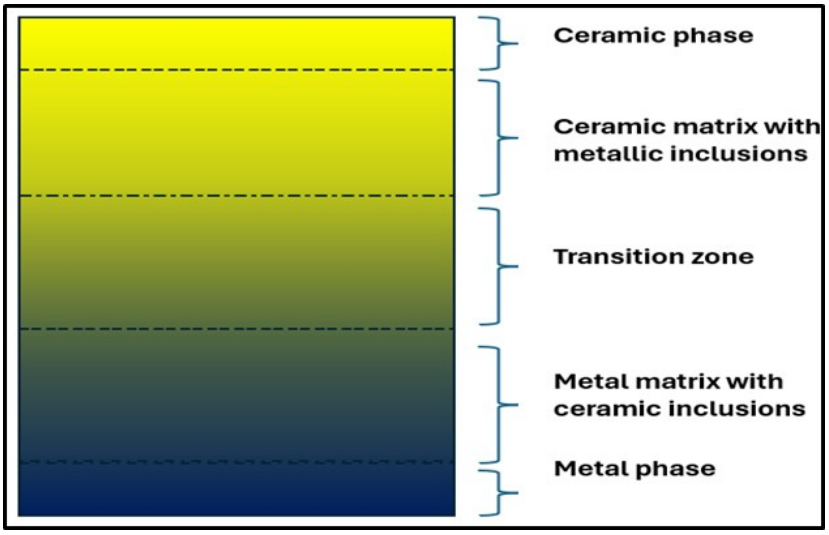


Figure 8: FGM material Gradation.

The first inner layer is composed solely of metal; as one moves towards the outer thickness direction, the fractional volume of the metal decreases and that of the ceramic increases. Thus, the outer layer is composed of 100% ceramic. The position dependence is obtained using the Voigt model, which provides a simple rule for composite materials. The material properties for each layer are expressed in equation 1:

To analyze and design FGM components, a mathematical description of the material property variation is required. The effective material property P at any point (e.g., Young's modulus E, Poisson's ratio ν, density ρ) is typically modeled as a function of the volume fractions of the constituent materials. The Voigt rule of mixtures is a common and simple approach:

$$P(z) = P_c V_c(z) + P_m V_m(z) \tag{1}$$

where subscripts c and m denote the ceramic and metal phases, respectively, and $V(z)$ is the volume fraction at a position z through the thickness. Since $V_c(z) + V_m(z) = 1$, the property can be written as $P(z) = (P_c - P_m)V_c(z) + P_m$. The following laws define the function $V_c(z)$.

Different mathematical models have been developed over the years by researchers to accurately predict the distribution. These include the power law, exponential law, and sigmoid law, which are the most widely used laws for grading FG materials. However, the majority of previous works have used power law grading in the case of FG microbeams.

5.1 The Exponential Law (E-FGM)

The Exponential Law describes a property distribution where the material changes rapidly at first and then more slowly as it approaches the pure constituent. This law can be more physically representative of certain diffusion-based fabrication processes. An effective property $P(z)$ for a plate of thickness h varying from a metal-rich bottom ($z = -h/2$) to a ceramic-rich top ($z = h/2$) can be modeled as:

$$P(z) = P_m e^{(\frac{1}{h}\ln(\frac{P_c}{P_m}))(z+\frac{h}{2})} \tag{2}$$

This formulation ensures that $P(-h/2) = P_m$ and $P(h/2) = P_c$. The exponential variation provides a smooth profile with non-zero property gradients at the boundaries.

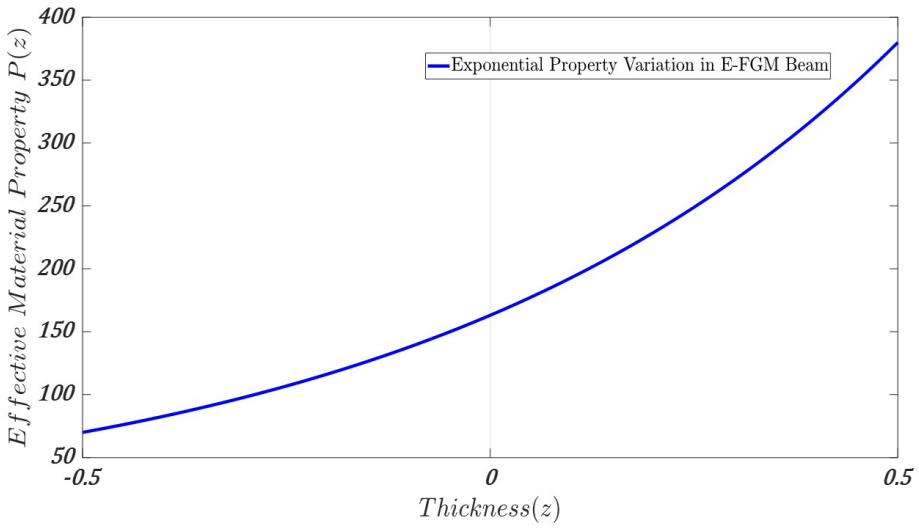


Figure 9: Variation of an effective material property across the thickness of an E-FGM beam.

5.2 The Sigmoid Law (S-FGM)

The Sigmoid Law (S-FGM) uses two power-law functions to create a smooth, S-shaped property distribution. This is useful for modeling FGMs with distinct surface layers that transition through a graded interlayer. For a plate of thickness h with pure metal at the bottom and pure ceramic at the top, the volume fraction of the ceramic phase $V_c(z)$ can be given by:

$$V_c(z) = \begin{cases} \frac{1}{2}\left(\frac{\frac{h}{2}+z}{\frac{h}{2}}\right)^k, & -\frac{h}{2} \le z \le 0, \\ 1 - \frac{1}{2}\left(\frac{\frac{h}{2}-z}{\frac{h}{2}}\right)^k, & 0 \le z \le \frac{h}{2}. \end{cases} \tag{3}$$

A more continuous form uses a logistic or hyperbolic tangent function, which provides a smooth transition centered around the mid-plane of the graded region. This allows for finer control over the start and end of the gradation.

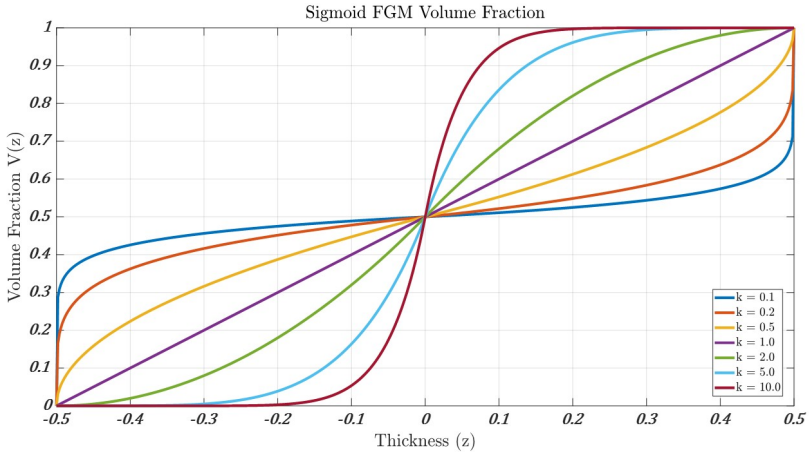


Figure 10: S-shaped distribution of the volume fraction in an S-FGM

5.3 The Power Law (P-FGM)

The Power Law is the most widely adopted and extensively studied model for FGMs due to its simplicity, versatility, and ease of integration into analytical and numerical solutions. It describes the volume fraction of one of the constituents as a power function of the spatial coordinate [93].

For a typical FGM plate of thickness h, where the coordinate z varies from the bottom surface ($z = -h/2$, pure metal) to the top surface ($z = h/2$, pure ceramic), the volume fraction of the ceramic phase, $V_c(z)$, is defined as:

$$V_c(z) = \left(\frac{z}{h} + \frac{1}{2}\right)^p, \quad \text{for} \quad p \geq 0 \tag{4}$$

Here, p is the **power-law index** or **material gradation index**, a dimensionless parameter that dictates the profile of the material variation through the thickness. The volume fraction of the metal phase is then simply $V_m(z) = 1 - V_c(z)$.

Substituting Eq. 4 into the rule of mixtures, any effective material property $P(z)$ can be expressed as:

$$P(z) = (P_c - P_m)\left(\frac{z}{h} + \frac{1}{2}\right)^p + P_m \tag{5}$$

The power-law index p provides significant control over the material distribution, as shown in Figure 11:

- **When $p = 0$:** The volume fraction $V_c(z) = 1$ for all z. The material is fully homogeneous ceramic.
- **When $p = 1$:** The volume fraction varies linearly from 0 at the bottom to 1 at the top. This represents a linear FGM.
- **When $0 < p < 1$:** The profile is convex. The material composition is metal-rich, with a rapid transition to ceramic near the top surface.
- **When $p > 1$:** The profile is concave. The material is predominantly ceramic-rich, with the transition to metal occurring rapidly near the bottom surface.
- **As $p \to \infty$:** The volume fraction $V_c(z)$ approaches 0 everywhere except at the very top surface ($z = h/2$). The material becomes effectively homogeneous metal.

This flexibility makes the P-FGM model an invaluable tool for parametric studies, allowing researchers to investigate how changes in the material gradation affect the mechanical, thermal, and vibrational behavior of FGM structures.

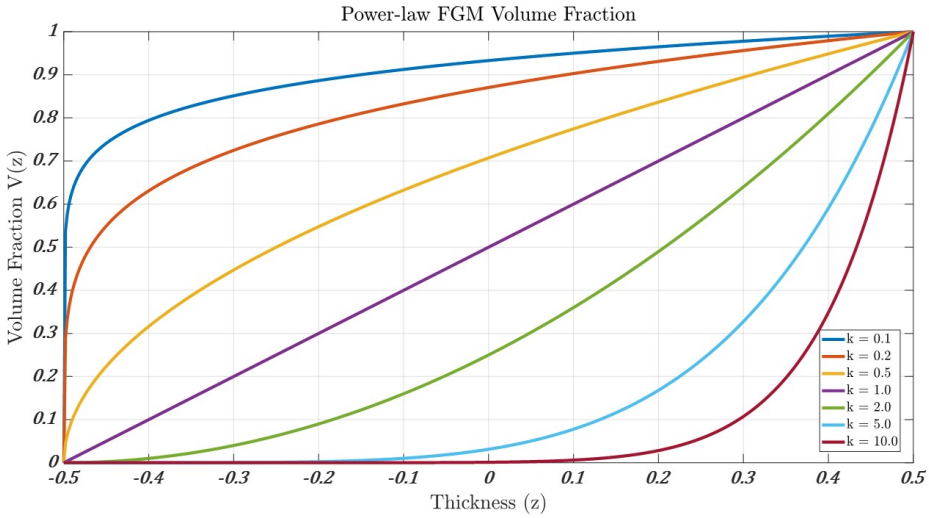


Figure 11: Variation of the ceramic volume fraction V_c through the thickness of a P-FGM beam for different values of the power-law index p.

6 Conclusion

Functionally Graded Materials represent a significant advancement in materials science, offering a sophisticated solution to the long-standing problem of interface failure in conventional composites. Born from the demanding requirements of the aerospace industry, the FGM concept—characterized by a continuous and smooth property gradient—has found diverse applications in fields ranging from biomedicine

to defense.

This chapter has provided a comprehensive overview of FGMs, covering their historical context, the core principles of their design, and their primary application domains. Furthermore, it detailed the key mathematical models used to describe their property variations, with a particular focus on the versatile and widely-used Power-Law model. This foundational understanding of FGM fabrication, concept, and modeling is essential for the advanced structural analyses that will be undertaken in the subsequent chapters of this thesis. The ability to mathematically control the material gradient is the first and most critical step in designing and optimizing the next generation of high-performance, multifunctional FGM structures.

Chapter III: Piezoelectric and Piezomagnetic Materials in Microbeam Applications

1 Introduction to Smart Materials: Piezoelectricity and Piezomagnetism

Smart materials form the cornerstone of modern sensing and actuation technologies, possessing the intrinsic ability to convert energy from one form to another. Among these, piezoelectric and piezomagnetic materials have garnered significant attention due to their unique electromechanical and magnetomechanical coupling behaviors. Piezoelectric materials exhibit a linear relationship between mechanical stress and electric polarization, while piezomagnetic materials demonstrate a similar coupling between mechanical stress and magnetization. This chapter explores the fundamental principles of these materials and their burgeoning applications in micro-scale structures, particularly microbeams. Functionally graded materials (FGMs) represent a significant advancement in material science, characterized by a continuous and gradual variation of material properties in one or more directions. This tailored gradation offers numerous advantages, including enhanced temperature resistance, improved sound insulation, and effective energy and electromagnetic wave absorption [5, 6]. The integration of piezoelectric and piezomagnetic phases within an FGM matrix has led to the development of magneto-electro-elastic functionally graded materials (MEE-FGMs), which are at the forefront of research in smart structures. Recent scientific endeavors have focused on evaluating the mechanical behavior of structures with laminated piezoelectric surfaces [94]. The study of MEE-FGMs in thin beams and plates has become particularly prominent in recent years, with researchers investigating their vibrational and bending characteristics.

2 Application of Piezoelectric and Piezomagnetic Materials in Microbeams

The unique properties of piezoelectric and piezomagnetic materials make them ideal candidates for integration into microbeam structures, serving as both sensors and actuators. These smart microbeams find applications in a diverse range of fields, including micro-electro-mechanical systems (MEMS), energy harvesting, and precision instrumentation. Early research into MEE-FGM structures includes the work of Bhangale & Ganesan [7] , who investigated the free vibration behavior of anisotropic and linear MEE-FGM plates. This foundational work paved the way for more complex analyses of smart micro and nano-scale structures. Khaje khabaz [94] later investigated the active optimal vibration control of a micro-beam with integrated piezoelectric

layers, considering small-scale effects through modified couple stress and surface stress elasticity theories. Further advancements in the field have been made by researchers such as Zhang [10], who analyzed the static bending and free vibration of a transversely isotropic MEE beam, incorporating microstructure and foundation effects. Hong [11] extended this research to study the bending and vibration of FG MEE Timoshenko microbeams, later adding wave propagation analysis to their work [12]. These studies highlight the critical role of material and geometric parameters in the performance of MEE microbeams.

3 Functionally Graded Magneto-Electro-Elastic (MEE-FGM) Microbeams

The concept of functionally graded materials has been revolutionary in the design of MEE structures. By gradually varying the volume fraction of the constituent piezoelectric and piezomagnetic phases, it is possible to tailor the material properties to meet specific application requirements. This allows for the optimization of the electromechanical and magnetomechanical coupling effects, as well as the overall structural response. Sladek [8] proposed a meshless approach for analyzing the bending of circular MEE-FGM plates, demonstrating the versatility of computational methods in handling the complex material properties of these structures. Mahesh [9] conducted an investigation into the effects of porosity on the nonlinear deformation characteristics of functionally graded magneto-electro-elastic smart shells under simultaneous loads, a critical consideration for the practical application of these materials. The influence of microstructure on the behavior of MEE structures has also been a key area of investigation. Qu [13] developed a microstructure-dependent anisotropic magneto-electro-elastic Mindlin plate model using a modified couple stress theory. This research underscores the importance of considering micro-scale phenomena in the accurate modeling of these advanced materials.

4 Constitutive Equations for Transversely Isotropic Magneto-Electro-Elastic Materials

To accurately model the behavior of MEE microbeams, it is essential to establish the constitutive equations that govern the coupled mechanical, electrical, and magnetic fields. For a transversely isotropic MEE material, where the properties are symmetric about an axis of rotation, the constitutive relations can be expressed as follows.

The stress tensor ($\boldsymbol{\sigma}$), electric displacement vector ($\mathbf{D}$), and magnetic induction vector ($\mathbf{B}$) are related to the strain tensor ($\boldsymbol{\varepsilon}$), electric field vector ($\mathbf{E}$), and magnetic field vector ($\mathbf{H}$) through a set of material property matrices. These equations form the basis for analyzing the response of MEE structures to external stimuli.

The equations representing transversely isotropic magneto-electro-elastic materials are given by:

Stress-Strain Relation

$$\begin{cases} \sigma_{11} = c_{11}\varepsilon_{11} + c_{12}\varepsilon_{22} + c_{13}\varepsilon_{33} - e_{31}E_3, \\ \sigma_{22} = c_{12}\varepsilon_{11} + c_{11}\varepsilon_{22} + c_{13}\varepsilon_{33} - e_{31}E_3, \\ \sigma_{33} = c_{13}(\varepsilon_{11} + \varepsilon_{22}) + c_{33}\varepsilon_{33} - e_{33}E_3, \\ \sigma_{23} = 2c_{44}\varepsilon_{23} - e_{15}E_2, \\ \sigma_{13} = 2c_{44}\varepsilon_{13} - e_{15}E_1, \\ \sigma_{12} = (c_{11} - c_{12})\varepsilon_{12}. \end{cases} \tag{6}$$

Electric Displacement-Strain Relation

$$\begin{cases} D_1 &= e_{15}\varepsilon_{13} + \kappa_{11}E_1, \\ D_2 &= e_{15}\varepsilon_{23} + \kappa_{11}E_2, \\ D_3 &= e_{31}(\varepsilon_{11} + \varepsilon_{22}) + e_{33}\varepsilon_{33} + \kappa_{33}E_3. \end{cases} \tag{7}$$

Magnetic Induction-Strain Relation

$$\begin{cases} B_1 &= m_{15}\varepsilon_{13} + \mu_{11}H_1, \\ B_2 &= m_{15}\varepsilon_{23} + \mu_{11}H_2, \\ B_3 &= m_{33}\varepsilon_{33} + \mu_{33}H_3. \end{cases} \tag{8}$$

Here, c_{ij} represents the elastic stiffness constants, e_{ij} are the piezoelectric constants, m_{ij} are the piezomagnetic constants, κ_{ij} are the dielectric permittivities, and μ_{ij} are the magnetic permeabilities. These equations, when coupled with the governing equations of motion and boundary conditions, provide a complete mathematical framework for the analysis of transversely isotropic MEE structures.

Zhang et al. [10] utilized these fundamental equations in their analysis of transversely isotropic MEE beams.

5 Conclusion

Piezoelectric and piezomagnetic materials, particularly when integrated into functionally graded structures, offer remarkable potential for the development of advanced microbeams with sensing and actuation capabilities. The continuous progress in material science and computational mechanics allows for increasingly sophisticated modeling and analysis of these complex MEE-FGM systems. The constitutive equations for transversely isotropic MEE materials provide the theoretical foundation for understanding and predicting the behavior of these smart structures. Future research in this field is expected to focus on the further refinement of material models, the exploration of novel applications, and the development of advanced manufacturing techniques for the fabrication of these intricate micro-scale devices. The works of Farajpour [1], Haghgoo [2], Sahmani [3], and Yakhno [4] are also relevant to this field, although their specific contributions could not be detailed in this chapter.

Chapter IV:
Beam Theory Formulation

1 Introduction

In structural mechanics and civil engineering, a beam is defined as a slender structural element whose length predominates over its transverse dimensions. This geometric characteristic allows for a simplified analysis of its mechanical behavior compared to an arbitrary three-dimensional solid body. Beam modeling, although simplified, applies to a wide range of engineering components, provided that certain geometric and loading assumptions are met. Beam theory constitutes a pillar of the strength of materials, providing an analytical framework for determining the stress and strain fields within these elements when subjected to external loads.

Beams are fundamentally three-dimensional structural elements, designed to support loads that primarily induce bending and buckling stresses. Nevertheless, for the purposes of analytical modeling, their geometry allows them to be idealized as one-dimensional elements. This approach, though approximate, proves to be effective and robust for studying the behavior of beams under transverse and axial loads.

The analysis of the mechanical behavior of beams, particularly concerning bending, vibration, and buckling, has been the subject of numerous scientific investigations. Several theories have been developed to model the deformation kinematics with varying degrees of precision. Among the most fundamental models are:

1. **The Euler-Bernoulli Beam Theory (EBT)**, which neglects the effect of shear [95]. It is based on the kinematic hypothesis that plane sections normal to the neutral axis before deformation remain so after deformation.
2. **The First-Order Shear Deformation Theory (FSDT)**, or Timoshenko Beam Theory (TBT), which accounts for the effect of shear by requiring a shear correction factor [96]. This model relaxes the hypothesis of the conservation of normality of the cross-section to the neutral axis.
3. **Higher-Order Shear Deformation Theories (HSDT)**, which account for the influence of shear more accurately, thereby avoiding the need for a shear correction factor. These notably include:
    - **The Third-Order Shear Deformation Theory (TSDT)**, such as Reddy's theory [97].
    - **The Sinusoidal Shear Deformation Theory (SSDT)**, developed by

Touratier [98].

- **The Exponential Shear Deformation Theory (ESDT)**, introduced by Karama et al. [99].

2 Classical and First-Order Beam Theories

2.1 Classical Beam Theory (CBT)

The earliest and simplest model is the Euler-Bernoulli Beam Theory, often referred to as Classical Beam Theory (CBT). Its development is attributed to the works of Jacob Bernoulli, Leonhard Euler, and Daniel Bernoulli in the 18th century. The core kinematic assumption of CBT is that plane sections, which are initially normal to the beam's neutral axis, remain plane and normal to the neutral axis after deformation [100]. This assumption implies that the effects of transverse shear deformation are neglected. Consequently, CBT is highly accurate for slender, homogeneous beams where bending is the dominant deformation mode, but it significantly overestimates stiffness and natural frequencies for thick or deep beams where shear effects become non-negligible.

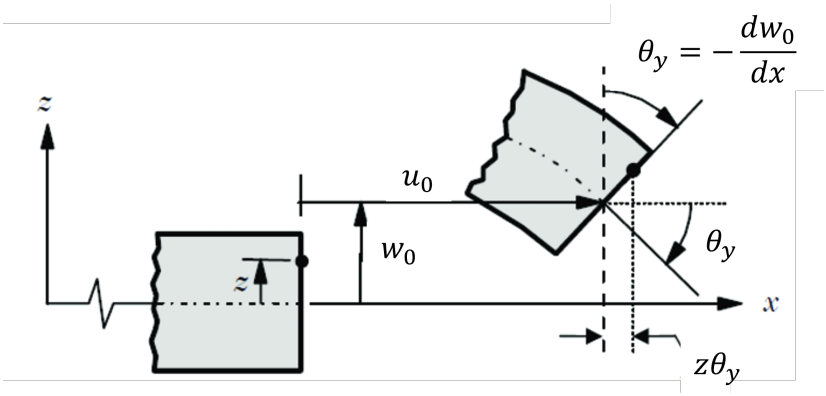


Figure 12: Kinematic assumption of Classical Beam Theory (Euler-Bernoulli), where a plane section remains plane and normal to the deformed neutral axis, implying zero transverse shear strain ($\gamma_{xz} = 0$).

Let us consider a beam with its longitudinal axis along the x-coordinate and its cross-section in the $y - z$ plane. For bending in the $x - z$ plane, the displacement field according to CBT can be derived from the kinematic assumptions. Let $u(x, z, t)$ be the displacement in the x-direction and $w(x, z, t)$ be the displacement in the z-direction. The assumption that the transverse displacement is constant through the thickness

implies:

$$w(x, z, t) = w_0(x, t) \tag{9}$$

where $w_0(x, t)$ is the transverse displacement of any point on the neutral axis ($z = 0$).

The assumptions that plane sections remain plane and normal to the deformed neutral axis mean that the axial displacement u is a linear function of z. The rotation of the cross-section is equal to the slope of the deflected neutral axis, $\theta_y(x, t) = \frac{\partial w_0(x,t)}{\partial x}$. Therefore, the axial displacement at a distance z from the neutral axis is given by:

$$u(x, z, t) = -z\theta_y(x, t) = -z\frac{\partial w_0(x, t)}{\partial x} \tag{10}$$

The complete displacement field for CBT is thus:

$$u(x, z, t) = -z\frac{\partial w_0(x, t)}{\partial x} \tag{11}$$

$$w(x, z, t) = w_0(x, t) \tag{12}$$

2.2 Timoshenko Beam Theory (TBT)

To account for transverse shear deformation, Stephen Timoshenko proposed a more refined theory in the early 20th century, now known as Timoshenko Beam Theory (TBT) or First-Order Shear Deformation Theory (FSDT) [96] . TBT relaxes the normality assumption of CBT, allowing plane sections to remain plane but not necessarily normal to the neutral axis after deformation. This is achieved by introducing an independent rotation of the cross-section, $\phi_y(x, t)$, which is not directly tied to the slope of the neutral axis $\frac{\partial w_0}{\partial x}$. While this correctly captures the first-order effects of shear, it assumes a constant shear strain through the thickness, which violates the zero-traction boundary conditions on the top and bottom surfaces of the beam. To correct for this, a *shear correction factor* is required, which depends on the cross-section's geometry and material properties.

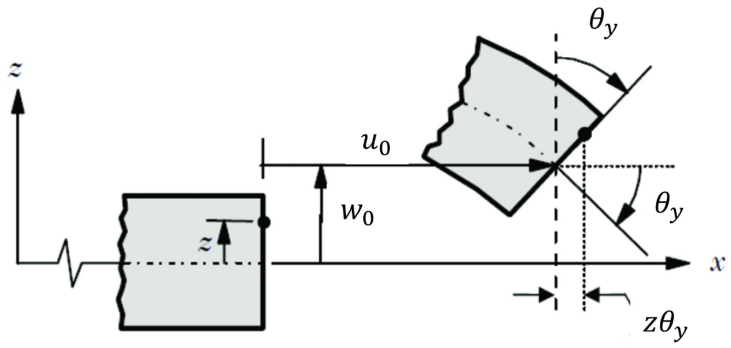


Figure 13: Kinematic assumption of Timoshenko Beam Theory (First-Order Shear Deformation), where a plane section remains plane but is no longer normal to the deformed neutral axis, allowing for a constant transverse shear strain ($\gamma_{xz} \neq 0$).

In TBT, the axial displacement u is still assumed to be linear with respect to z, but it is now a function of the independent rotation $\theta_y(x,t)$:

$$u(x,z,t) = -z\theta_y(x,t) \tag{13}$$

The transverse displacement remains a function of x only:

$$w(x,z,t) = w_0(x,t) \tag{14}$$

The complete displacement field for TBT is thus defined by two independent variables, w_0 and θ_y:

$$u(x,z,t) = -z\theta_y(x,t) \tag{15}$$

$$w(x,z,t) = w_0(x,t) \tag{16}$$

The strain components are derived accordingly. The axial strain ϵ_{xx} is:

$$\epsilon_{xx} = \frac{\partial u}{\partial x} = -z\frac{\partial \theta_y(x,t)}{\partial x} \tag{17}$$

Unlike in CBT, the transverse shear strain γ_{xz} is non-zero:

$$\gamma_{xz} = \frac{\partial u}{\partial z} + \frac{\partial w}{\partial x} = -\theta_y(x,t) + \frac{\partial w_0(x,t)}{\partial x} \tag{18}$$

This shear strain is constant through the thickness, which is a key feature and limitation

of TBT. The constitutive relations for an isotropic material are:

$$\sigma_{xx} = E\epsilon_{xx} = -Ez\frac{\partial \theta_y}{\partial x} \tag{19}$$

$$\tau_{xz} = G\gamma_{xz} = G\left(\frac{\partial w_0}{\partial x} - \theta_y\right) \tag{20}$$

where G is the shear modulus. To compensate for the discrepancy between the constant shear stress profile predicted by this equation and the actual parabolic profile, the shear correction factor κ (or k_s) is introduced. The resultant shear force Q_z is then given by:

$$Q_z = \kappa GA\gamma_{xz} = \kappa GA\left(\frac{\partial w_0}{\partial x} - \theta_y\right) \tag{21}$$

The theory results in a system of two coupled partial differential equations for the two unknowns, w_0 and ϕ_y:

$$\frac{\partial}{\partial x}\left[\kappa GA\left(\frac{\partial w_0}{\partial x} - \theta_y\right)\right] + q(x,t) = \rho A\frac{\partial^2 w_0}{\partial t^2} \tag{22}$$

$$\frac{\partial}{\partial x}\left[EI_{yy}\frac{\partial \theta_y}{\partial x}\right] + \kappa GA\left(\frac{\partial w_0}{\partial x} - \theta_y\right) = \rho I_{yy}\frac{\partial^2 \theta_y}{\partial t^2} \tag{23}$$

This coupled system governs the flexural and shear behavior of the beam, including rotary inertia effects (the term on the right-hand side of Eq. 23).

3 Higher-Order Shear Deformation Theories (HSDT)

The limitations of Timoshenko beam theory (TBT), particularly the need for a shear correction factor, motivated the development of Higher-Order Shear Deformation Theories (HSDTs). In this section, the Cartesian coordinates are denoted by (x, y, z), where x and y define the mid-plane of the structure and z represents the thickness coordinate, with $-h/2 \leq z \leq h/2$, where h is the total thickness. The displacement components along the x, y, and z directions are denoted by $u(x, y, z)$, $v(x, y, z)$, and $w(x, y, z)$, respectively.

These theories, pioneered by researchers such as Reddy [101], use higher-order terms, such as cubic, quintic, or trigonometric functions, in the expansion of the in-plane displacement field through the thickness coordinate. This allows for a more realistic non-linear distribution of transverse shear strain and stress. Consequently, HSDTs can satisfy the zero-traction boundary conditions at the top and bottom surfaces naturally, thereby eliminating the need for a shear correction factor. HSDTs provide significantly more accurate results for thick beams and laminated composite structures where shear deformation is prominent.

Several higher-order theories have been proposed by NAGHDI [102] and Reddy [101], Phan and Reddy [103], Reddy [104]. In general, these theories use a Taylor series expansion of the displacement field through the thickness. For a generic in-plane displacement component u_α, where $\alpha = x, y$, the expansion can be written as

$$u_\alpha(x, y, z) = u_\alpha^0(x, y) + \sum_{k=1}^{n} z^k \, \phi_\alpha^{(k)}(x, y), \qquad \alpha = x, y, \tag{24}$$

where $u_\alpha^0(x, y)$ represents the displacement of a point located on the mid-plane in the α direction, $\phi_\alpha^{(k)}(x, y)$ denotes the k-th order generalized displacement or rotation function associated with the thickness expansion, and n is the order of the adopted displacement model. The superscript (k) is an index indicating the order of the term and should not be interpreted as a power. In Kirchhoff–Love theory, $n = 0$ for the transverse displacement assumptions, while Reissner–Mindlin theory is a first-order shear deformation theory with $n = 1$ for the in-plane displacement components and $n = 0$ for the transverse displacement component.

According to Reddy [105] and Mallikarjuna and Kant [106], the assumptions underlying the development of these higher-order theories are:

- Displacements are small compared to the plate thickness.
- Cross-sections, initially planar and normal to the mid-plane, do not necessarily remain planar and normal to it after deformation.
- The transverse normal strain, denoted by ε_{zz}, may be considered non-negligible in refined models.
- The transverse normal stress, denoted by σ_{zz}, may also be considered non-negligible in advanced higher-order or quasi-3D models.

Most higher-order shear deformation theories are based on the approaches of Reissner [107] and Hencky–Mindlin [108]. For plate-type structures, the displacement field is commonly written as

$$u(x, y, z) = u_0(x, y) - z \, \frac{\partial w_0(x, y)}{\partial x} + f(z) \, \varphi_x(x, y), \tag{25}$$

$$v(x, y, z) = v_0(x, y) - z \, \frac{\partial w_0(x, y)}{\partial y} + f(z) \, \varphi_y(x, y), \tag{26}$$

$$w(x, y, z) = w_0(x, y), \tag{27}$$

where $u_0(x, y)$, $v_0(x, y)$, and $w_0(x, y)$ are the mid-plane displacement components along the x, y, and z directions, respectively. The terms $\partial w_0/\partial x$ and $\partial w_0/\partial y$ represent the bending slopes of the transverse displacement. The functions $\varphi_x(x, y)$ and $\varphi_y(x, y)$ are generalized shear rotation functions associated with transverse shear deformation in the xz and yz planes, respectively. The function $f(z)$ is the transverse shear warping function, which describes the non-linear variation of the in-plane displacement through the thickness.

For beam-type structures, where the deformation is usually described in the (x, z) plane, the above displacement field reduces to

$$u(x, z) = u_0(x) - z\,\frac{dw_0(x)}{dx} + f(z)\,\varphi_x(x), \tag{28}$$

$$w(x, z) = w_0(x), \tag{29}$$

where $u_0(x)$ is the axial displacement of the beam midline, $w_0(x)$ is the transverse displacement, dw_0/dx is the bending slope, and $\varphi_x(x)$ is the generalized shear deformation variable.

Higher-Order Shear Deformation Theories improve upon first-order models by incorporating a more realistic non-linear distribution of the axial displacement through the beam or plate thickness. This is achieved by introducing the transverse shear warping function $f(z)$, which models the distortion of the cross-section due to shear deformation. The derivative of this function, $f'(z)$, directly affects the transverse shear strain distribution. For example, in the xz plane, the transverse shear strain is generally written as

$$\gamma_{xz} = \frac{\partial u}{\partial z} + \frac{\partial w}{\partial x}, \tag{30}$$

where γ_{xz} denotes the engineering transverse shear strain. By selecting a suitable form of $f(z)$, the shear strain and shear stress distributions can be made parabolic or otherwise non-linear through the thickness.

A key advantage of these advanced theories is their ability to accurately represent the distribution of transverse shear stresses, such as τ_{xz} and τ_{yz}, across the thickness. In particular, the zero-traction boundary conditions at the upper and lower surfaces of the structure can be satisfied as

$$\tau_{xz} = \tau_{yz} = 0 \qquad \text{at} \qquad z = \pm\frac{h}{2}. \tag{31}$$

Therefore, unlike Timoshenko beam theory, HSDTs do not require an artificial shear correction factor. Consequently, HSDT models are robust and accurate for both moderately thick and thick beams, plates, and laminated composite structures.

Several influential contributions to higher-order beam and plate theories are summarized in the following table, where the different proposed forms of the warping function $f(z)$ are listed.

Table 1: Examples of warping functions $f(z)$ used in various HSDT beam theories. For comparison, the implied functions for CBT and FSDT are also included.

Theory	**Function** $f(z)$
CBT [95]	$f(z) = 0$
FSDT (TBT) [96]	$f(z) = z$
TSDT [109]	$f(z) = z\left(1 - \frac{4z^2}{3h^2}\right)$
TrSDT [98]	$f(z) = -\frac{h}{\pi}\sin\left(\frac{\pi z}{h}\right)$
ESDT [99]	$f(z) = ze^{-2(z/h)^2}$
HSDT [110]	$f(z) = h\sinh\left(\frac{z}{h}\right) - z\cosh\left(\frac{1}{2}\right)$

4 Refined Beam Theory (RBT)

A particularly efficient class of higher-order models is the Refined Beam Theory (RBT), which can be categorized as a third-order shear deformation theory. The formulation of RBT is based on the key assumption that it accurately represents the parabolic variation of shear strains and stresses through the beam's thickness. This allows it to inherently satisfy the zero-traction boundary conditions on the top and bottom surfaces without requiring a shear correction factor.

A notable advantage of this model is its computational efficiency. It is formulated using only two primary variables to describe the transverse displacement, in contrast to some HSDTs which may require more. This reduction in variables simplifies the governing equations and the computational effort required for a solution. As a result, the theory provides high accuracy for the analysis of both thick and thin beams under mechanical loading.

The displacement field for the Refined Beam Theory is derived from the following core assumptions:

- The analysis is based on the theory of infinitesimal strains, where displacements are considered small relative to the beam's thickness.
- The transverse normal stress, σ_z, is considered negligible compared to the in-plane axial stress, σ_x.
- The total transverse displacement, w, is decomposed into a bending component, w_b, and a shear component, w_s. Both components are functions of the axial coordinate x and time t.
- The axial displacement, u, is also composed of contributions from bending and shear. The bending component is assumed to be analogous to the displacement predicted by Classical Beam Theory.

Based on these assumptions, the displacement field of the refined theory is given by:

$$\begin{cases} u(x,z,t) = u_0(x,t) - z\dfrac{dw_b}{dx} - f(z)\dfrac{dw_s}{dx} \\ \\ w(x,z,t) = w_b(x,t) + w_s(x,t) \end{cases} \tag{32}$$

where u_0 is the axial displacement of any point on the beam's mid-plane ($z = 0$). The functions $w_b(x,t)$ and $w_s(x,t)$ are the bending and shear components of the transverse displacement, respectively, and $f(z)$ is the transverse shear warping function that defines the shape of the shear strain distribution through the thickness.

Due to its numerous advantages, this refined theory framework, often extended to plates as Refined Plate Theory (RPT), has been successfully employed to solve complex structural problems. For instance, analytical solutions based on the Navier method have been used to evaluate the deflection and natural frequencies of simply supported laminated composite plates [111, 112] . Furthermore, by applying the Levy-type solution method with RPT for the analysis of orthotropic plates, researchers have determined the critical buckling loads for plates with two opposite edges simply supported and the other two subjected to arbitrary boundary conditions [113].

5 Quasi-3D Beam Theory (Q3D)

While HSDTs provide an excellent description of shear deformation, most of them still assume that the beam is inextensible in the transverse normal direction (i.e., the transverse normal strain ϵ_{zz} is zero). This assumption may be invalid for very thick

beams or for sandwich structures with soft cores, where thickness stretching effects can become significant.

The development of quasi-3D shear deformation theories, which enhance higher-order models by incorporating thickness stretching effects, has been a significant area of research. A prominent trend within this field has been the reduction of kinematic variables to create models that are both accurate and computationally efficient. Early contributions in this domain often featured five-unknown formulations; for example, several related quasi-3D frameworks were proposed by Thai et Kim [114] , Tounsi and Houari [115], Hamidi and Tounsi [116], Thai [117], Bessaim [118] , and Bennoun [119] , with each model being distinguished by its choice of shape functions. Subsequent research focused on further simplifying these theories. By introducing new hypotheses to six-variable models, Zenkour [120] successfully developed a novel four-variable quasi-3D theory and demonstrated its application to FGM plates, sandwich plates [121] , and laminated composite plates [122]. In a similar effort to create a more parsimonious model, Mantari and Guedes Soares [123, 124] also proposed a computationally efficient four-variable quasi-3D theory for functionally graded plates. Their approach elegantly combines the shear and thickness stretching effects by utilizing a hyperbolic shape function.

Quasi-3D (Q3D) theories were developed to address this by incorporating the effects of both transverse shear deformation and thickness stretching. They provide a more comprehensive, "quasi-three-dimensional" description of the beam's kinematics while still retaining the computational advantages of a one-dimensional framework. The Q3D displacement field used in this thesis not only includes higher-order terms for in-plane displacement but also allows the transverse displacement to vary through the thickness. A general form of such a displacement field can be expressed as:

$$\begin{cases} u(x,z,t) & = u_0(x,t) - z\frac{\partial w_b}{\partial x} + f(z)\frac{\partial w_s}{\partial x} \\ \\ w(x,z,t) & = w_b(x,t) + w_s(x,t) + g(z)w_z(x,t) \end{cases} \tag{33}$$

where u_0 is the axial displacement, w_b and w_s represent the bending and shear components of the transverse displacement, and w_z accounts for the thickness stretching via the function $g(z)$. The function $f(z)$ is chosen to ensure a parabolic shear strain distribution. This refined kinematic model is particularly well-suited for the analysis

of thick, multi-layered MEE-FGM microbeams.

$$g(z) = 1 - f'(z) \tag{34}$$

6 Modified couple stress theory

6.1 Review of the modified couple stress theory

Yang et al. [125] presented the modified couple stress theory (MCST) by revising the classical couple stress theory developed by Toupin [18], Mindlin and Tiersten [126], and Koiter [127]. By adding an extra equilibrium requirement for the moments of couples to make sure that the couple stress tensor is symmetrical, the number of extra material length scale parameters in the modified couple stress theory is cut down from two to one. The modified pair stress theory is better because it's hard to figure out the material properties. As shown in [125], the strain energy U depends on both strain and curvature.

$$U = \frac{1}{2}\int_V \left(\sigma_{ij}\varepsilon_{ij} + m_{ij}\chi_{ij}\right) dV \tag{35}$$

where m_{ij} stands for the parts of the deviatoric part of the symmetric couple stress tensor, and χ_{ij} stands for the parts of the symmetric curvature tensor as described by:

$$\begin{aligned}
&\chi_{xx} = \frac{\partial\theta_x}{\partial x}, && \chi_{yy} = \frac{\partial\theta_y}{\partial y}, && \chi_{zz} = \frac{\partial\theta_z}{\partial z},\\
&\chi_{xy} = \tfrac{1}{2}\left(\frac{\partial\theta_x}{\partial y} + \frac{\partial\theta_y}{\partial x}\right), && \chi_{xz} = \tfrac{1}{2}\left(\frac{\partial\theta_x}{\partial z} + \frac{\partial\theta_z}{\partial x}\right), && \chi_{yz} = \tfrac{1}{2}\left(\frac{\partial\theta_y}{\partial z} + \frac{\partial\theta_z}{\partial y}\right).
\end{aligned} \tag{36}$$

where the rotation vector θ is expressed in relation to the displacement field (u_x, u_y, u_z) as:

$$\begin{aligned}
\theta_x &= \frac{1}{2}\left(\frac{\partial u_z}{\partial y} - \frac{\partial u_y}{\partial z}\right)\\
\theta_y &= \frac{1}{2}\left(\frac{\partial u_x}{\partial z} - \frac{\partial u_z}{\partial x}\right)\\
\theta_z &= \frac{1}{2}\left(\frac{\partial u_y}{\partial x} - \frac{\partial u_x}{\partial y}\right)
\end{aligned} \tag{37}$$

The components m_{ij} are defined for the linear elastic material as:

$$m_{ij} = \frac{E}{1+\nu}\ell^2\chi_{ij} \tag{38}$$

where ℓ represents the material length scale parameter. The assessment and adjustment of ℓ are detailed in References [128, 129].

6.2 Modified couple stress models via EBT

The initial modified couple stress EBT model was created by Park and Gao [130] for isotropic microbeams. Their model was employed to examine the influence of the material length scale parameter on the deflection and bending rigidity of a cantilever epoxy beam under a concentrated load at the free end. The incorporation of the material length scale parameter results in an enhancement of the bending rigidity of the cantilever microbeam. The effect is significant at small beam thicknesses, but becomes negligible as beam thickness increases. This observation is consistent with the experimental data. Kong et al. [131, 132] extended the modified couple stress EBT model to address the free vibration [131] and buckling [132] issues of isotropic microbeams. The nonlinear modified couple stress EBT model was initially introduced by Xia et al. [133]for the analysis of nonlinear bending, post-buckling, and nonlinear free vibration of isotropic microbeams, utilising von Karman nonlinearity. The findings underscore the necessity of accounting for nonlinearity and size effects in the effective design of microscale devices and systems, including biosensors, atomic force microscopes, and MEMS [133].

Simsek [134] developed a nonlinear EBT model for analysing the nonlinear bending and vibration of isotropic microbeams, considering the interaction between the beam and an elastic medium. The nonlinear EBT model has been extensively utilised to investigate the size effect on nonlinear bending, nonlinear vibration, and post-buckling responses of isotropic microbeams. Farokhi et al. [135] examined initial geometric imperfections in the nonlinear forced vibration of beams, while Togun and Bagdatli [136] incorporated axial pretension in the nonlinear free vibration of microbeams. Wang et al. [137, 138] considered the thermal effect in the nonlinear bending [137], post-buckling, and free vibration [138] of beams. Ansari et al. [139] presented closed-form solutions for the vibration and postbuckling analyses of microbeams subjected to various boundary conditions.

The EBT model was applied to the FG microbeams as well. Asghari et al. [140]

utilised it to predict the bending and free vibration behaviours of FG microbeams. The free vibration of functionally graded tapered microbeams, characterised by material properties that change along the longitudinal direction, was investigated by Akgoz and Civalek [141] and Shafiei et al. [142]. Akgoz and Civalek [141] focused exclusively on cantilever beams, whereas Shafiei et al. [142] incorporated geometric nonlinearity in beams with various boundary conditions. Simsek [143] investigated the nonlinear free vibration characteristics of axially functionally graded microbeams. He employed the Galerkin and He's variational method to derive approximate solutions for beams with simply supported and clamped boundary conditions. Dehrouyeh-Semnani et al. [144] incorporated initial geometric imperfections in the free vibration analysis of FG microbeams.

6.3 Modified couple stress models via TBT

Ma et al. [145] first came up with the modified couple stress TBT model by adding the effects of shear deformation to the EBT model that Park and Gao [130] had already come up with. The model was employed to investigate the effects of the material length scale parameter and shear deformation on the deflections and natural frequencies of simply supported isotropic microbeams. Asghari et al. [146] obtained closed-form solutions for the bending response of beams subjected to diverse boundary conditions (BCs) within the TBT model. Conversely, Dos Santos and Reddy [147] derived approximate solutions for the buckling loads and natural frequencies of beams with varying boundary conditions using the Ritz method. Dehrouyeh-Semnani and Nikkhah-Bahrami [148] utilised both EBT and TBT models to examine the Poisson effect in isotropic microbeams. A comparative analysis of the bending rigidities and deflections of epoxy cantilever microbeams under concentrated loads, as predicted by modified couple stress models and confirmed through experimental tests, demonstrates that the inclusion of the Poisson effect in these models leads to an underestimation of the epoxy cantilever microbeam's deflection, as shown in Fig. 5. Liu and Reddy [149] developed a modified couple stress TBT model for isotropic curved microbeams, utilising it to examine bending and free vibration phenomena in simply supported curved beams. Taati et al. [150] created a TBT model to study thermal effects in isotropic microbeams. Asghari et al. [151] developed a nonlinear TBT model for the analysis of bending and free vibrations in isotropic microbeams. Ghayesh et al. [152, 153] proposed a nonlinear TBT model to tackle nonlinear resonant phenomena

in isotropic microbeams.

The TBT model was utilised for microbeams fabricated from functionally graded and laminated composite materials. Reddy [154] created EBT and TBT models for FG microbeams that took into account geometric nonlinearity. Closed-form equations were given for the natural frequencies, deflections, and buckling loads of microbeams that were simply supported. Ke et al. [155] developed a nonlinear TBT model to examine the effect of size on the nonlinear vibrational properties of FG microbeams. Asghari et al. [156] developed a TBT model to analyse the effects of size on the deflections and rotations of cantilever FG beams, as well as the natural frequencies of simply supported FG beams. However, their model did not take into account geometric nonlinearity. Ke and Wang [157] utilised the TBT model to examine the free vibration, static buckling, and dynamic stability characteristics of FG microbeams under diverse boundary conditions employing the DQ method. Nateghi and Salamat-talab [158] examined the buckling and free vibration responses of FG microbeams at elevated temperatures employing the modified couple stress TBT model. The DQ method was used to find the natural frequencies and critical buckling loads of FG microbeams under different boundary conditions. Numerical results indicated that the impact of temperature becomes significant at higher ratios of beam thickness to the material length scale parameter. Simsek et al. [159] employed the TBT model to investigate the impact of size on the deflections of simply supported FG microbeams subjected to uniform and concentrated loads. Chen et al. [160] , Chen and Li [161] , Roque et al. [162] , and Mohammad-Abadi and Daneshmehr [163] expanded the use of the TBT model to encompass the static bending [160, 162] , free vibration, and buckling [163] of laminated composite microbeams. Thai et al. [164] additionally employed the TBT model to tackle static bending, buckling, and free vibration challenges in FG sandwich microbeams. Krysko et al. [165] have recently created a TBT model for analysing the static bending and free vibration of three-layer microbeams using Grigolyuk-Chulkov theory.

6.4 Modified couple stress models via RBT

Ma et al. [166] were the first to suggest the modified couple stress RBT model for isotropic microbeams. The research examined the influence of size on the static bending and free vibration responses of simply supported microbeams. Mohammad-Abadi and Daneshmehr [167] expanded the utilisation of the RBT model to investigate the

size effect on the buckling behaviour of isotropic microbeams. Their studies included both EBT and TBT models. We provided analytical solutions for simply supported beams so that we could compare them. Salamat-talab et al. [168] broadened the utilisation of the RBT model to FG microbeams, obtaining closed-form solutions for the deflections and natural frequencies of simply supported microbeams. Nateghi et al. [169] and Aghazadeh et al. [170] put forward a detailed model that looks at buckling [169] , bending, and free vibration [170] of functionally graded microbeams. The unified model incorporates three separate beam theories: EBT, FBT, and TBT. We use the DQ solution method to find the buckling loads, deflections, and natural frequencies of FG microbeams when they are put under different boundary conditions. Chen et al. [171] developed an RBT model for laminated composite microbeams by employing an innovative constitutive relation for anisotropic materials. The model was utilised to examine the effect of size on the deflections of cross-ply simply supported microbeams under uniform loading conditions. MohammadAbadi and Daneshmehr [172] and Mohammad-Abadi et al. [173] built on their isotropic model from [167] to study the free vibration [172] and thermal buckling [173] of laminated composite microbeams under various boundary conditions.

6.5 Modified couple stress models via HSDTs

Darijani and Mohammadabadi [174] presented a revised couple stress higher-order shear deformation theory (HSDT) model for isotropic microbeams, differentiating the axial and transverse displacements into shear and bending components. The shape function for the shear part, shown in Table 2, was created with the assumption that the transverse shear stress and couple stress are both zero at the top and bottom surfaces of the cross-section. Noori et al. [175] recently presented an HSDT model for the free vibration of isotropic microbeams, employing a fifth-order variation of the axial displacement across the thickness. The DQ solution method was employed to ascertain the natural frequencies of microbeams under varying boundary conditions. Simsek and Reddy [176] developed an extensive HSDT model for FG microbeams, integrating seven distinct beam theories: EBT, TBT, RBT, the sinusoidal theory of Touratier [98] , the hyperbolic theory of Soldatos [177], the exponential theory of Karama et al. [178] , and the general exponential theory of Aydogdu [179] . The model was used to solve the problems of bending and free vibration in FG microbeams that are simply supported. Simsek and Reddy [180] and Akbarzadeh Khorshidi et al. [181]

expanded the model to tackle buckling problems of functionally graded (FG) embedded microbeams [180] and postbuckling issues of FG microbeams under general boundary conditions [181] . Trinh et al. [182] proposed a cohesive modified couple stress model for functionally graded microbeams, amalgamating higher-order shear deformation theory (HSDT) and quasi-3D beam theories. The displacement field in their model is based on the framework set up by Thai et al. [117] , which divides the transverse displacements into bending, shear, and thickness stretching components, as shown in Table 3. Using the sinusoidal theory put forth by Touratier [98] , Akgoz and Civalek [183] developed a modified couple stress sinusoidal model to investigate the thermal-mechanical buckling properties of simply supported functionally graded materials (FG).

Table 2: HSDT shape functions and corresponding displacement fields.

Reference	**Shape function** $f(z)$	**Displacement field**
Aydogdu [179]	$f(z) = z\alpha^{-2(z/h)^2/\ln\alpha}, \quad \alpha > 0$	$u_x(x,z,t) = u(x,t) - z\dfrac{\partial w}{\partial x} + f(z)\phi_x(x,t),$ $u_z(x,z,t) = w(x,t)$
Karama et al. [99]	$f(z) = ze^{-2(z/h)^2}$	
Touratier [98]	$f(z) = \frac{h}{\pi}\sin\left(\frac{\pi z}{h}\right)$	
Soldatos [177]	$f(z) = h\sinh\left(\frac{z}{h}\right) - z\cosh\left(\frac{1}{2}\right)$	
Shimpi [184]	$f(z) = \left[\frac{5}{3}\left(\frac{z}{h}\right)^2 - \frac{1}{4}\right] z$	$u_x(x,z,t) = u(x,t) - z\dfrac{\partial w_b}{\partial x} - f(z)\dfrac{\partial w_s}{\partial x},$ $u_z(x,z,t) = w_b(x,t) + w_s(x,t)$
Thai and Choi [185]	$f(z) = \frac{4z^3}{3h^2}$	
Thai and Vo [185, 186]	$f(z) = z - \frac{h}{\pi}\sin\left(\frac{\pi z}{h}\right)$	
Darijani and Mohammadabadi [174]	$f(z) = \frac{z^5}{20h^4} - \frac{z^3}{24h^2} + \frac{63z}{64} + \alpha$	
Darijani and Shahdadi [187]	$f(z) = z\left[-\frac{121}{16} + \frac{455}{4}\left(\frac{z}{h}\right)^2 - 483\left(\frac{z}{h}\right)^4 + 660\left(\frac{z}{h}\right)^6\right]$	
Xiang et al. [188]	$f(z) = \frac{1}{n}\left(\frac{2}{h}\right)^{n-1} z^n,$ with $n = 3, 5, 7, 9, \ldots$	$u_x(x,z,t) = u(x,t) - z\phi_x(x,t) + f(z)\left(\phi_x(x,t) + \dfrac{\partial w}{\partial x}\right),$ $u_z(x,z,t) = w(x,t)$

Table 3: Q3D shape functions and corresponding displacement fields.

Reference	**Shape function(s)**	**Displacement field**
Thai and Kim [114]	$f(z) = z - \frac{h}{\pi}\sin\left(\frac{\pi z}{h}\right)$	$u_x(x,z,t) = u(x,t) - z\dfrac{\partial w_b}{\partial x} - f(z)\dfrac{\partial w_s}{\partial x},$ $u_z(x,z,t) = w_b(x,t) + w_s(x,t) + g(z)w_z(x,t)$
Sobhy and Radwan [189]	$f(z) = z - \dfrac{z\cosh\left(\frac{\pi}{2}\right) - \frac{h}{\pi}\sin\left(\frac{\pi z}{h}\right)}{\cosh\left(\frac{\pi}{2}\right) - 1}$	
Thai et al. [117]	$f(z) = z - h\sinh\left(\frac{z}{h}\right) + z\cosh\left(\frac{z}{h}\right)$	
Lei et al. [190]; Trinh et al. [191]	$f(z) = \frac{4z^3}{3h^2}, \quad g(z) = 1 - f'(z)$	
Reddy and Kim [192]	–	$u_x(x,z,t) = u(x,t) + z\theta_x + z^2\phi_x + z^3\psi_x,$ $u_z(x,z,t) = w(x,t) + z\theta_z + z^2\phi_z$
Nguyen et al. [193]	$f(z) = \pi z\left(-1 + \frac{9z^2}{5h^2} - \frac{28z^4}{25h^4}\right),\ g(z) = \frac{1}{8}f'(z),$ $f(z) = z\left(8 - \frac{10z^2}{3h^2} - \frac{6z^4}{5h^4} + \frac{8z^6}{7h^6}\right),\ g(z) = \frac{3}{20}f'(z)$	$u_x(x,z,t) = u(x,t) - z\dfrac{\partial w_b}{\partial x} - f(z)\dfrac{\partial w_s}{\partial x},$ $u_z(x,z,t) = w_b(x,t) + w_s(x,t) + g(z)w_z(x,t)$

7 Conclusion

This chapter has established the theoretical foundation for the present study by systematically reviewing the hierarchy of beam theories. The review traced the evolution of kinematic assumptions, beginning with the constraints of Classical Beam Theory (CBT) and the introduction of shear effects in First-Order Shear Deformation Theory (FSDT). It continued through the advanced formulations of Higher-Order (HSDT) and Refined Beam Theories (RBT), culminating in the quasi-3D theories that offer a more complete description of the beam's kinematics. The primary objective of this literature survey was to identify a theoretical framework that balances analytical accuracy with computational feasibility for modeling complex microstructures. Based on this analysis, the quasi-3D shear deformation theory has been selected as the optimal model for this research. Its unique capability to account for both transverse shear and thickness stretching effects makes it particularly well-suited for capturing the intricate electromechanical coupling present in magnetoelectric microbeams. Accordingly, the central contribution of this thesis will be the implementation and application of this quasi-3D theory to investigate the bending and free vibration response of such microstructures. The validity and robustness of the proposed model will be established through a comparative analysis, where our findings will be benchmarked against results derived from the other prominent theories discussed in this chapter, thereby situating our contribution within the broader landscape of structural mechanics.

Part II

PART TWO: SCIENTIFIC CONTRIBUTIONS

Chapter V: Variational Formulation for Magneto-Electro Functionally Graded Microbeams Based on a Quasi-3D Beam Theory

Chapter VI: Numerical Implementation Using the Differential Quadrature Finite Element Method (DQ-FEM)

Chapter VII: Results and Discussion

Chapter V: Variational Formulation for Magneto-Electro Functionally Graded Microbeams based on a Quasi-3D Beam Theory

1 Introduction

The development of magneto-electro-elastic (MEE) functionally graded microbeams has attracted considerable attention due to their potential applications in advanced microelectromechanical systems (MEMS), sensors, actuators, and energy harvesters. The integration of mechanical, electrical, magnetic, and thermal fields within a single structural element offers unique advantages in multifunctionality and adaptability. However, accurately modeling the behavior of such microstructures requires advanced formulations that can capture both material gradation effects and small-scale phenomena.

In this chapter, we present the variational formulation for MEE functionally graded microbeams based on a quasi-3D beam theory, which accounts for both transverse shear deformation and thickness stretching effects without relying on shear correction factors. Three distinct microbeam configurations are considered:

1. Magneto-Electro Functionally Graded Sandwich Microbeams.
2. Magneto-Electro Bilaterally Coated Functionally Graded Microbeams.
3. Magneto-Electro Bi-Coated Functionally Graded Microbeams.

For each model, detailed derivations of the kinetic energy, strain energy, and virtual work expressions are provided, establishing the foundation for subsequent governing equations through Hamilton's principle. This systematic approach enables a unified framework to analyze the dynamic and static behavior of advanced MEE microbeam structures under various loading and boundary conditions.

2 General formulation

The total strain energy in this particular situation is as follow:

$$U = \frac{1}{2}\int_0^L \int_A \left(\sigma_{ij}\varepsilon_{ij} + m_{ij}\chi_{ij} - D_i E_i - B_i H_i\right) dA dx \tag{39}$$

The equations representing "transversely isotropic magneto-electro-elastic materials" are provided in accordance with the extended MCST [10, 13, 194]. Where $\sigma_{ij}, m_{ij}, D_i, B_i$ represent the "Cauchy stress tensor, deviatoric couple stress tensor, electric displacements, and magnetic fluxes":

$$\begin{Bmatrix} \sigma_{xx} \\ \sigma_{yy} \\ \sigma_{zz} \\ \sigma_{yz} \\ \sigma_{zx} \\ \sigma_{xy} \end{Bmatrix} = \begin{bmatrix} C_{11} & C_{12} & C_{13} & 0 & 0 & 0 \\ C_{12} & C_{22} & C_{23} & 0 & 0 & 0 \\ C_{13} & C_{23} & C_{33} & 0 & 0 & 0 \\ 0 & 0 & 0 & C_{44} & 0 & 0 \\ 0 & 0 & 0 & 0 & C_{55} & 0 \\ 0 & 0 & 0 & 0 & 0 & C_{66} \end{bmatrix} \begin{Bmatrix} \varepsilon_{xx} \\ \varepsilon_{yy} \\ \varepsilon_{zz} \\ 2\varepsilon_{yz} \\ 2\varepsilon_{zx} \\ 2\varepsilon_{xy} \end{Bmatrix} - \begin{bmatrix} 0 & 0 & q_{31} \\ 0 & 0 & q_{32} \\ 0 & 0 & q_{33} \\ 0 & q_{24} & 0 \\ q_{15} & 0 & 0 \\ 0 & 0 & 0 \end{bmatrix} \begin{Bmatrix} H_x \\ H_y \\ H_z \end{Bmatrix} - \begin{bmatrix} 0 & 0 & e_{31} \\ 0 & 0 & e_{32} \\ 0 & 0 & e_{33} \\ 0 & e_{24} & 0 \\ e_{15} & 0 & 0 \\ 0 & 0 & 0 \end{bmatrix} \begin{Bmatrix} E_x \\ E_y \\ E_z \end{Bmatrix} \tag{40}$$

$$\begin{Bmatrix} m_{xx} \\ m_{yy} \\ m_{zz} \\ m_{yz} \\ m_{zx} \\ m_{xy} \end{Bmatrix} = \begin{bmatrix} A_{11} & A_{12} & A_{13} & 0 & 0 & 0 \\ A_{12} & A_{22} & A_{23} & 0 & 0 & 0 \\ A_{13} & A_{23} & A_{33} & 0 & 0 & 0 \\ 0 & 0 & 0 & A_{44} & 0 & 0 \\ 0 & 0 & 0 & 0 & A_{55} & 0 \\ 0 & 0 & 0 & 0 & 0 & A_{66} \end{bmatrix} \begin{Bmatrix} \chi_{xx} \\ \chi_{yy} \\ \chi_{zz} \\ 2\chi_{yz} \\ 2\chi_{zx} \\ 2\chi_{xy} \end{Bmatrix} \tag{41}$$

$$\begin{Bmatrix} D_x \\ D_y \\ D_z \end{Bmatrix} = \begin{bmatrix} 0 & 0 & 0 & 0 & e_{15} & 0 \\ 0 & 0 & 0 & e_{24} & 0 & 0 \\ e_{31} & e_{32} & e_{33} & 0 & 0 & 0 \end{bmatrix} \begin{Bmatrix} \varepsilon_{xx} \\ \varepsilon_{yy} \\ \varepsilon_{zz} \\ 2\varepsilon_{yz} \\ 2\varepsilon_{zx} \\ 2\varepsilon_{xy} \end{Bmatrix} + \begin{bmatrix} s_{11} & 0 & 0 \\ 0 & s_{22} & 0 \\ 0 & 0 & s_{33} \end{bmatrix} \begin{Bmatrix} E_x \\ E_y \\ E_z \end{Bmatrix} + \begin{bmatrix} d_{11} & 0 & 0 \\ 0 & d_{22} & 0 \\ 0 & 0 & d_{33} \end{bmatrix} \begin{Bmatrix} H_x \\ H_y \\ H_z \end{Bmatrix} \tag{42}$$

$$\begin{Bmatrix} B_x \\ B_y \\ B_z \end{Bmatrix} = \begin{bmatrix} 0 & 0 & 0 & 0 & q_{15} & 0 \\ 0 & 0 & 0 & q_{24} & 0 & 0 \\ q_{31} & q_{32} & q_{33} & 0 & 0 & 0 \end{bmatrix} \begin{Bmatrix} \varepsilon_{xx} \\ \varepsilon_{yy} \\ \varepsilon_{zz} \\ 2\varepsilon_{yz} \\ 2\varepsilon_{zx} \\ 2\varepsilon_{xy} \end{Bmatrix} + \begin{bmatrix} \mu_{11} & 0 & 0 \\ 0 & \mu_{22} & 0 \\ 0 & 0 & \mu_{33} \end{bmatrix} \begin{Bmatrix} H_x \\ H_y \\ H_z \end{Bmatrix} + \begin{bmatrix} d_{11} & 0 & 0 \\ 0 & d_{22} & 0 \\ 0 & 0 & d_{33} \end{bmatrix} \begin{Bmatrix} E_x \\ E_y \\ E_z \end{Bmatrix} \tag{43}$$

The parameters $C_{\alpha\beta}\,(\alpha,\ \beta = 1, 2, \ldots,\ 6)$, $A_{\alpha\beta}\,(\alpha, \beta = 1, 2, \ldots,\ 6)$ describe the elastic stiffness tensor and the couple stress tensor, with:

$$A_{\alpha\beta} = C_{\alpha\beta} l^2 \tag{44}$$

Where l is the material length scale parameter (MLSP). $q_{i\alpha}$, $e_{i\alpha}$, s_{ij}, μ_{ij}, d_{ij} are the piezomagnetic tensor, the piezoelectric tensor, the dielectric tensor, the magnetic permeability tensor, and the magneto-dielectric tensor respectively. And ε_{ij}, χ_{xx} are "the strain tensor and the rotationally symmetric gradient tensor", which are described by the following equations:

$$\varepsilon_{ij} = \frac{1}{2}\left(u_{i,j} + u_{j,i}\right) \tag{45}$$

$$\chi^{s}_{ij} = \frac{1}{2}\left(\theta_{i,j} + \theta_{j,i}\right) \tag{46}$$

$$\theta_i = \frac{1}{2} e_{ijk} u_{k,j} \tag{47}$$

The variables u_i and θ_i represent the components of the displacement vector and rotation vectors, respectively. e_{ijk} is the permutation symbol. Also, E_i and H_i represent the electric field and magnetic field intensities, respectively.

$$E_i = -\Phi_{,i} \quad , \qquad H_i = -M_{,i} \tag{48}$$

Φ and M represent the "electric and magnetic potentials", respectively

The distribution of electric and magnetic potentials in the thickness direction is provided by [11]:

$$\begin{cases} \Phi(x,z,t) = -\cos\left(\frac{\pi}{h}z\right)\gamma\left(x,t\right) + \frac{2z}{h}\gamma_0 \\ M(x,z,t) = -\cos\left(\frac{\pi}{h}z\right)\zeta\left(x,t\right) + \frac{2z}{h}\zeta_0 \end{cases} \tag{49}$$

The spatial variations of electric potential in the x-direction are represented by γ, while the external electric potential is denoted as γ_0. ζ and ζ_0 represent the spatial variations of the magnetic potential in the x-direction and the external magnetic potential, respectively

In accordance with the higher order quasi-3D beam theory, The current study posits that the field of displacement at any random spot on the microbeam can be expressed as follows:

$$\begin{cases} u\left(x,z,t\right)=u_0\left(x,t\right)-z\frac{dw_b}{dx}+f(z)\frac{dw_s}{dx} \\ w\left(x,z,t\right)=w_b\left(x,t\right)+w_s\left(x,t\right)+g\left(z\right)w_z\left(x,t\right) \end{cases} \tag{50}$$

The transversal displacement is divided into two components, notably w_b, w_s and w_z, following this method. Here, u, w_b, w_s and w_z represent the displacement in the x-direction, the bending component, the shear component, and the stretching component of the transverse displacement of the points on the neutral axis of the beam, respectively. The selection of our function $f(z)$ is governed by the shear function provided by Reddy [109].

$$f\left(z\right)=z-\left(1-\left(\frac{4z^2}{3h^2}\right)\right),\quad g\left(z\right)=\left(1-\frac{df}{dz}\right) \tag{51}$$

By substituting equation 50 into equation 45, the non-zero components of the deformation tensor are extracted as:

$$\begin{cases} \varepsilon_{xx}=\frac{du}{dx}-z\frac{d^2w_b}{dx^2}-f\frac{d^2w_s}{dx^2} \\ \varepsilon_{zz}=\frac{dg}{dz}w_z \\ \varepsilon_{xz}=\frac{1}{2}g\left(\frac{dw_s}{dx}+\frac{dw_z}{dx}\right) \end{cases} \tag{52}$$

Replacing equation 50 into 47 and then 46 gives:

$$\begin{cases} \theta_x=0 \\ \theta_y=\frac{1}{2}\left(\frac{du}{dz}-\frac{dw}{dx}\right)=-\frac{1}{2}\left(2\frac{dw_b}{dx}+\left(\frac{df_1}{dz}+1\right)\frac{dw_s}{dx}+f_2\frac{dw_z}{dx}\right) \\ \theta_y=0 \end{cases} \tag{53}$$

$$\begin{cases} \chi_{xx}=0 \\ \chi_{yy}=0 \\ \chi_{zz}=0 \\ \chi_{yz}=-\frac{1}{4}\left(\frac{d^2f_1}{dz^2}\frac{dw_s}{dx}+\frac{df_2}{dz}\frac{dw_z}{dx}\right) \\ \chi_{xz}=0 \\ \chi_{xy}=-\frac{1}{4}\left(2\frac{d^2w_b}{dx^2}+\left(\frac{df_1}{dz}+1\right)\frac{d^2w_s}{dx^2}+f_2\frac{d^2w_z}{dx^2}\right) \end{cases} \tag{54}$$

Introducing equation 49 into 48 yields:

$$
\begin{aligned}
H_x &= \cos\left(\tfrac{\pi}{h}z\right)\ \frac{d\zeta}{dx},\\
H_z &= -\tfrac{\pi}{h}\sin\left(\tfrac{\pi z}{h}\right)\zeta - \tfrac{2}{h}\zeta_0,\\
E_x &= \cos\left(\tfrac{\pi}{h}z\right)\ \frac{d\gamma}{dx},\\
E_z &= -\tfrac{\pi}{h}\sin\left(\tfrac{\pi z}{h}\right)\gamma - \tfrac{2}{h}\gamma_0.
\end{aligned}
\tag{55}
$$

Given Equations 45-48, the constitutive equation 39 is derived as follows:

$$
\begin{aligned}
U = \tfrac{1}{2}\int_0^l \Bigg(& I_1\left(\tfrac{du}{dx}\right)^2 - 2I_2\tfrac{du}{dx}\tfrac{d^2w_b}{dx^2} - 2I_3\tfrac{du}{dx}\tfrac{d^2w_s}{dx^2} + 2I_4\tfrac{d^2w_b}{dx^2}\tfrac{d^2w_s}{dx^2}\\
& + I_5\left(\tfrac{d^2w_b}{dx^2}\right)^2 + I_6\left(\tfrac{d^2w_s}{dx^2}\right)^2 + I_7w_z^2 + 2I_8\tfrac{du}{dx}w_z - 2I_9\tfrac{d^2w_b}{dx^2}w_z\\
& - 2I_{10}\tfrac{d^2w_s}{dx^2}w_z + I_{11}\left[\left(\tfrac{dw_s}{dx}\right)^2 + \left(\tfrac{dw_z}{dx}\right)^2 + 2\tfrac{dw_s}{dx}\tfrac{dw_z}{dx}\right]\\
& + 2I_{12}\tfrac{du}{dx}\gamma - 2I_{13}\tfrac{d^2w_b}{dx^2}\gamma - 2I_{14}\tfrac{d^2w_s}{dx^2}\gamma + 2I_{15}\tfrac{du}{dx}\zeta - 2I_{16}\tfrac{d^2w_b}{dx^2}\zeta\\
& - 2I_{17}\tfrac{d^2w_s}{dx^2}\zeta - 2I_{18}\left(\tfrac{dw_s}{dx}\tfrac{d\gamma}{dx} - \tfrac{dw_z}{dx}\tfrac{d\gamma}{dx}\right) - 2I_{19}\left(\tfrac{dw_s}{dx}\tfrac{d\zeta}{dx} - \tfrac{dw_z}{dx}\tfrac{d\zeta}{dx}\right)\\
& + 2I_{20}w_z\gamma + 2I_{21}w_z\zeta - I_{22}\left(\tfrac{d\gamma}{dx}\right)^2 - I_{23}\left(\tfrac{d\zeta}{dx}\right)^2 - 2I_{24}\tfrac{d\zeta}{dx}\tfrac{d\gamma}{dx}\\
& - I_{25}\gamma^2 - I_{26}\zeta^2 - 2I_{27}\gamma\zeta + D_1\left(\tfrac{dw_s}{dx}\right)^2 + D_2\left(\tfrac{dw_z}{dx}\right)^2 + 2D_3\tfrac{dw_s}{dx}\tfrac{dw_z}{dx}\\
& + 4D_4\left(\tfrac{d^2w_b}{dx^2}\right)^2 + 4D_5\tfrac{d^2w_b}{dx^2}\tfrac{d^2w_s}{dx^2} + 4D_6\tfrac{d^2w_b}{dx^2}\tfrac{d^2w_z}{dx^2} + 2D_7\tfrac{d^2w_s}{dx^2}\tfrac{d^2w_z}{dx^2}\\
& + D_8\left(\tfrac{d^2w_s}{dx^2}\right)^2 + D_9\left(\tfrac{d^2w_z}{dx^2}\right)^2\Bigg)\,dx
\end{aligned}
\tag{56}
$$

With:

$$\begin{cases} \{I_{1:6}\} = \int_{a_y}^{b_y}\int_{a_z}^{b_z} C_{11}\,(1, z, f, zf, z^2, f^2)\,dz\,dy, \\ \{I_{8:10}\} = \int_{a_y}^{b_y}\int_{a_z}^{b_z} C_{13}\,\frac{dg}{dz}\,(1, z, f)\,dz\,dy, \\ \{I_{12:14}\} = \int_{a_y}^{b_y}\int_{a_z}^{b_z} e_{31}\,\frac{\pi}{h}\sin\!\left(\frac{\pi z}{h}\right)(1, z, f)\,dz\,dy, \\ \{I_{18:19}\} = \int_{a_y}^{b_y}\int_{a_z}^{b_z} g\,\frac{\pi}{h}\cos\!\left(\frac{\pi z}{h}\right)(e_{15}, q_{15})\,dz\,dy, \\ \{I_{22:24}\} = \int_{a_y}^{b_y}\int_{a_z}^{b_z} \left(\frac{\pi}{h}\cos\!\left(\frac{\pi z}{h}\right)\right)^2(s_{11}, \mu_{11}, d_{11})\,dz\,dy, \\ \{I_7\} = \int_{a_y}^{b_y}\int_{a_z}^{b_z} C_{33}\left(\frac{dg}{dz}\right)^2 dz\,dy, \\ \{I_{11}\} = \int_{a_y}^{b_y}\int_{a_z}^{b_z} C_{55}\,g^2\,dz\,dy, \\ \{I_{15:17}\} = \int_{a_y}^{b_y}\int_{a_z}^{b_z} q_{31}\,\frac{\pi}{h}\sin\!\left(\frac{\pi z}{h}\right)(1, z, f)\,dz\,dy, \\ \{I_{20:21}\} = \int_{a_y}^{b_y}\int_{a_z}^{b_z} \frac{dg}{dz}\,\frac{\pi}{h}\sin\!\left(\frac{\pi z}{h}\right)(e_{33}, q_{33})\,dz\,dy, \\ \{I_{25:27}\} = \int_{a_y}^{b_y}\int_{a_z}^{b_z} \left(\frac{\pi}{h}\sin\!\left(\frac{\pi z}{h}\right)\right)^2(s_{33}, \mu_{33}, d_{33})\,dz\,dy. \end{cases} \tag{57}$$

$$\begin{cases} \{D_{1:3}\} = \int_{a_y}^{b_y}\int_{a_z}^{b_z} \frac{1}{4}A_{44}\left(\frac{d^2f}{dz^2},\ \left(\frac{dg}{dz}\right)^2,\ \frac{d^2f}{dz^2}\frac{dg}{dz}\right)dz\,dy, \\ \{D_{4:9}\} = \int_{a_y}^{b_y}\int_{a_z}^{b_z} \frac{1}{4}A_{66}\left(1,\ \frac{df}{dz}+1,\ g,\ g\left(\frac{df}{dz}+1\right),\ \left(\frac{df}{dz}+1\right)^2,\ g^2\right)dz\,dy. \end{cases} \tag{58}$$

with the integral boundary $\int_{a_y}^{b_y}$, $\int_{a_z}^{b_z}$ vary according to microbeams models.

The total kinetic energy can be written according to the Q3D theory:

$$\begin{aligned} T = \frac{1}{2}\int_0^l \Big[& J_1\left(\dot{u}^2 + \dot{w}_b^2 + \dot{w}_s^2 + 2\dot{w}_b\dot{w}_s\right) - 2J_2\dot{u}\frac{d\dot{w}_b}{dx} - 2J_3\dot{u}\frac{d\dot{w}_s}{dx} \\ & + 2J_4\frac{d\dot{w}_b}{dx}\frac{d\dot{w}_s}{dx} + J_5\left(\frac{d\dot{w}_b}{dx}\right)^2 + J_6\left(\frac{d\dot{w}_s}{dx}\right)^2 \\ & + J_7\dot{w}_z^2 + 2J_8\left(\dot{w}_b\dot{w}_z + \dot{w}_s\dot{w}_z\right)\Big]\,dx. \end{aligned} \tag{59}$$

With:

$$\begin{bmatrix} J_1 \\ J_2 \\ J_3 \\ J_4 \\ J_5 \\ J_6 \\ J_7 \\ J_8 \end{bmatrix} = \int_{a_y}^{b_y} \int_{a_z}^{b_z} \rho \begin{bmatrix} 1 \\ z \\ f \\ zf \\ z^2 \\ f^2 \\ g^2 \\ g \end{bmatrix} dz\, dy \tag{60}$$

Furthermore, the virtual work performed by the applied loades acting on the current quasi-3D microbeam can be written as:

$$W_{\text{ext}} = \int_0^L q_0 \Big(w_b(x,t) + w_s(x,t) + g(z)\, w_z(x,t) \Big)\, dx \tag{61}$$

3 Magneto-Electro Functionally Graded Sandwich (MEFGS) Microbeams.

This section considers a microbeam of length L, width b, and thickness h, as shown in figure 14, from which the microbeam is composed of a MEE core with a thickness h_c and two FG surface layers with thickness h_u for the upper and h_b for the bottom. The total thickness h is given by the sum of h_u+h_c+h_b. for a given thickness ratio, the values of h_u, h_c, and h_b are determined as fractions of h. These fractions can be generated based on the specific ratio $(r_u - r_c - r_b)$ (e.g., 1-1-1 or 2-1-1). Each layer's thickness can be expressed as a fraction of h, $h_u = h\frac{r_u}{r_u+r_c+r_b}$, $h_c = h\frac{r_c}{r_u+r_c+r_b}$, $h_b = h\frac{r_b}{r_u+r_c+r_b}$.

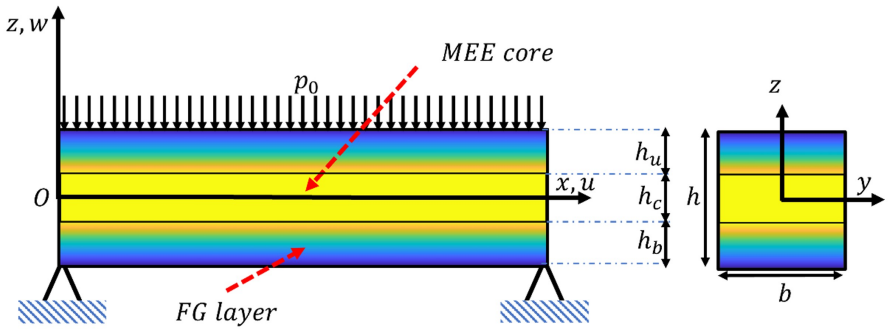


Figure 14: Sandwich FG microbeam model with MEE core

The material characteristics are considered to change continuously in two opposite

direction throughout the thickness (z-axis) in the upper and bottom layers based on the power-law distribution [195]. The following equations describe the distribution of material characteristics in FG materials:

$$P\left(z\right) = \left(P_1 - P_2\right) V_m\left(z\right) + P_2 \tag{62}$$

$$V_m(z) = 1 - V_c(z), \qquad V_c(z) = \begin{cases} \left(\frac{h+2z}{h-h_c}\right)^k & \text{for } z \in z_b^{\pm} = \left[-\frac{h_c}{2} - h_b, -\frac{h_c}{2}\right] \\ 1 & \text{for } z \in z_c^{\pm} = \left[-\frac{h_c}{2}, \frac{h_c}{2}\right] \\ \left(\frac{h-2z}{h-h_c}\right)^k & \text{for } z \in z_u^{\pm} = \left[\frac{h_c}{2}, \frac{h_c}{2} + h_u\right] \end{cases} \tag{63}$$

Where $P\left(z\right)$ represent "elastic stiffness, couple stress stiffness, piezoelectric constant, piezomagnetic constant, dielectric constant, magnetic permeability constant, magneto-dielectric constant and density".

The boundaries borne of the stiffness coefficients in equations 57, 58 according to the Magneto-Electro Functionally Graded Sandwich Microbeam model are as follow, where the subscripts b, c, u denote bottom, core, and upper layers :

$$
\begin{cases}
\{I_{1:6}\} = \displaystyle\int_{-b/2}^{b/2} \left[\sum_{m\in\{b,c,u\}} \int_{z_m^-}^{z_m^+} C_{11}^{(m)}(z)\, F_1(z)\, dz \right] dy, \\
I_7 = \displaystyle\int_{-b/2}^{b/2} \left[\sum_{m\in\{b,c,u\}} \int_{z_m^-}^{z_m^+} C_{33}^{(m)}(z) \Big(\tfrac{dg}{dz}\Big)^2 dz \right] dy, \\
\{I_{8:10}\} = \displaystyle\int_{-b/2}^{b/2} \left[\sum_{m\in\{b,c,u\}} \int_{z_m^-}^{z_m^+} C_{13}^{(m)}(z)\, \tfrac{dg}{dz}\, F_2(z)\, dz \right] dy, \\
I_{11} = \displaystyle\int_{-b/2}^{b/2} \left[\sum_{m\in\{b,c,u\}} \int_{z_m^-}^{z_m^+} C_{55}^{(m)}(z)\, g^2(z)\, dz \right] dy, \\
\{I_{12:14}\} = \displaystyle\int_{-b/2}^{b/2} \left[\sum_{m\in\{b,c,u\}} \int_{z_m^-}^{z_m^+} e_{31}^{(m)}(z)\, \tfrac{\pi}{h} \sin\Big(\tfrac{\pi z}{h}\Big)\, F_2(z)\, dz \right] dy, \\
\{I_{15:17}\} = \displaystyle\int_{-b/2}^{b/2} \left[\sum_{m\in\{b,c,u\}} \int_{z_m^-}^{z_m^+} q_{31}^{(m)}(z)\, \tfrac{\pi}{h} \sin\Big(\tfrac{\pi z}{h}\Big)\, F_2(z)\, dz \right] dy, \\
\{I_{18:19}\} = \displaystyle\int_{-b/2}^{b/2} \left[\sum_{m\in\{b,c,u\}} \int_{z_m^-}^{z_m^+} g(z)\, \tfrac{\pi}{h} \cos\Big(\tfrac{\pi z}{h}\Big)\, (e_{15}^{(m)}, q_{15}^{(m)})\, dz \right] dy, \\
\{I_{20:21}\} = \displaystyle\int_{-b/2}^{b/2} \left[\sum_{m\in\{b,c,u\}} \int_{z_m^-}^{z_m^+} \tfrac{dg}{dz}\, \tfrac{\pi}{h} \sin\Big(\tfrac{\pi z}{h}\Big) (e_{33}^{(m)}, q_{33}^{(m)})\, dz \right] dy, \\
\{I_{22:24}\} = \displaystyle\int_{-b/2}^{b/2} \left[\sum_{m\in\{b,c,u\}} \int_{z_m^-}^{z_m^+} \Big(\tfrac{\pi}{h} \cos\big(\tfrac{\pi z}{h}\big)\Big)^2 (s_{11}^{(m)}, \mu_{11}^{(m)}, d_{11}^{(m)})\, dz \right] dy, \\
\{I_{25:27}\} = \displaystyle\int_{-b/2}^{b/2} \left[\sum_{m\in\{b,c,u\}} \int_{z_m^-}^{z_m^+} \Big(\tfrac{\pi}{h} \sin\big(\tfrac{\pi z}{h}\big)\Big)^2 (s_{33}^{(m)}, \mu_{33}^{(m)}, d_{33}^{(m)})\, dz \right] dy.
\end{cases}
\tag{64}
$$

with the compact notations:

$$
F_1(z) = (1,\ z,\ f,\ zf,\ z^2,\ f^2), \qquad F_2(z) = (1,\ z,\ f).
$$

$$
\begin{cases}
\{D_{1:3}\} = \displaystyle\int_{-b/2}^{b/2} \sum_{m\in\{b,c,u\}} \int_{z_m^-}^{z_m^+} \tfrac{1}{4} A_{44}\, F_3(z)\, dz\, dy, \\
\{D_{4:9}\} = \displaystyle\int_{-b/2}^{b/2} \sum_{m\in\{b,c,u\}} \int_{z_m^-}^{z_m^+} \tfrac{1}{4} A_{66}\, F_4(z)\, dz\, dy,
\end{cases}
\tag{65}
$$

where the compact notations are defined as

$$
F_3(z) = \left(\tfrac{d^2 f}{dz^2},\ \Big(\tfrac{dg}{dz}\Big)^2,\ \tfrac{d^2 f}{dz^2}\, \tfrac{dg}{dz} \right), \qquad F_4(z) = \left(1,\ \tfrac{df}{dz} + 1,\ g,\ g\Big(\tfrac{df}{dz} + 1\Big),\ \Big(\tfrac{df}{dz} + 1\Big)^2,\ g^2 \right).
$$

The inertia coefficients in equation 60 are as follow according to the MEFGS microbeam model :

$$\{J_1, J_2, J_3, J_4, J_5, J_6, J_7, J_8\} = \int_{-b/2}^{b/2} \sum_{m\in\{b,c,u\}} \int_{z_m^-}^{z_m^+} \rho\, F_5(z)\, dz\, dy, \tag{66}$$

where we define

$$F_5(z) = \left(1,\ z,\ f,\ zf,\ z^2,\ f^2,\ g^2,\ g\right),$$

4 Magneto-Electro Bilaterally Coated Functionally Graded (MEBCFG) Microbeams.

This section considers a microbeam of length L, width b, and thickness h, as shown in figure 15, from which the material characteristics are progressively graded from the outer surfaces to the inner core.

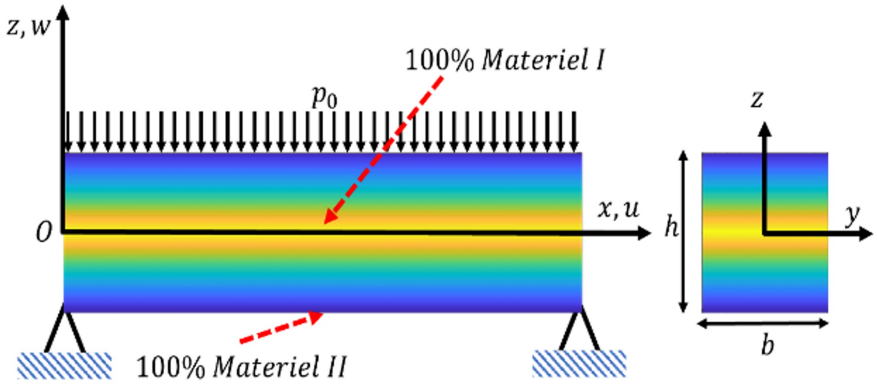


Figure 15: MEBCFG microbeam model

The material characteristics are considered to change continuously in two opposite direction throughout the thickness (z-axis) based on the power-law distribution [61]. The following equations describe the distribution of material characteristics in FG materials:

$$P\left(z\right) = \left(P_1 - P_2\right)\left(\left|\left|\frac{2z}{h}\right| - 1\right|\right)^{k_z} + P_2 \tag{67}$$

The boundaries borne of the stiffness coefficients in equations 57, 58 according to the MEBCFG Microbeam model are as follows, where $z \in z^{\pm} = \left[-\frac{h}{2}, \frac{h}{2}\right]$ and $y \in y^{\pm} = \left[-\frac{b}{2}, \frac{b}{2}\right]$.

$$
\begin{cases}
\{I_{1:6}\} = \int_{-b/2}^{b/2}\int_{-h/2}^{h/2} C_{11}\,(1, z, f, zf, z^2, f^2)\,dz\,dy, \\
\{I_{7}\} = \int_{-b/2}^{b/2}\int_{-h/2}^{h/2} C_{33}\left(\frac{dg}{dz}\right)^2 dz\,dy, \\
\{I_{8:10}\} = \int_{-b/2}^{b/2}\int_{-h/2}^{h/2} C_{13}\,\frac{dg}{dz}\,(1, z, f)\,dz\,dy, \\
\{I_{11}\} = \int_{-b/2}^{b/2}\int_{-h/2}^{h/2} C_{55}\,g^2\,dz\,dy, \\
\{I_{12:14}\} = \int_{-b/2}^{b/2}\int_{-h/2}^{h/2} e_{31}\,\frac{\pi}{h}\sin\left(\frac{\pi z}{h}\right)(1, z, f)\,dz\,dy, \\
\{I_{15:17}\} = \int_{-b/2}^{b/2}\int_{-h/2}^{h/2} q_{31}\,\frac{\pi}{h}\sin\left(\frac{\pi z}{h}\right)(1, z, f)\,dz\,dy, \\
\{I_{18:19}\} = \int_{-b/2}^{b/2}\int_{-h/2}^{h/2} g\,\frac{\pi}{h}\cos\left(\frac{\pi z}{h}\right)(e_{15}, q_{15})\,dz\,dy, \\
\{I_{20:21}\} = \int_{-b/2}^{b/2}\int_{-h/2}^{h/2} \frac{dg}{dz}\,\frac{\pi}{h}\sin\left(\frac{\pi z}{h}\right)(e_{33}, q_{33})\,dz\,dy, \\
\{I_{22:24}\} = \int_{-b/2}^{b/2}\int_{-h/2}^{h/2} \left(\frac{\pi}{h}\cos\left(\frac{\pi z}{h}\right)\right)^2(s_{11}, \mu_{11}, d_{11})\,dz\,dy, \\
\{I_{25:27}\} = \int_{-b/2}^{b/2}\int_{-h/2}^{h/2} \left(\frac{\pi}{h}\sin\left(\frac{\pi z}{h}\right)\right)^2(s_{33}, \mu_{33}, d_{33})\,dz\,dy.
\end{cases}
\tag{68}
$$

$$
\begin{cases}
\{D_{1:3}\} = \int_{-b/2}^{b/2}\int_{-h/2}^{h/2} \frac{1}{4}A_{44}\left(\frac{d^2f}{dz^2},\ \left(\frac{dg}{dz}\right)^2,\ \frac{d^2f}{dz^2}\frac{dg}{dz}\right) dz\,dy, \\
\{D_{4:9}\} = \int_{-b/2}^{b/2}\int_{-h/2}^{h/2} \frac{1}{4}A_{66}\left(1,\ \frac{df}{dz}+1,\ g,\ g\left(\frac{df}{dz}+1\right),\ \left(\frac{df}{dz}+1\right)^2,\ g^2\right) dz\,dy.
\end{cases}
\tag{69}
$$

The inertia coefficients in equation 60 are as follow according to the MEBCFG microbeam model :

$$
\{J_1, \ldots, J_8\} = \int_{-b/2}^{b/2}\int_{-h/2}^{h/2} \rho\,(1, z, f, zf, z^2, f^2, g^2, g)\,dz\,dy. \tag{70}
$$

5 Magneto-Electro Bi-Coated Functionally Graded (MEBiCFG) Microbeams.

This section considers a microbeam of length L, width b, and thickness h, as shown in figure 16 and 17 , from which the microbeam is composed of a MEE core and non-piezo material in the surface.

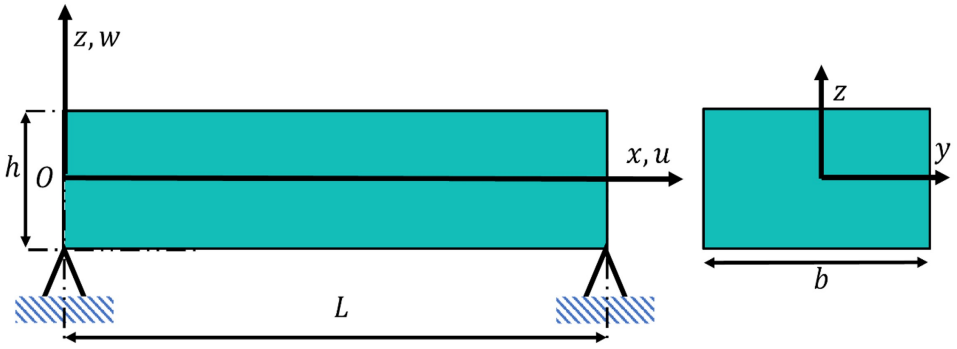


Figure 16: MEBiCFG microbeam model

The material characteristics are considered to change continuously in two direction throughout the thickness (z-axis) and the width (y-axis) from the core to the external surface based on the power-law distribution [196]. This study considers bi-coated FG distribution pattern figure 17:

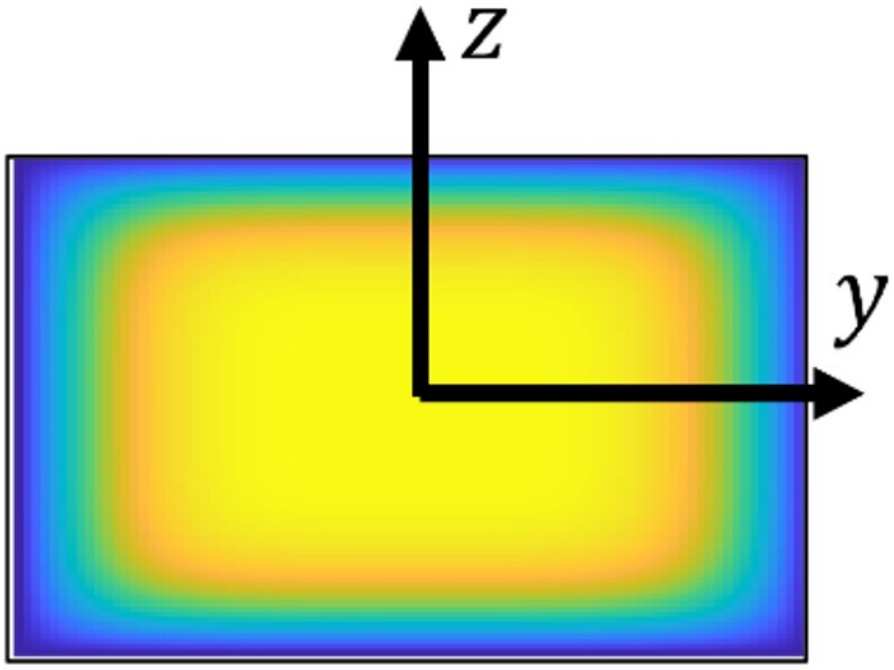


Figure 17: FG distribution pattern

The following equations describe the distribution of material characteristics in FG materials [196]:

$$P(z) = (P_1 - P_2) V_{FG}(z) + P_2 \tag{71}$$

$$V_{FG-A}(z) = \left[\left(\frac{|2z|}{h} \right)^{k_z} - 1 \right] \left[\left(\frac{|2y-b|}{b} \right)^{k_y} - 1 \right] \tag{72}$$

The boundaries borne of the stiffness coefficients in equations 57, 58 according to the MEBiCFG Microbeam model are the same as the MEBCFG Microbeam model, and also the inertia coefficients in equation 60, where $z \in z^{\pm} = \left[-\frac{h}{2}, \frac{h}{2}\right]$ and $y \in y^{\pm} = \left[-\frac{b}{2}, \frac{b}{2}\right]$.

6 Conclusion

In this chapter, a comprehensive variational formulation was established for magneto-electro functionally graded microbeams. Utilizing a quasi-3D beam theory, which inherently accounts for transverse shear and thickness stretching effects without the need for shear correction factors, the expressions for kinetic energy, strain energy, and virtual work were meticulously derived. Three distinct configurations—namely, Magneto-Electro Functionally Graded Sandwich, Bilaterally Coated, and Bi-Coated Microbeams, were specifically addressed, providing a versatile framework. This detailed formulation lays the groundwork for subsequent derivation of governing equations and in-depth analysis of the static and dynamic responses of these advanced MEE microstructures.

Chapter VI: Numerical Implementation using the Differential Quadrature Finite Element Method (DQ-FEM)

1 Introduction

In the preceding chapter, a comprehensive variational formulation was established for magneto-electro functionally graded (MEE-FG) microbeams based on a quasi-3D beam theory. The derived expressions for kinetic energy, strain energy, and virtual work have set the foundation for the numerical implementation. In this chapter, attention is directed toward the **Differential Quadrature Finite Element Method (DQ-FEM)**, a powerful hybrid numerical technique that integrates the accuracy and efficiency of the Generalized Differential Quadrature Method (GDQM) with the versatility of the Finite Element Method (FEM).

The primary motivation behind adopting DQ-FEM lies in its ability to achieve **spectral-like accuracy** with relatively few nodes, while retaining the structural flexibility of FEM. This makes it particularly suitable for modeling the static and dynamic responses of MEE-FG microbeams, where strong coupling between mechanical, electrical, magnetic, and thermal fields demands both robustness and efficiency.

2 Formulation of the DQ-FEM

2.1 Differential Quadrature Approximation

The essence of DQ is that the derivative of a function at a given point can be expressed as a weighted linear sum of the function values at all discrete sampling points within the domain. For an arbitrary displacement or potential field $q(x)$, we assume [57, 59, 60, 61, 62]:

$$q(x) = \sum_{i=1}^{N} L_i(x)\, q_i, \tag{73}$$

where $L_i(x)$ denotes the Lagrange interpolation polynomial, and $q_i = q(x_i)$ are the nodal values of the unknown variables (e.g., displacements u, w_b, w_s, w_z, electric potential γ, and magnetic potential ζ).

The n^{th}-order derivative of a field variable $F(x,t)$ at a discrete point x_i is approximated as:

$$\left.\frac{\partial^n F(x,t)}{\partial x^n}\right|_{x_i} = \sum_{j=1}^{N} A_{ij}^{(n)} F(x_j,t), \quad i = 1, 2, \ldots, N, \tag{74}$$

where $A_{ij}^{(n)}$ are the weighting coefficients of the n^{th}-order derivative.

2.2 Weighting Coefficients

The weighting coefficients $A_{ij}^{(n)}$ are related to the derivatives of the Lagrange interpolation functions. They are obtained as follows:

For the **first derivative** ($n = 1$):

$$A_{ij}^{(1)} = \frac{M(x_i)}{(x_i - x_j)M(x_j)}, \quad i \neq j, \quad i, j = 1, 2, \ldots, N, \tag{75}$$

$$A_{ii}^{(1)} = -\sum_{\substack{j=1 \\ j\neq i}}^{N} A_{ij}^{(1)}, \quad i = 1, 2, \ldots, N, \tag{76}$$

where

$$M(x_i) = \prod_{\substack{k=1 \\ k\neq i}}^{N} (x_i - x_k), \quad M(x_j) = \prod_{\substack{k=1 \\ k\neq j}}^{N} (x_j - x_k). \tag{77}$$

For **higher-order derivatives** ($n > 1$), the coefficients are computed by the recurrence relation:

$$A_{ij}^{(n)} = n \left(A_{ij}^{(1)} A_{ii}^{(n-1)} - \frac{A_{ij}^{(n-1)}}{(x_i - x_j)} \right), \quad i \neq j, \ i, j = 1, 2, \ldots, N, \ n > 1, \tag{78}$$

$$A_{ii}^{(n)} = -\sum_{\substack{j=1 \\ j\neq i}}^{N} A_{ij}^{(n)}, \quad i = 1, 2, \ldots, N. \tag{79}$$

2.3 Gauss–Lobatto Quadrature Rule

To evaluate integrals in the weak form, the Gauss–Lobatto quadrature rule is adopted:

$$\int_{-1}^{1} F(x)\, dx = \sum_{j=1}^{N} C_j F(x_j), \tag{80}$$

where C_j are the quadrature weights, given by:

$$C_1 = C_N = \frac{2}{N(N-1)}, \quad C_j = \frac{2}{N(N-1)[P_{N-1}(x_j)]^2}, \quad j \neq 1, N, \tag{81}$$

and x_j are the Gauss–Lobatto nodes:

$$x_j = -\cos\left(\frac{j-1}{N-1}\pi\right). \tag{82}$$

The nodes are determined from the roots of the derivative of the Legendre polynomials, which are computed by the recurrence relation:

$$P_{N+1}(x) = \frac{2N+1}{N+1} x P_N(x) - \frac{N}{N+1} P_{N-1}(x), \tag{83}$$

with

$$P_0(x) = 1, \quad P_1(x) = x. \tag{84}$$

The higher-order derivatives of Legendre polynomials can also be determined using the recurrence formula:

$$P_{N+1}^{(n)}(x) = xP_N^{(n)}(x) + (N+n)P_N^{(n)}(x). \tag{85}$$

2.4 Transformation Matrix and Nodal Relations

In DQ-FEM, the relations between the field variables and their interpolated values are expressed as:

$$u = Q\bar{u}, \quad w_b = Q\bar{w}_b, \quad w_s = Q\bar{w}_s, \quad \gamma = Q\bar{\gamma}, \quad \zeta = Q\bar{\zeta}, \tag{86}$$

where Q is the transformation matrix:

$$Q = \begin{bmatrix} 1 & 0 & 0 & \cdots & 0 & 0 \\ A_{1,1}^{(1)} & A_{1,2}^{(1)} & A_{1,3}^{(1)} & \cdots & A_{1,N-1}^{(1)} & A_{1,N}^{(1)} \\ 0 & 0 & 1 & \cdots & 0 & 0 \\ \vdots & \vdots & \vdots & \ddots & \vdots & \vdots \\ 0 & 0 & 0 & \cdots & 0 & 1 \\ A_{N,1}^{(1)} & A_{N,2}^{(1)} & A_{N,3}^{(1)} & \cdots & A_{N,N-1}^{(1)} & A_{N,N}^{(1)} \end{bmatrix} \tag{87}$$

All types of nodal arrangement for differentiation and quadrature reside inside the interval $[-1, 1]$. Consequently, to implement them in practice, the subsequent adjustments from the interval $[0, l_e]$ to $[-1, 1]$ must be applied to the differential and quadrature matrices.

$$\bar{C} = \frac{l_e}{2}C, \qquad \bar{A}^1 = \frac{2}{l_e}A^1, \qquad \bar{A}^2 = \frac{4}{{l_e}^2}A^2 \tag{88}$$

Were l_e is the length of the microbeam element.

3 Element Matrices

By substituting the above approximations into the variational formulation (strain (equation 56), kinetic (equation 59) , and virtual works (equation 61) derived in Chapter 5).

Strain energy (DQ-FEM implementation)

$$
\begin{aligned}
U = \tfrac{1}{2}\Big(& I_1\Big[Q^T {A^1}^T C A^1 Q\Big]u^2 - 2I_2\Big[Q^T {A^1}^T C A^2 Q\Big]uw_b - 2I_3\Big[Q^T {A^1}^T C A^2 Q\Big]uw_s \\
& + 2I_4\Big[Q^T {A^2}^T C A^2 Q\Big]w_b w_s + I_5\Big[Q^T {A^2}^T C A^2 Q\Big]w_b^2 + I_6\Big[Q^T {A^2}^T C A^2 Q\Big]w_s^2 \\
& + I_7\Big[Q^T C Q\Big]w_z^2 + 2I_8\Big[Q^T {A^1}^T C Q\Big]uw_z - 2I_9\Big[Q^T {A^2}^T C Q\Big]w_b w_z \\
& - 2I_{10}\Big[Q^T {A^2}^T C Q\Big]w_s w_z + I_{11}\Big[Q^T {A^1}^T C A^1 Q\Big]\Big(w_s^2 + w_z^2 + 2w_s w_z\Big) \\
& + 2I_{12}\Big[Q^T {A^1}^T C Q\Big]u\gamma - 2I_{13}\Big[Q^T {A^2}^T C Q\Big]w_b\gamma - 2I_{14}\Big[Q^T {A^2}^T C Q\Big]w_s\gamma \\
& + 2I_{15}\Big[Q^T {A^1}^T C Q\Big]u\zeta - 2I_{16}\Big[Q^T {A^2}^T C Q\Big]w_b\zeta - 2I_{17}\Big[Q^T {A^2}^T C Q\Big]w_s\zeta \\
& - 2I_{18}\Big[Q^T {A^1}^T C A^1 Q\Big](w_s\gamma - w_z\gamma) - 2I_{19}\Big[Q^T {A^1}^T C A^1 Q\Big](w_s\zeta - w_z\zeta) \\
& + 2I_{20}\Big[Q^T C Q\Big]w_z\gamma + 2I_{21}\Big[Q^T C Q\Big]w_z\zeta - I_{22}\Big[Q^T {A^1}^T C A^1 Q\Big]\gamma^2 \\
& - I_{23}\Big[Q^T {A^1}^T C A^1 Q\Big]\zeta^2 - 2I_{24}\Big[Q^T {A^1}^T C A^1 Q\Big]\gamma\zeta - I_{25}\Big[Q^T C Q\Big]\gamma^2 \\
& - I_{26}\Big[Q^T C Q\Big]\zeta^2 - 2I_{27}\Big[Q^T C Q\Big]\gamma\zeta + D_1\Big[Q^T {A^1}^T C A^1 Q\Big]w_s^2 \\
& + D_2\Big[Q^T {A^1}^T C A^1 Q\Big]w_z^2 + 2D_3\Big[Q^T {A^1}^T C A^1 Q\Big]w_s w_z + 4D_4\Big[Q^T {A^2}^T C A^2 Q\Big]w_b^2 \\
& + 4D_5\Big[Q^T {A^2}^T C A^2 Q\Big]w_b w_s + 4D_6\Big[Q^T {A^2}^T C A^2 Q\Big]w_b w_z + 2D_7\Big[Q^T {A^2}^T C A^2 Q\Big]w_s w_z \\
& + D_8\Big[Q^T {A^2}^T C A^2 Q\Big]w_s^2 + D_9\Big[Q^T {A^2}^T C A^2 Q\Big]w_z^2\Big).
\end{aligned}
\tag{89}
$$

Kinetic energy (DQ-FEM implementation)

$$
\begin{aligned}
T = \frac{1}{2}\Big(& J_1\Big[G^T C G\Big]\Big(\dot{u}^2 + \dot{w}_b^2 + \dot{w}_s^2 + 2\dot{w}_b\dot{w}_s\Big) - 2J_2\Big[G^T C {A^{(1)}} G\Big]\dot{u}\dot{w}_b - 2J_3\Big[G^T C {A^{(1)}} G\Big]\dot{u}\dot{w}_s \\
& + 2J_4\Big[G^T {A^{(1)}}^T C A^{(1)} G\Big]\dot{w}_b\dot{w}_s + J_5\Big[G^T {A^{(1)}}^T C A^{(1)} G\Big]\dot{w}_b^2 + J_6\Big[G^T {A^{(1)}}^T C A^{(1)} G\Big]\dot{w}_s^2 \\
& + J_7\Big[G^T C G\Big]\dot{w}_z^2 + 2J_8\Big[G^T C G\Big]\Big(\dot{w}_b\dot{w}_z + \dot{w}_s\dot{w}_z\Big)\Big)
\end{aligned}
\tag{90}
$$

Virtual works (DQ-FEM implementation)

$$
W_{ext} = -q_0\left(\Big[Q^T C\Big]\, w_b + \Big[Q^T C\Big]\, w_s + f_2\Big[Q^T C\Big]\, w_z\right) \tag{91}
$$

The governing equations are obtained by applying **Lagrange's principle** to the discretized DQ-FEM formulation. For each element, the vector of generalized nodal variables is defined as

$$\{\bar{q}^e\} = \left\{\bar{u}, \bar{w}_b, \bar{w}_s, \bar{w}_z, \bar{\gamma}, \bar{\zeta}\right\}^T, \tag{92}$$

where $\bar{u}$ is the axial displacement vector, $\bar{w}_b$ is the bending component of the transverse displacement, $\bar{w}_s$ is the shear component, $\bar{w}_z$ is the thickness-stretching displacement, while $\bar{\gamma}$ and $\bar{\zeta}$ denote the electric and magnetic potential vectors, respectively.

The Lagrangian of the element is written as

$$\mathcal{L}^e = T^e - U^e, \tag{93}$$

where T^e is the kinetic energy and U^e is the strain energy of the element. The contribution of the external mechanical loading is introduced through the virtual work δW^e_{ext}. Therefore, Lagrange's equation for each generalized coordinate $\bar{q}^e_i$ is expressed as

$$\frac{d}{dt}\left(\frac{\partial \mathcal{L}^e}{\partial \dot{\bar{q}}^e_i}\right) - \frac{\partial \mathcal{L}^e}{\partial \bar{q}^e_i} = F^e_i, \qquad i = 1, 2, \ldots, n_e, \tag{94}$$

where $\dot{\bar{q}}^e_i$ is the time derivative of the generalized coordinate, F^e_i is the corresponding generalized external force, and n_e is the total number of generalized degrees of freedom of the element.

Using the discretized expressions of the kinetic and strain energies, the element energies can be written in quadratic matrix form as

$$T^e = \frac{1}{2}\{\dot{\bar{q}}^e\}^T [M^e] \{\dot{\bar{q}}^e\}, \tag{95}$$

and

$$U^e = \frac{1}{2}\{\bar{q}^e\}^T [K^e] \{\bar{q}^e\}, \tag{96}$$

where $[M^e]$ and $[K^e]$ are the elementary mass and stiffness matrices, respectively. The external virtual work is written as

$$\delta W^e_{\text{ext}} = \{\delta \bar{q}^e\}^T \{F^e\}, \tag{97}$$

where $\{F^e\}$ is the elementary external load vector.

Substituting Eqs. (95)–(97) into Lagrange's equation gives the elementary equations of motion:

$$[M^e]\{\ddot{\bar{q}}^e\} + [K^e]\{\bar{q}^e\} = \{F^e\}. \tag{98}$$

It should be noted that the electric and magnetic potentials, $\bar{\gamma}$ and $\bar{\zeta}$, do not contribute to the kinetic energy. Consequently, the corresponding rows and columns in the mass matrix associated with these potential variables are equal to zero, while their coupling with the mechanical field appears through the stiffness matrix.

For free vibration analysis, the external load vector is set to zero and the generalized displacement vector is assumed to be harmonic:

$$\{\bar{q}^e(t)\} = \{\hat{q}^e\}e^{i\omega t}, \tag{99}$$

where $\{\hat{q}^e\}$ is the amplitude vector, ω is the natural circular frequency, and $i = \sqrt{-1}$. Substituting Eq. (99) into Eq. (98) leads to the elementary eigenvalue problem:

$$\left([K^e] - \omega^2[M^e]\right)\{\hat{q}^e\} = \{0\}. \tag{100}$$

After assembling all elementary matrices using the standard finite element procedure, the global governing equation is obtained as

$$[M]\{\ddot{\bar{q}}\} + [K]\{\bar{q}\} = \{F\}, \tag{101}$$

For harmonic free vibration, it becomes

$$\left([K] - \omega^2[M]\right)\{\hat{q}\} = \{0\}. \tag{102}$$

For static bending, it becomes

$$[K]\{\bar{q}\} = \{F\},. \tag{103}$$

The **elementary mass matrix** is:

$$[M^e] = \begin{bmatrix} [M^e]_{11} & [M^e]_{12} & [M^e]_{13} & 0 & 0 & 0 \\ & [M^e]_{22} & [M^e]_{23} & [M^e]_{24} & 0 & 0 \\ & & [M^e]_{33} & [M^e]_{34} & 0 & 0 \\ & & & [M^e]_{44} & 0 & 0 \\ & & & & 0 & 0 \\ \text{sym} & & & & & 0 \end{bmatrix} \tag{104}$$

where the mass matrix components are as follow:

$$
\begin{aligned}
&[M^e]_{11} = J_1 \left[Q^T C Q\right], && [M^e]_{12} = -J_2 \left[Q^T C A^1 Q\right], \\
&[M^e]_{13} = -J_3 \left[Q^T C A^1 Q\right], && [M^e]_{22} = J_1 \left[Q^T C Q + J_5\, Q^T {A^1}^T C A^1 Q\right], \\
&[M^e]_{23} = J_1 \left[Q^T C Q + J_4\, Q^T {A^1}^T C A^1 Q\right], && [M^e]_{24} = J_8 \left[Q^T C Q\right], \\
&[M^e]_{33} = J_1 \left[Q^T C Q + J_6\, Q^T {A^1}^T C A^1 Q\right], && [M^e]_{34} = J_8 \left[Q^T C Q\right], \\
&[M^e]_{44} = J_7 \left[Q^T C Q\right].
\end{aligned}
\tag{105}
$$

while the **elementary strain matrix** is:

$$
[K^e] = \begin{bmatrix}
[K^e]_{11} & [K^e]_{12} & [K^e]_{13} & [K^e]_{14} & [K^e]_{15} & [K^e]_{16} \\
 & [K^e]_{22} & [K^e]_{23} & [K^e]_{24} & [K^e]_{25} & [K^e]_{26} \\
 & & [K^e]_{33} & [K^e]_{34} & [K^e]_{35} & [K^e]_{36} \\
 & & & [K^e]_{44} & [K^e]_{45} & [K^e]_{46} \\
\text{sym} & & & & [K^e]_{55} & [K^e]_{56} \\
 & & & & & [K^e]_{66}
\end{bmatrix}
\tag{106}
$$

where the strain matrix components are as follow:

$$
\begin{aligned}
[K^e]_{11} &= I_1 \left[Q^T {A^1}^T C A^1 Q\right], \\
[K^e]_{12} &= -I_2 \left[Q^T {A^1}^T C A^2 Q\right], \\
[K^e]_{13} &= -I_3 \left[Q^T {A^1}^T C A^2 Q\right], \\
[K^e]_{14} &= I_8 \left[Q^T {A^1}^T C Q\right], \\
[K^e]_{15} &= I_{14} \left[Q^T {A^1}^T C Q\right], \\
[K^e]_{16} &= I_{17} \left[Q^T {A^1}^T C Q\right], \\
[K^e]_{22} &= (I_5 + 4D_4) \left[Q^T {A^2}^T C A^2 Q\right], \\
[K^e]_{23} &= (I_4 + 2D_5) \left[Q^T {A^2}^T C A^2 Q\right], \\
[K^e]_{24} &= -I_9 \left[Q^T {A^2}^T C Q\right] + 2D_6 \left[Q^T {A^2}^T C A^2 Q\right], \\
[K^e]_{25} &= -I_{15} \left[Q^T {A^2}^T C Q\right], \\
[K^e]_{26} &= -I_{18} \left[Q^T {A^2}^T C Q\right], \\
[K^e]_{33} &= (I_6 + D_8) \left[Q^T {A^2}^T C A^2 Q\right] + (I_{11} + D_1) \left[Q^T {A^1}^T C A^1 Q\right], \\
[K^e]_{34} &= -I_{10} \left[Q^T {A^2}^T C Q\right] + (I_{13} + D_3) \left[Q^T {A^1}^T C A^1 Q\right] + D_7 \left[Q^T {A^2}^T C A^2 Q\right], \\
[K^e]_{35} &= -I_{16} \left[Q^T {A^2}^T C Q\right] - I_{20} \left[Q^T {A^1}^T C A^1 Q\right], \\
[K^e]_{36} &= -I_{19} \left[Q^T {A^2}^T C Q\right] - I_{21} \left[Q^T {A^1}^T C A^1 Q\right], \\
[K^e]_{44} &= I_7 \left[Q^T C Q\right] + (I_{12} + D_2) \left[Q^T {A^1}^T C A^1 Q\right] + D_9 \left[Q^T {A^2}^T C A^2 Q\right], \\
[K^e]_{45} &= -I_{22} \left[Q^T {A^1}^T C A^1 Q\right] + I_{24} \left[Q^T C Q\right], \\
[K^e]_{55} &= -I_{26} \left[Q^T {A^1}^T C A^1 Q\right] - I_{29} \left[Q^T C Q\right], \\
[K^e]_{56} &= -I_{28} \left[Q^T {A^1}^T C A^1 Q\right] - I_{31} \left[Q^T C Q\right], \\
[K^e]_{66} &= -I_{27} \left[Q^T {A^1}^T C A^1 Q\right] - I_{30} \left[Q^T C Q\right].
\end{aligned}
\tag{107}
$$

The external load vector takes the form:

$$[F] = \{0, F_{e2}, F_{e3}, F_{e4}, 0, 0\}^T. \tag{108}$$

Assembly of the global matrices follows the standard FEM procedure, leading to the governing equation of motion:

$$\left([K] - \omega^2 [M]\right) \{\bar{q}\} = \{F\}, \tag{109}$$

where $\bar{q} = \{\bar{u}, \bar{w}_b, \bar{w}_s, \bar{w}_z, \bar{\gamma}, \bar{\zeta}\}^T$.

4 Boundary Conditions

In DQ-FEM, mechanical, electrical, and magnetic boundary conditions are imposed similarly to FEM. This is accomplished by **eliminating rows and columns** of the global matrices associated with constrained degrees of freedom:

- **Simply Supported (S):** First and penultimate rows/columns removed.
- **Clamped (C):** First, second, penultimate, and last rows/columns removed.
- **Free (F):** No elimination applied.

For electro-magnetic constraints:

$$\gamma = 0, \quad \zeta = 0 \quad \text{at clamped and simply supported ends.}$$

This ensures that both displacement and potential boundary conditions are accurately enforced within the numerical model.

5 Concluding Remarks

This chapter presented the **numerical implementation of the quasi-3D variational formulation** of MEE-FG microbeams using DQ-FEM. The method combines the **accuracy of spectral methods** with the **flexibility of FEM**, enabling efficient and robust modeling of static and dynamic responses. The derived mass and stiffness matrices provide the foundation for subsequent **parametric studies and validation**, which will be detailed in the following chapter.

Chapter VII:
Numerical results and discussion

1 Introduction

The preceding chapters have meticulously detailed the theoretical formulation of three distinct magneto-electro-elastic functionally graded (MEE-FGM) microbeam models namely the *sandwich*, the *bilaterally coated*, and the *bi-coated* configurations. A robust computational framework was established by integrating a refined quasi-3D/higher-order beam theory with the Modified Couple Stress Theory (MCST) to capture both macroscopic deformations and microscopic size effects. The governing equations, derived via Lagrange's principle, were subsequently discretized and solved using the highly efficient Differential Quadrature Finite Element Method (DQ-FEM).

This chapter now transitions from the development of the model to its application and validation. It serves as the cornerstone of the thesis, where the predictive capabilities of the proposed framework are rigorously tested and utilized to generate new scientific insights into the complex behavior of these advanced microstructures. The primary objectives of this chapter are twofold: first, to establish the accuracy and reliability of the developed numerical models through a series of validation and convergence studies against established literature; and second, to conduct a comprehensive parametric investigation into the static bending and free vibration responses of each microbeam configuration.

To achieve these objectives, the chapter is structured as follows. It begins with a crucial validation section to confirm the integrity of the proposed DQ-FEM code. Subsequently, the main body of the chapter is divided into three distinct sections, each dedicated to one of the developed microbeam models. Within each section, a detailed analysis of both static deflection under magneto-electro-mechanical loads and free vibration characteristics will be presented. The influence of key design parameters—including the material gradation index (p), the length-to-thickness ratio (L/h), the material length scale parameter, and the MEE material composition—will be systematically investigated and discussed. Ultimately, the results presented herein aim to provide a deep understanding of the coupled multi-physics behavior of these microbeams and offer valuable guidelines for the design and optimization of next-generation micro-electromechanical systems (MEMS), such as sensors, actuators, and energy harvesters.

2 Model Validation and Convergence Study

In this section, based on literature works [10, 13, 197] the model used is a simply supported (S-S) FG microbeam assumed to be composed of $50\% - 50\% BaTiO_3 - CoFe_2O_4$ and epoxy [198]. A uniform continuous load $q_0 = 1/2000h\ N/m$ is applied on the microbeam along the Oz axis. The shape cross section is taken as $(b = 2h)$ and $(L = 20h)$, and $(h = 14.42\ \mu m)$. The material properties a indicated in table 4.

Table 4: Material properties of $BaTiO_3 - CoFe_2O_4$ and epoxy.

	$BaTiO_3 - CoFe_2O_4$							Epoxy
Property	0%-100%	20%-80%	40%-60%	50%-50%	60%-40%	80%-20%	100%-0%	
C_{11}	286	262	238	226	214	190	166	4.889
C_{13}	170	151.6	133.2	124	114.8	96.4	78	2.407
C_{33}	269.5	248	226.5	215.75	205	183.5	162	4.889
C_{55}	45.3	44.84	44.38	44.15	43.92	43.46	43	1.241
q_{31}	580.3	464.24	348.18	290.15	232.12	116.06	0	0
q_{33}	699.7	559.76	419.82	349.85	279.88	139.94	0	0
q_{15}	550	440	330	275	220	110	0	0
e_{31}	0	-0.88	-1.76	-2.2	-2.64	-3.52	-4.4	0
e_{33}	0	3.72	7.44	9.3	11.16	14.88	18.6	0
e_{15}	0	2.32	4.64	5.8	6.96	9.28	11.6	0
s_{11}	0.08	2.3	4.53	5.64	6.75	8.98	11.2	0
s_{33}	0.093	2.59	5.1	6.35	7.6	10.1	12.6	0
d_{11}	0	2.6	4.58	5.38	6.02	7.04	0	0
d_{33}	0	2020	2760	2740	2520	1550	0	0
μ_{11}	590	473	356	297.5	239	122	5	0
μ_{33}	157	127.6	98	83.5	68.8	39.4	10	0
ρ	5300	5400	5500	5550	5600	5700	5800	1180
MLSP	7.33	7.29	7.24	7.21	7.18	7.1	7	16.93

The units in table 4 are as follow: the piezoelectric constants are given in e_{ij} (C/m^2) , the dielectric constants are given in $s_{ij}(10^{-9}C^2/(N.m^2))$, the piezomagnetic constants are given in $q_{ij}(N/(A.m))$, the magnetoelectric constants are given in $d_{ij}(10^{-12}Ns/(V.C))$, the magnetic constants are given in $\mu_{ij}(10^{-6}Ns^2/C^2)$, and the density is given in $\rho(kg/m^3)$. The material length scale parameter is given in l (μm).

2.1 convergence analysis

To demonstrate the accuracy and high computational efficiency of the proposed numerical method a convergence study is done figures 18, 19, 20, 21 and table 5, 6, 7.

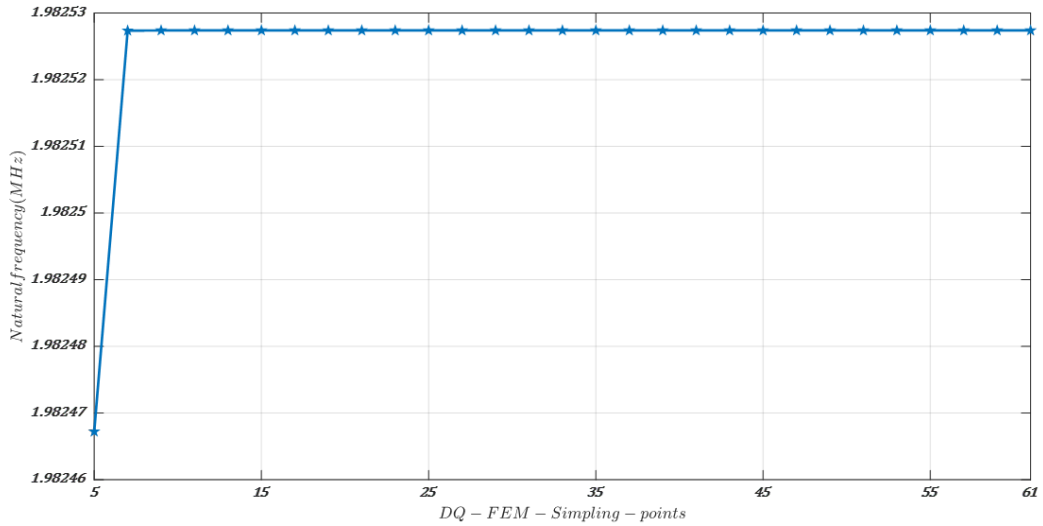


Figure 18: Convergence of the 1st frequency for a simply supported ME bilaterally coated FG microbeam,$k = 1, h = 20\mu m, b = 2h, L = 20h, BaTiO_3(50\%) - CoFe_2O_4(50\%)$

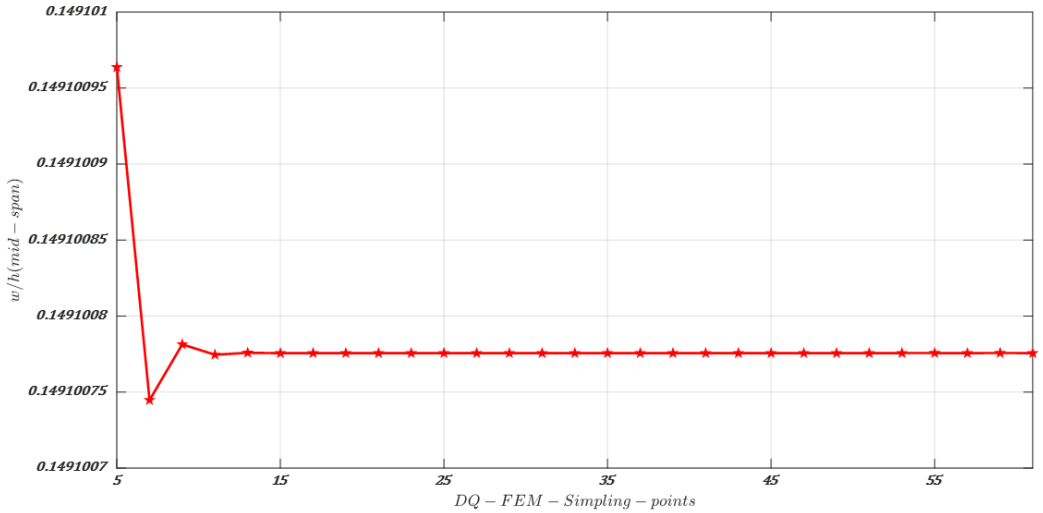


Figure 19: Convergence of the mid span deflection for a simply supported ME bilaterally coated FG microbeam,$k = 1, h = 20\mu m, b = 2h, L = 20h, BaTiO_3(50\%) - CoFe_2O_4(50\%)$

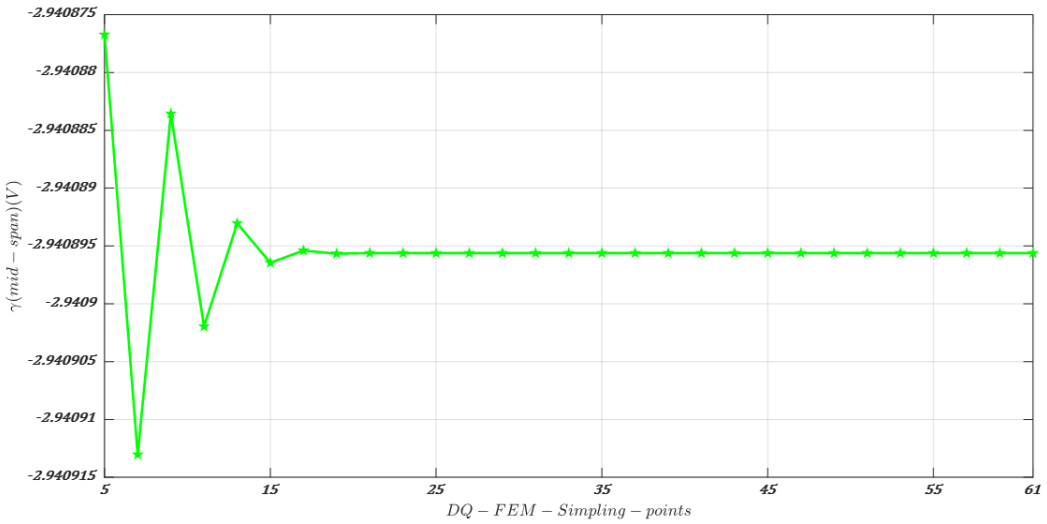


Figure 20: Convergence of the mid span electric potential for a simply supported ME bilaterally coated FG microbeam,$k = 1, h = 20\mu m, b = 2h, L = 20h, BaTiO_3(50\%) - CoFe_2O_4(50\%)$

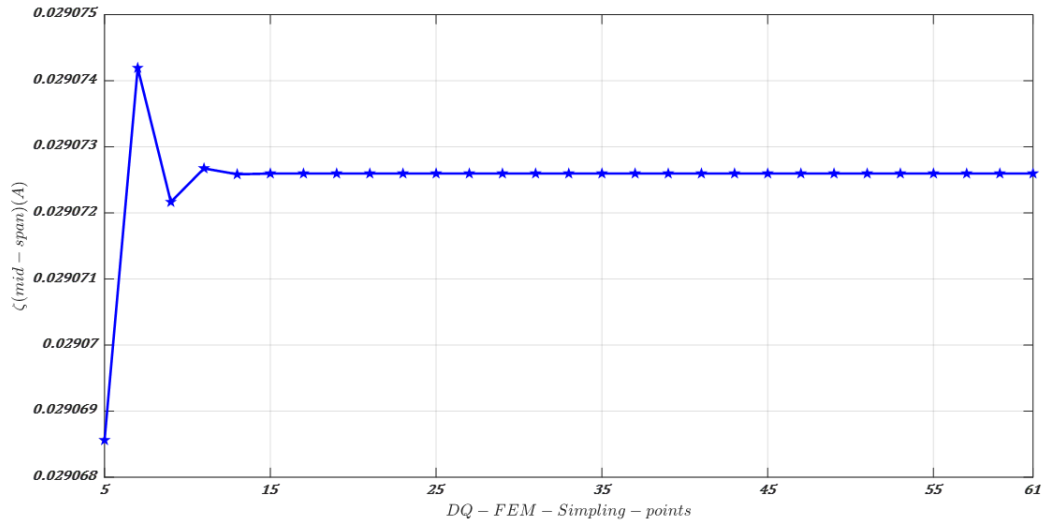


Figure 21: Convergence of the mid span magnetic potential for a simply supported ME bilaterally coated FG microbeam,$k = 1, h = 20\mu m, b = 2h, L = 20h, BaTiO_3(50\%) - CoFe_2O_4(50\%)$

PS: The convergence results for all the microbeams models have a similar allure.

A convergence study was systematically conducted to check the numerical stability and accuracy of the proposed models. The analysis showed that all of the microbeam configurations studied in this work converged very quickly and well. Based on these results, it was decided that 61 sampling points for the Differential Quadrature

Table 5: Convergence results for the simply supported beam (SS) with respect to the number of sampling points N_s.

N_s	$f_1(MHz)$	$f_2(MHz)$	$f_3(MHz)$	w/h	$\gamma(V)$	$\zeta(A)$
5	1.982	10.061	21.538	0.149	-2.941	0.029
7	1.983	7.947	17.840	0.149	-2.941	0.029
9	1.983	7.914	17.745	0.149	-2.941	0.029
11	1.983	7.914	17.607	0.149	-2.941	0.029
13	1.983	7.914	16.611	0.149	-2.941	0.029
15	1.983	7.914	16.255	0.149	-2.941	0.029
17	1.983	7.914	16.151	0.149	-2.941	0.029
19	1.983	7.914	16.120	0.149	-2.941	0.029
21	1.983	7.914	16.121	0.149	-2.941	0.029
23	1.983	7.914	16.120	0.149	-2.941	0.029
25	1.983	7.914	16.120	0.149	-2.941	0.029
27	1.983	7.914	16.120	0.149	-2.941	0.029
29	1.983	7.914	16.120	0.149	-2.941	0.029
31	1.983	7.914	16.120	0.149	-2.941	0.029
33	1.983	7.914	16.120	0.149	-2.941	0.029
35	1.983	7.914	16.120	0.149	-2.941	0.029
37	1.983	7.914	16.120	0.149	-2.941	0.029
39	1.983	7.914	16.120	0.149	-2.941	0.029
41	1.983	7.914	16.120	0.149	-2.941	0.029
43	1.983	7.914	16.120	0.149	-2.941	0.029
45	1.983	7.914	16.120	0.149	-2.941	0.029
47	1.983	7.914	16.120	0.149	-2.941	0.029
49	1.983	7.914	16.120	0.149	-2.941	0.029
51	1.983	7.914	16.120	0.149	-2.941	0.029
53	1.983	7.914	16.120	0.149	-2.941	0.029
55	1.983	7.914	16.120	0.149	-2.941	0.029
57	1.983	7.914	16.120	0.149	-2.941	0.029
59	1.983	7.914	16.120	0.149	-2.941	0.029
61	1.983	7.914	16.120	0.149	-2.941	0.029

Table 6: Convergence results for the clamped–clamped beam (CC) with respect to the number of sampling points N_s.

N_s	$f_1(MHz)$	$f_2(MHz)$	$f_3(MHz)$	w/h	$\gamma(V)$	$\zeta(A)$
5	50.272	143.095	26.000	0.030	-0.723	0.007
7	4.493	12.610	24.501	0.030	-1.153	0.011
9	4.493	12.361	24.152	0.030	-0.863	0.009
11	4.493	12.357	24.136	0.030	-1.042	0.010
13	4.493	12.357	24.136	0.030	-0.925	0.009
15	4.493	12.357	24.136	0.030	-1.007	0.010
17	4.493	12.357	24.136	0.030	-0.946	0.009
19	4.493	12.357	24.136	0.030	-0.993	0.010
21	4.493	12.357	24.136	0.030	-0.955	0.009
23	4.493	12.357	24.136	0.030	-0.987	0.009
25	4.493	12.357	24.136	0.030	-0.960	0.009
27	4.493	12.357	24.136	0.030	-0.983	0.009
29	4.493	12.357	24.136	0.030	-0.963	0.009
31	4.493	12.357	24.136	0.030	-0.980	0.009
33	4.493	12.357	24.136	0.030	-0.965	0.009
35	4.493	12.357	24.136	0.030	-0.979	0.009
37	4.493	12.357	24.136	0.030	-0.967	0.009
39	4.493	12.357	24.136	0.030	-0.977	0.009
41	4.493	12.357	24.136	0.030	-0.968	0.009
43	4.493	12.357	24.136	0.030	-0.976	0.009
45	4.493	12.357	24.136	0.030	-0.969	0.009
47	4.493	12.357	24.136	0.030	-0.976	0.009
49	4.493	12.357	24.136	0.030	-0.969	0.009
51	4.493	12.357	24.136	0.030	-0.975	0.009
53	4.493	12.357	24.136	0.030	-0.970	0.009
55	4.493	12.357	24.136	0.030	-0.975	0.009
57	4.493	12.357	24.136	0.030	-0.970	0.009
59	4.493	12.357	24.136	0.030	-0.974	0.009
61	4.493	12.357	24.136	0.030	-0.970	0.009

Table 7: Convergence results for the clamped–free beam (CF) with respect to the number of sampling points N_s.

N_s	$f_1(MHz)$	$f_2(MHz)$	$f_3(MHz)$	w/h	$\gamma(V)$	$\zeta(A)$
5	0.707	4.435	21.562	0.509	-4.686	0.046
7	0.707	4.419	12.641	0.508	-2.158	0.023
9	0.707	4.419	12.338	0.508	-3.394	0.033
11	0.707	4.419	12.335	0.507	-2.712	0.028
13	0.707	4.419	12.335	0.507	-3.134	0.031
15	0.707	4.419	12.335	0.507	-2.847	0.029
17	0.707	4.419	12.335	0.507	-3.057	0.031
19	0.707	4.419	12.335	0.507	-2.894	0.030
21	0.707	4.419	12.335	0.507	-3.026	0.031
23	0.707	4.419	12.335	0.507	-2.916	0.030
25	0.707	4.419	12.335	0.507	-3.008	0.030
27	0.707	4.419	12.335	0.507	-2.930	0.030
29	0.707	4.419	12.335	0.507	-2.998	0.030
31	0.707	4.419	12.335	0.507	-2.939	0.030
33	0.707	4.419	12.335	0.507	-2.990	0.030
35	0.707	4.419	12.335	0.507	-2.945	0.030
37	0.707	4.419	12.335	0.507	-2.985	0.030
39	0.707	4.419	12.335	0.507	-2.949	0.030
41	0.707	4.419	12.335	0.507	-2.981	0.030
43	0.707	4.419	12.335	0.507	-2.952	0.030
45	0.707	4.419	12.335	0.507	-2.979	0.030
47	0.707	4.419	12.335	0.507	-2.955	0.030
49	0.707	4.419	12.335	0.507	-2.976	0.030
51	0.707	4.419	12.335	0.507	-2.957	0.030
53	0.707	4.419	12.335	0.507	-2.975	0.030
55	0.707	4.419	12.335	0.507	-2.958	0.030
57	0.707	4.419	12.335	0.507	-2.973	0.030
59	0.707	4.419	12.335	0.507	-2.959	0.030
61	0.707	4.419	12.335	0.507	-2.972	0.030

Finite Element Method (DQFEM) were enough to get a stable and correct answer. Consequently, this value was utilised for all resulting parametric studies to guarantee both elevated accuracy and computational efficacy.

2.2 validation

Rigorous validation of the DQ-FEM code by comparing results for simplified cases against published analytical and numerical solutions.

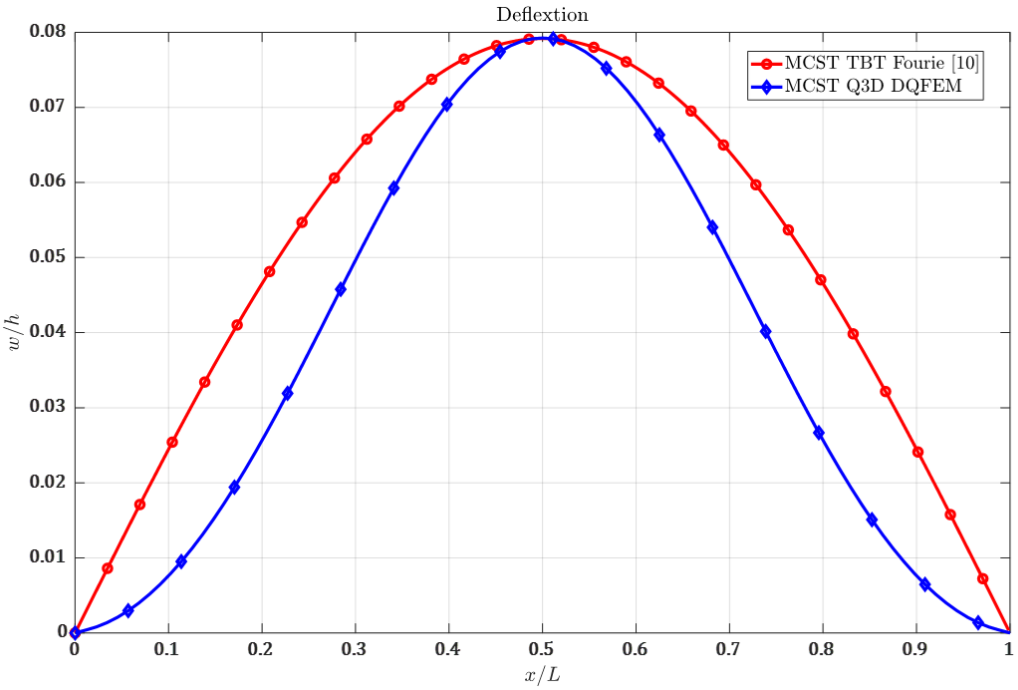


Figure 22: Comparative analysis of the bending of a doubly S-S microbeam exposed to an even distribution of load

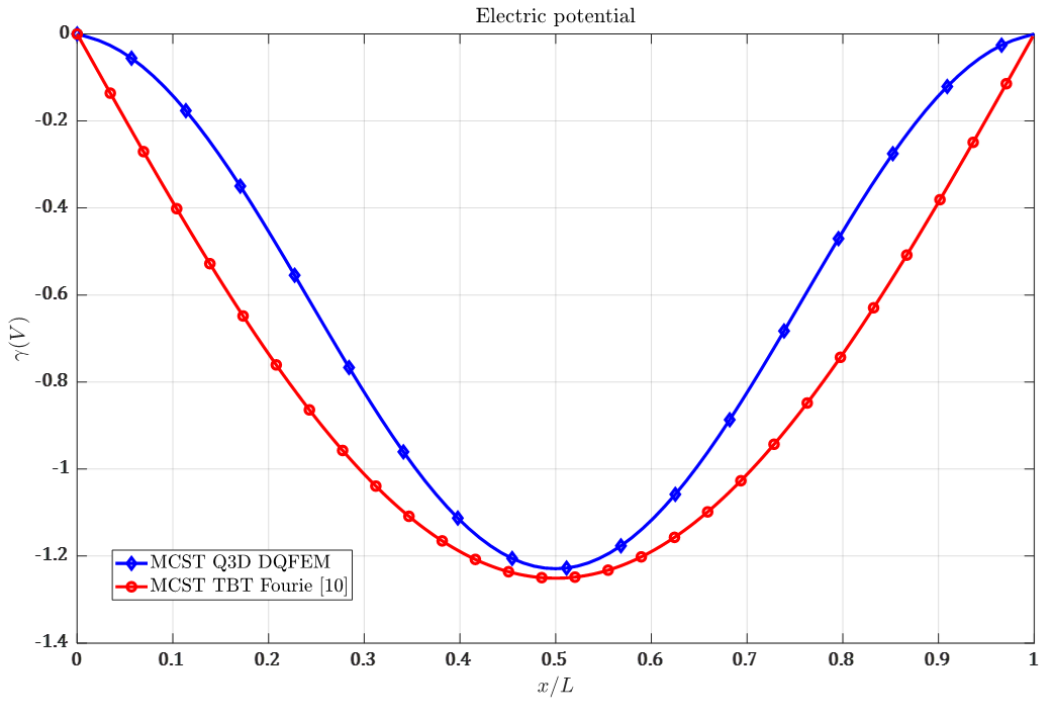


Figure 23: Comparative analysis of electrical potential of a doubly S-S microbeam exposed to an even distribution of load

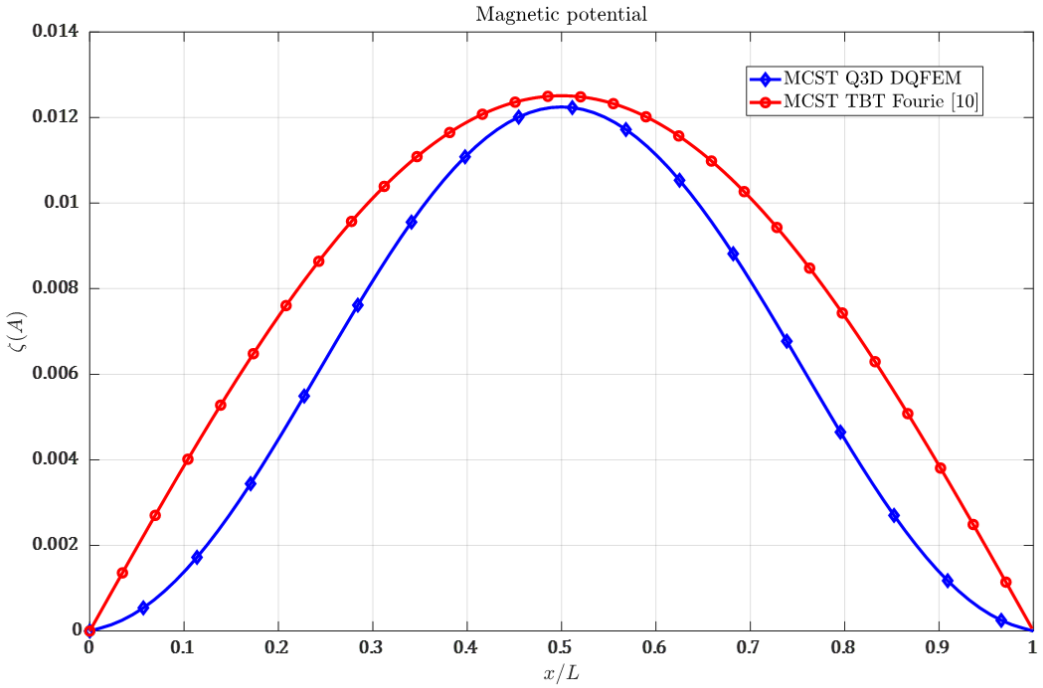


Figure 24: Comparative analysis of magnetic potential of a doubly S-S microbeam exposed to an even distribution of load

To validate our numerical method, we computed the semi-analytical model presented

Table 8: Comparison of numerical results ($b = 2h$, $L = 20h$), $50\% - 50\%$ $BaTiO_3$–$CoFe_2O_4$

$h(\mu m)$	Frequency (MHz)					
	1st mode		2nd mode		3rd mode	
	[10]	Present	[10]	Present	[10]	Present
14.42	4.097	4.069	16.811	16.228	39.647	34.853
28.84	1.710	1.701	7.007	6.784	16.466	14.796
$h(\mu m)$	w/h		$\gamma(V)$		$\zeta(A)$	
	[10]	Present	[10]	Present	[10]	Present
14.42	0.0792	0.0793	-1.251	-1.229	0.0125	0.0122
28.84	0.0284	0.0283	-0.896	-0.877	0.0090	0.0087

in reference [10] and compared it with our method. As shown in Figures 22-24, the results of our current model closely align in midspan with the semi-analytical results from [10]. Our model give the exact shape of the bending , electrical potential and magnetic potential, on the other hand the literature semi analytical model give only the sinusoidal midspan value shape. This comparison supports the validity of the existing model and demonstrates that the DQFEM, in conjunction with the refined high-order beam theory, provides more accurate results at all locations, in contrast to analytical methods, which only provide data at the midline. Table 8 presents a comparison of the first, second and third frequencies, as well as the midspan deflection, electric potential, and magnetic potential. The results in Table 8 further confirm the effectiveness and validity of our model.

3 Parametric Analysis of the Sandwich MEE-FGM Microbeam

In this section, for the upper and bottom outer surfaces layers an FG mixture of $(BaTiO_3 - CoFe_2O_4)$ and epoxy is used, from which this mixture is controlled by the power law of FG materials in equations 62 and 63. The inner core is an isotropic material and it is composed of epoxy. The physical characteristics of these materials are listed in Table 4.

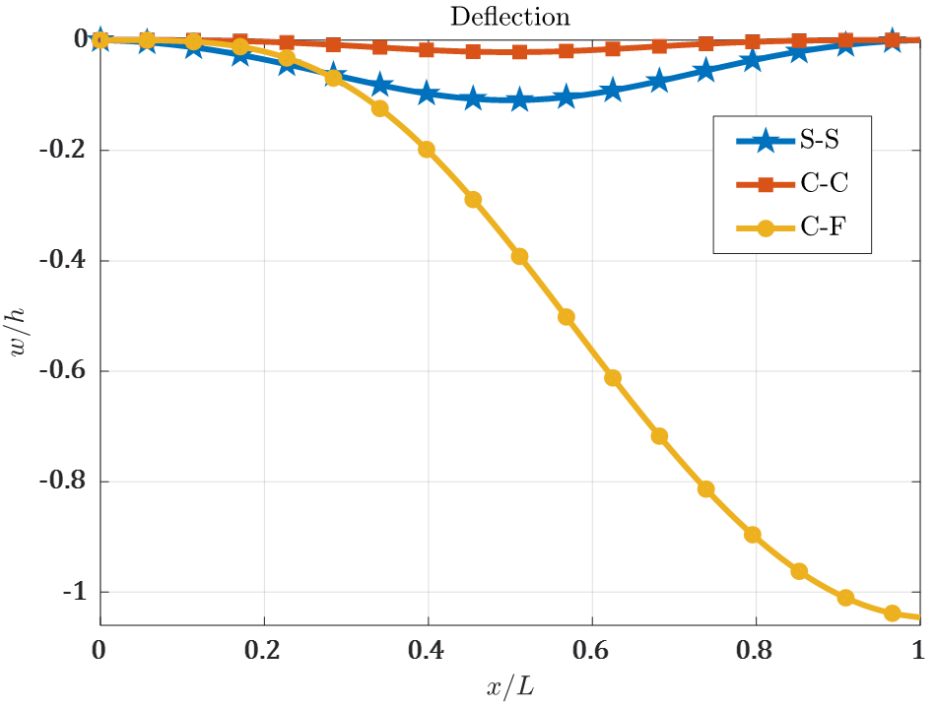


Figure 25: Deflection of MEE sandwich microbeam with various boundary conditions,$k = 1, h = 20\mu m, b = 2h, L = 20h, (1-1-1), BaTiO_3(50\%) - CoFe_2O_4(50\%)$

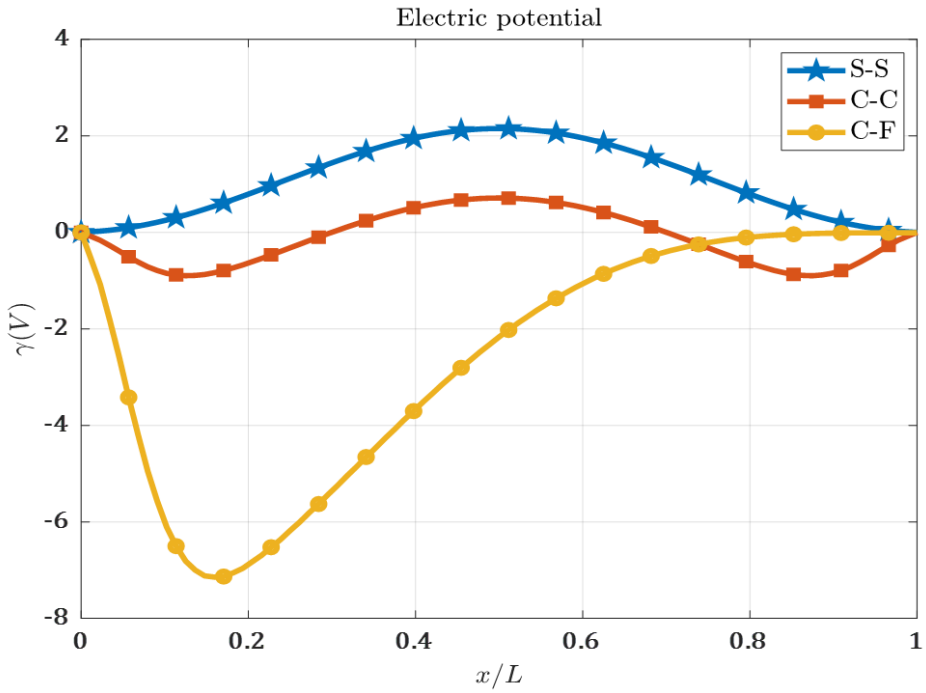


Figure 26: Electric potential of MEE sandwich microbeam with various boundary conditions,$k = 1, h = 20\mu m, b = 2h, L = 20h, (1-1-1), BaTiO_3(50\%) - CoFe_2O_4(50\%)$

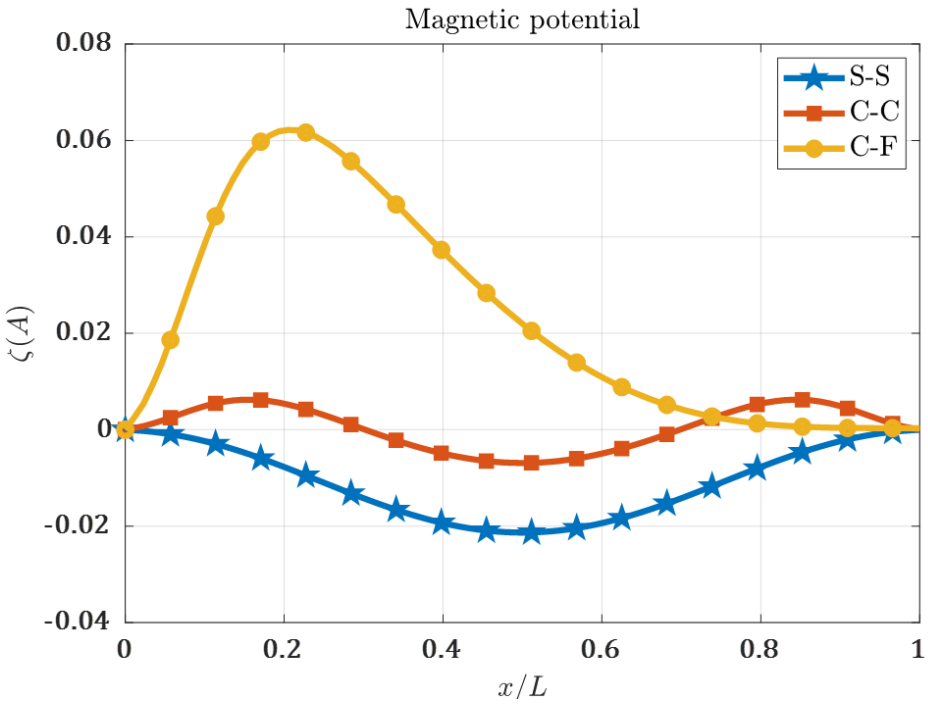


Figure 27: Magnetic potential of MEE sandwich microbeam with various boundary conditions,$k = 1, h = 20\mu m, b = 2h, L = 20h, (1-1-1), BaTiO_3(50\%) - CoFe_2O_4(50\%)$

Figure 25 shows the bending response of a MEE sandwich microbeam with three deferent boundary conditions as simply supported, clamped, and clamped free. As noticed the simply supported example give high deflection then the clamped example, and the clamped free give more important deflection. Then nature of the bending response gives deferent electric and magnetic potential distribution along the length of the beam as showed in figures 26 and 27 respectively. As represented in figure 26, electrical potential has positive value in all the points of the microbeam in simply supported case, unlike the clamped free, the electric potential has negative value across all the microbeam. In the clamped example it is noticed that the electric potential has negative value near the boundary ends of the microbeam, but in the middle the value is positive. All that is explained that the uniform load cause mechanical deformation who generate electrical potential across the microbeam. In regions of the microbeam where the material is compressed, the piezoelectric effect generates a positive electric charge (V) and the piezomagnetic effect generates a negative magnetic charge (A), and it is the opposites where the material is stretched, a negative electric and a positive magnetic charge are generated. Tables 9-11 represent the deflection, electric potential, and magnetic potential for a microbeam with simply supported boundary conditions

with various layers thickness ratio and MEE core material mixture percentage and also various FG gradations index for the upper and bottom layers. It is noticed that with the increaser of the inner core thickness the deflection decreases, in parallel the electric and magnetic potentials decrease. by increasing the surface layers thickness the deflection, electric and magnetic potentials increase. This is due to the increased proportion of epoxy materials which are more flexible compared to $BaTiO_3-CoFe_2O_4$. The electric potential and the magnetic potential are proportional to the percentage of $BaTiO_3 - CoFe_2O_4$ mixture.

Table 9: S–S sandwich microbeam midspan deflection with various layers thickness ratio and MEE core material mixture percentage $BaTiO_3$–$CoFe_2O_4$ ($h = 20\,\mu m,\ b = 2h,\ L = 20h$).

$BaTiO_3$–$CoFe_2O_4$	k	1-1-1	1-2-1	2-1-2	1-0-1	2-2-1	2-1-1
20%-80%	0	-0.0447	-0.0447	-0.0447	-0.0447	-0.0447	-0.0447
	0.5	-0.0716	-0.0646	-0.0770	-0.0849	-0.0688	-0.0750
	1	-0.0968	-0.0809	-0.1105	-0.1326	-0.0902	-0.1053
	10	-0.2523	-0.1574	-0.3693	-0.6712	-0.2086	-0.3201
40%-60%	0	-0.0488	-0.0488	-0.0488	-0.0488	-0.0488	-0.0488
	0.5	-0.0778	-0.0703	-0.0837	-0.0922	-0.0748	-0.0815
	1	-0.1048	-0.0878	-0.1196	-0.1432	-0.0978	-0.1140
	10	-0.2681	-0.1691	-0.3879	-0.6878	-0.2228	-0.3378
50%-50%	0	-0.0511	-0.0511	-0.0511	-0.0511	-0.0511	-0.0511
	0.5	-0.0814	-0.0736	-0.0875	-0.0963	-0.0783	-0.0852
	1	-0.1094	-0.0917	-0.1246	-0.1491	-0.1021	-0.1188
	10	-0.2766	-0.1756	-0.3978	-0.6963	-0.2305	-0.3473
60%-40%	0	-0.0537	-0.0537	-0.0537	-0.0537	-0.0537	-0.0537
	0.5	-0.0852	-0.0771	-0.0916	-0.1008	-0.0820	-0.0892
	1	-0.1143	-0.0960	-0.1301	-0.1554	-0.1068	-0.1241
	10	-0.2857	-0.1825	-0.4080	-0.7049	-0.2387	-0.3572
80%-20%	0	-0.0597	-0.0597	-0.0597	-0.0597	-0.0597	-0.0597
	0.5	-0.0941	-0.0853	-0.1011	-0.1111	-0.0906	-0.0985
	1	-0.1256	-0.1058	-0.1426	-0.1698	-0.1174	-0.1361
	10	-0.3054	-0.1980	-0.4298	-0.7224	-0.2568	-0.3784

Table 10: S–S sandwich microbeam midspan electric potential with various layer thickness ratios and MEE core material mixture percentage $BaTiO_3$–$CoFe_2O_4$ ($h = 20\,\mu m,\ b = 2h,\ L = 20h$).

$BaTiO_3$–$CoFe_2O_4$	k	1-1-1	1-2-1	2-1-2	1-0-1	2-2-1	2-1-1
20%-80%	0	0.9449	0.9449	0.9449	0.9449	0.9449	0.9449
	0.5	1.4394	1.3045	1.5476	1.7064	1.3851	1.5071
	1	1.8800	1.5836	2.1428	2.5699	1.7567	2.0419
	10	4.3303	2.8067	6.1661	10.7477	3.6328	5.4012
40%-60%	0	1.0476	1.0476	1.0476	1.0476	1.0476	1.0476
	0.5	1.5895	1.4419	1.7080	1.8816	1.5301	1.6637
	1	2.0687	1.7461	2.3541	2.8171	1.9346	2.2446
	10	4.6731	3.0621	6.5780	11.1912	3.9393	5.7887
50%-50%	0	1.1005	1.1005	1.1005	1.1005	1.1005	1.1005
	0.5	1.6659	1.5120	1.7894	1.9704	1.6040	1.7432
	1	2.1637	1.8284	2.4599	2.9401	2.0244	2.3463
	10	4.8342	3.1870	6.7624	11.3599	4.0860	5.9658
60%-40%	0	1.1574	1.1574	1.1574	1.1574	1.1574	1.1574
	0.5	1.7474	1.5869	1.8762	2.0650	1.6829	1.8281
	1	2.2644	1.9160	2.5719	3.0697	2.1197	2.4540
	10	4.9991	3.3175	6.9469	11.5183	4.2375	6.1446
80%-20%	0	1.2876	1.2876	1.2876	1.2876	1.2876	1.2876
	0.5	1.9321	1.7570	2.0725	2.2784	1.8617	2.0200
	1	2.4903	2.1136	2.8221	3.3579	2.3340	2.6950
	10	5.3506	3.6036	7.3283	11.8226	4.5645	6.5190

Table 11: S–S sandwich microbeam midspan magnetic potential with various layer thickness ratios and MEE core material mixture percentage $BaTiO_3$–$CoFe_2O_4$ ($h = 20\,\mu m,\ b = 2h,\ L = 20h$).

$BaTiO_3$–$CoFe_2O_4$	k	1-1-1	1-2-1	2-1-2	1-0-1	2-2-1	2-1-1
20%-80%	0	-0.0100	-0.0100	-0.0100	-0.0100	-0.0100	-0.0100
	0.5	-0.0152	-0.0138	-0.0163	-0.0180	-0.0146	-0.0159
	1	-0.0198	-0.0167	-0.0225	-0.0270	-0.0185	-0.0215
	10	-0.0443	-0.0293	-0.0607	-0.0956	-0.0375	-0.0541
40%-60%	0	-0.0107	-0.0107	-0.0107	-0.0107	-0.0107	-0.0107
	0.5	-0.0161	-0.0146	-0.0173	-0.0191	-0.0155	-0.0169
	1	-0.0209	-0.0177	-0.0238	-0.0285	-0.0196	-0.0227
	10	-0.0460	-0.0307	-0.0624	-0.0961	-0.0391	-0.0558
50%-50%	0	-0.0110	-0.0110	-0.0110	-0.0110	-0.0110	-0.0110
	0.5	-0.0165	-0.0150	-0.0178	-0.0196	-0.0159	-0.0173
	1	-0.0214	-0.0181	-0.0243	-0.0291	-0.0201	-0.0232
	10	-0.0465	-0.0313	-0.0628	-0.0957	-0.0397	-0.0564
60%-40%	0	-0.0112	-0.0112	-0.0112	-0.0112	-0.0112	-0.0112
	0.5	-0.0168	-0.0153	-0.0181	-0.0199	-0.0162	-0.0176
	1	-0.0218	-0.0184	-0.0247	-0.0295	-0.0204	-0.0236
	10	-0.0468	-0.0316	-0.0628	-0.0947	-0.0400	-0.0564
80%-20%	0	-0.0109	-0.0109	-0.0109	-0.0109	-0.0109	-0.0109
	0.5	-0.0163	-0.0148	-0.0174	-0.0192	-0.0157	-0.0170
	1	-0.0209	-0.0178	-0.0237	-0.0282	-0.0196	-0.0226
	10	-0.0439	-0.0300	-0.0584	-0.0868	-0.0378	-0.0527

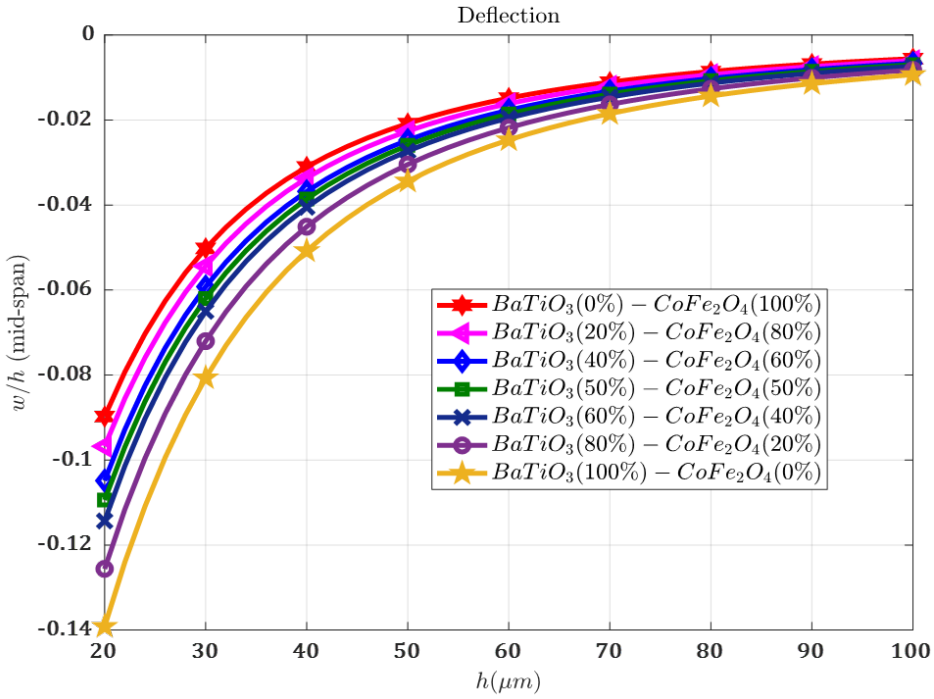


Figure 28: Simply supported sandwich microbeam midspan deflection with various thickness and MEE core material mixture percentage $BaTiO_3 - CoFe_2O_4$ ($k_z = 1, \quad b = 2h, \quad L = 20h, \quad (1 - 1 - 1)$)

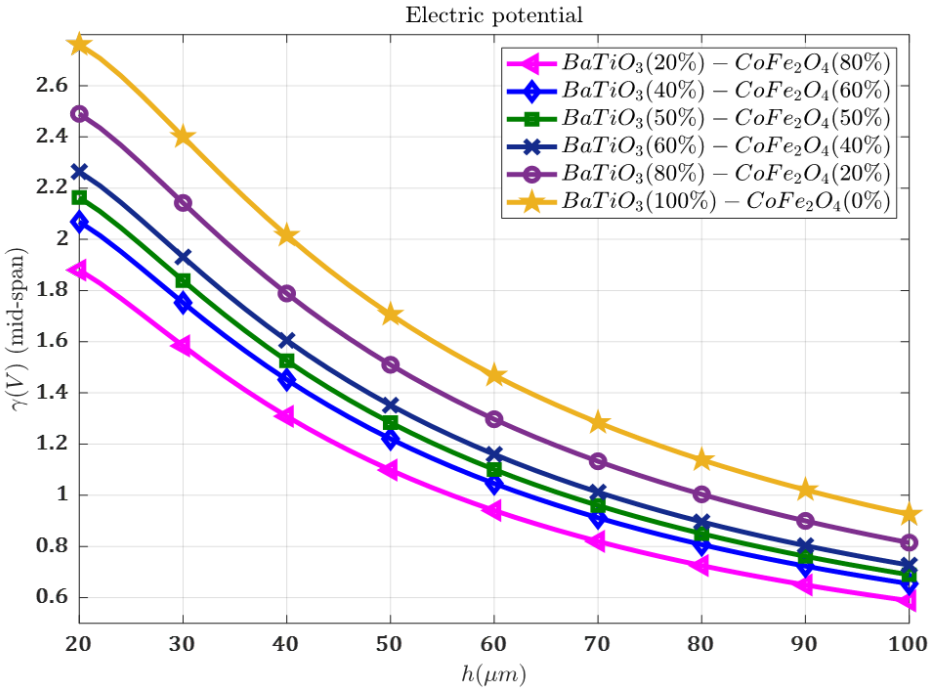


Figure 29: Simply supported sandwich microbeam midspan Electric potential with various thickness and MEE core material mixture percentage $BaTiO_3 - CoFe_2O_4$ ($k_z = 1, \quad b = 2h, \quad L = 20h, \quad (1 - 1 - 1)$)

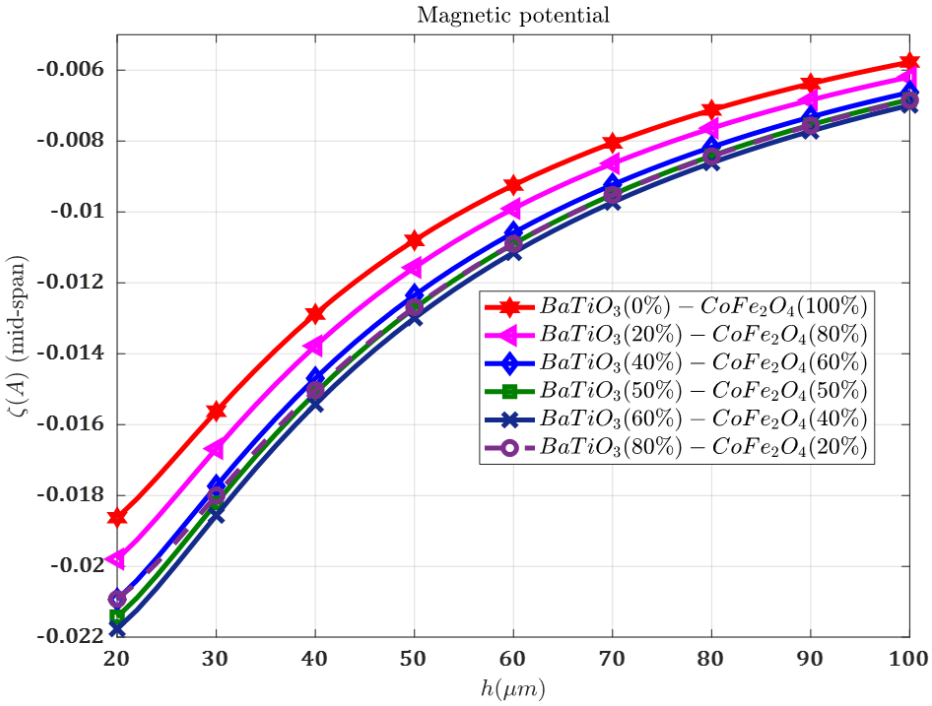


Figure 30: Simply supported sandwich microbeam midspan Magnetic potential with various thickness and MEE core material mixture percentage $BaTiO_3 - CoFe_2O_4$ ($k_z = 1, \quad b = 2h, \quad L = 20h, \quad (1-1-1)$)

Figures 28, 29 and 30 illustrates the midspan "deflection, electric potential, and magnetic potential for a doubly S-S microbeam versus the thickness of the beam with various MEE inner material mixture percentage of $BaTiO_3 - CoFe_2O_4$, and a layer's thickness ratio 1-1-1. It is noticed that midspan deflection decrease with the augmentation of the thickness, this is physically reasonable because thicker beams tend to be stiffer and can resist bending or deflection more effectively under the same load. The deflection and the electrical potential increase according to the increase of the $BaTiO_3$ percentage, which means that it generates an electric charge when mechanically deformed. A higher percentage of $BaTiO_3$ would increase the beam's piezoelectric response, causing greater electrical potential, and also the electric potential decrease with higher value of the thickness. However, the magnetic potential magnitude increases when the percentage of $CoFe_2O_4$ increase, but compared to the expansion of the thickness the magnetic potential decrease. As the beam becomes thicker, the mechanical strain induced by bending is distributed over a larger cross-sectional area, leading to a reduced deformation. Since the piezoelectric and piezomagnetic effects depends on the deformation, the electric and magnetic potentials decrease with increasing thickness.

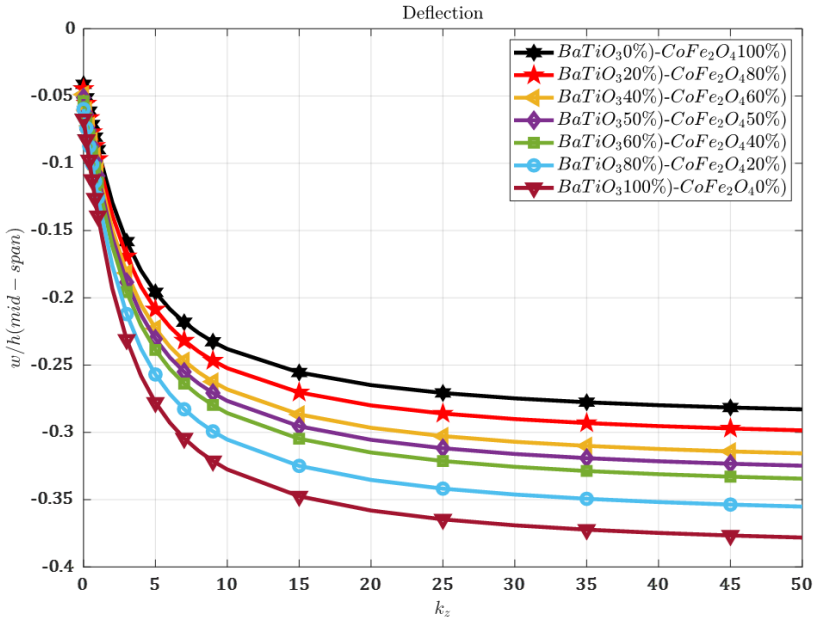


Figure 31: Simply supported sandwich microbeam midspan deflection with various FG fraction index and MEE core material mixture percentage $BaTiO_3 - CoFe_2O_4$ ($h = 20\mu m$, $b = 2h$, $L = 20h$, $(1-1-1)$)

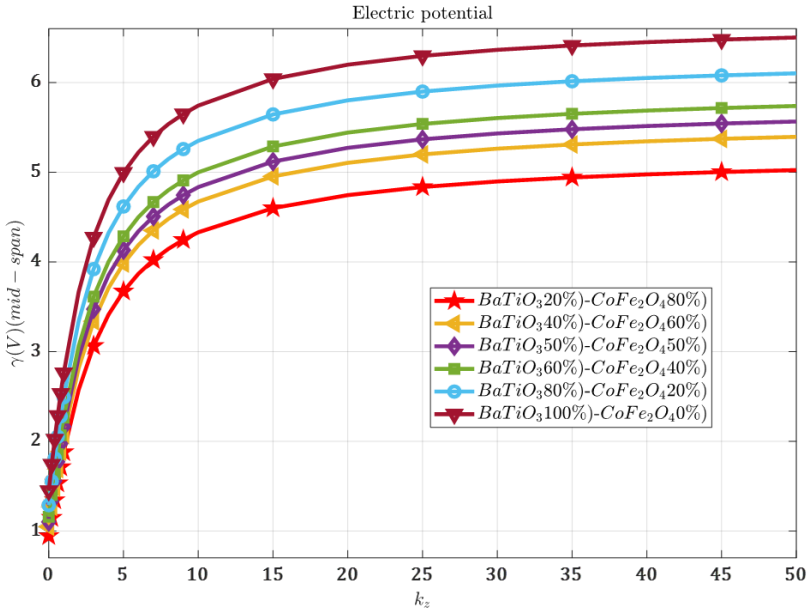


Figure 32: Simply supported sandwich microbeam midspan Electric potential with various FG fraction index and MEE core material mixture percentage $BaTiO_3 - CoFe_2O_4$ ($h = 20\mu m$, $b = 2h$, $L = 20h$, $(1-1-1)$)

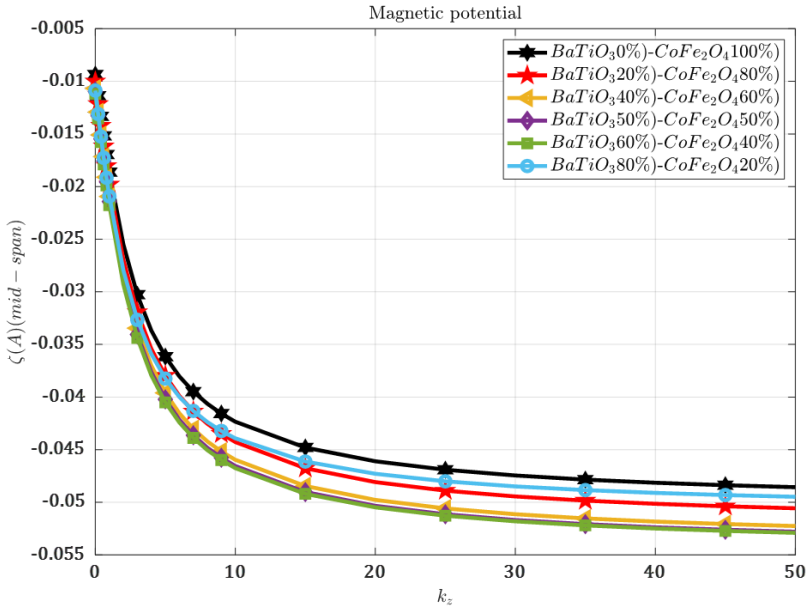


Figure 33: Simply supported sandwich microbeam midspan Magnetic potential with various FG fraction index and MEE core material mixture percentage $BaTiO_3 - CoFe_2O_4$ ($h = 20\mu m$, $b = 2h$, $L = 20h$, $(1-1-1)$)

To demonstrate the influence of the material gradation of the upper and bottom layers, figures 31, 32 and 33 shows the midspan deflection, electric, and magnetic potentials over the variation of the FG material gradation index. As it is known form table 1, the external material (epoxy) is less dense and less rigid than the inner MEE material $BaTiO_3 - CoFe_2O_4$, and according to material distribution formula in equation (1), when the index $k_z = 0$ means that the microbeam's upper and bottom layers is 100% $BaTiO_3 - CoFe_2O_4$ and by increasing the volume fraction index the mixture tends towards the external materials (epoxy). all this explains why the midspan deflection increase in figure 31 as the volume fraction index increase. The increase of the deflection lead to the increase of magnitudes of the electric and magnetic potentials. In figures 32 and 33 it is noticed that the more FG index increases the more we get higher electric and magnetic potentials. It is deduced that high value of FG index is more efficient then when we have a microbeam with 100% $BaTiO_3 - CoFe_2O_4$ mixture. In figures 35 and the magnetic potential has an optimal value between $50\% - 50\%$ and $60\% - 40\%$ of $BaTiO_3 - CoFe_2O_4$ mixture, and this value increase more with the increase of FG index of the upper and bottom layers. The goal in this illustration (figures 34, 35) is to make the mixture $BaTiO_3 - CoFe_2O_4$ more flexible by adding the epoxy material, but keeping the maximum electrical and magnetic efficiency.

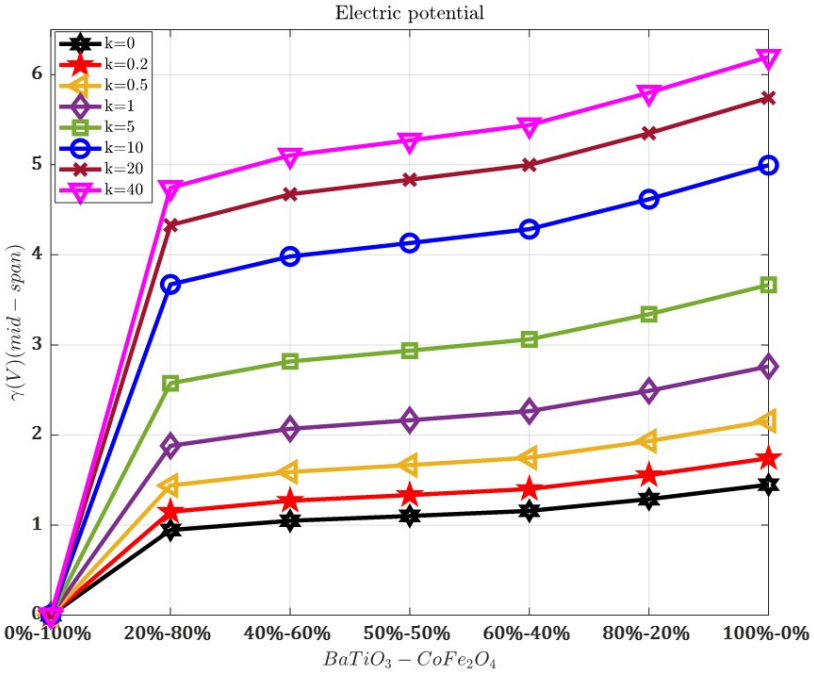


Figure 34: Electric potential at simply supported microbeam midspan with various FG fraction index and MEE inner material mixture percentage $BaTiO_3 - CoFe_2O_4$ ($h = 20\mu m$, $b = 2h$, $L = 20h$, $(1-1-1)$)

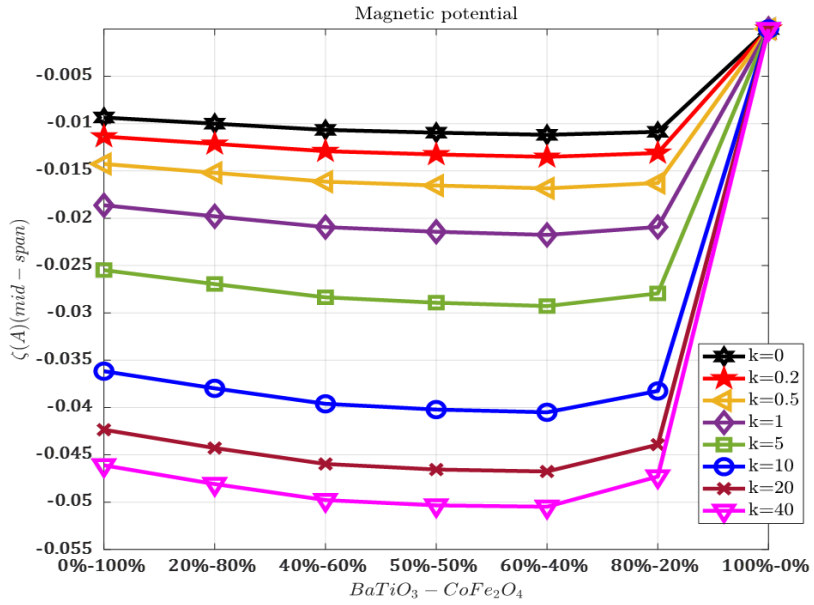


Figure 35: Magnetic potential at simply supported microbeam midspan with various FG fraction index and MEE inner material mixture percentage $BaTiO_3 - CoFe_2O_4$ ($h = 20\mu m$, $b = 2h$, $L = 20h$, $(1-1-1)$)

Table 12: Natural frequency (MHz) of S–S sandwich MEE FG microbeam ($h = 20\,\mu m,\ b = 2h,\ L = 20h$).

$BaTiO_3$–$CoFe_2O_4$	k	1-1-1	1-2-1	2-1-2	1-0-1	2-2-1	2-1-1
0%-100%	0	3.0009	3.0009	3.0009	3.0009	3.0009	3.0009
	0.5	2.6044	2.6727	2.5641	2.5248	2.6293	2.5778
	1	2.3641	2.4816	2.2923	2.2197	2.4074	2.3169
	10	1.7208	1.9782	1.5614	1.3939	1.8166	1.6159
20%-80%	0	2.8546	2.8546	2.8546	2.8546	2.8546	2.8546
	0.5	2.4830	2.5467	2.4455	2.4095	2.5062	2.4582
	1	2.2581	2.3675	2.1916	2.1252	2.2984	2.2143
	10	1.6598	1.8973	1.5156	1.3729	1.7478	1.5646
40%-60%	0	2.7068	2.7068	2.7068	2.7068	2.7068	2.7068
	0.5	2.3605	2.4195	2.3259	2.2931	2.3819	2.3376
	1	2.1513	2.2526	2.0902	2.0301	2.1885	2.1110
	10	1.5992	1.8163	1.4703	1.3523	1.6792	1.5136
50%-50%	0	2.6321	2.6321	2.6321	2.6321	2.6321	2.6321
	0.5	2.2987	2.3554	2.2656	2.2344	2.3192	2.2768
	1	2.0975	2.1947	2.0391	1.9822	2.1332	2.0590
	10	1.5689	1.7757	1.4478	1.3421	1.6449	1.4882
60%-40%	0	2.5568	2.5568	2.5568	2.5568	2.5568	2.5568
	0.5	2.2364	2.2907	2.2048	2.1752	2.2561	2.2155
	1	2.0434	2.1364	1.9877	1.9341	2.0775	2.0067
	10	1.5387	1.7350	1.4254	1.3320	1.6106	1.4629
80%-20%	0	2.4040	2.4040	2.4040	2.4040	2.4040	2.4040
	0.5	2.1103	2.1598	2.0817	2.0555	2.1282	2.0913
	1	1.9340	2.0185	1.8840	1.8368	1.9649	1.9009
	10	1.4783	1.6532	1.3809	1.3120	1.5418	1.4126
100%-0%	0	2.2473	2.2473	2.2473	2.2473	2.2473	2.2473
	0.5	1.9814	2.0258	1.9560	1.9331	1.9974	1.9645
	1	1.8226	1.8981	1.7783	1.7378	1.8501	1.7933
	10	1.4179	1.5706	1.3367	1.2923	1.4728	1.3624

Table 13: Natural frequency (MHz) of S–S sandwich MEE FG microbeam ($h = 20\,\mu m,\ b = 2h,\ L = 5h$).

$BaTiO_3$–$CoFe_2O_4$	k	1-1-1	1-2-1	2-1-2	1-0-1	2-2-1	2-1-1
0%-100%	0	47.2916	47.2916	47.2916	47.2916	47.2916	47.2916
	0.5	41.1713	42.2333	40.5404	39.9204	41.5587	40.7551
	1	37.4306	39.2669	36.3010	35.1478	38.1089	36.6893
	10	25.0912	28.8436	24.0779	22.0434	26.2430	24.2694
20%-80%	0	44.9860	44.9860	44.9860	44.9860	44.9860	44.9860
	0.5	39.2521	40.2426	38.6666	38.0975	39.6129	38.8654
	1	35.7532	37.4636	34.7073	33.6535	36.3840	35.0659
	10	24.6506	28.1325	23.7786	21.7129	25.7067	23.9241
40%-60%	0	42.6567	42.6567	42.6567	42.6567	42.6567	42.6567
	0.5	37.3158	38.2338	36.7762	36.2581	37.6497	36.9591
	1	34.0637	35.6463	33.1026	32.1487	34.6463	33.4313
	10	24.2175	27.4286	23.3300	21.3876	25.1785	23.5847
50%-50%	0	41.4802	41.4802	41.4802	41.4802	41.4802	41.4802
	0.5	36.3391	37.2203	35.8227	35.3302	36.6594	35.9975
	1	33.2127	34.7303	32.2946	31.3910	33.7708	32.6081
	10	24.0035	27.0790	22.9739	21.2270	24.9173	23.4170
60%-40%	0	40.2938	40.2938	40.2938	40.2938	40.2938	40.2938
	0.5	35.3554	36.1994	34.8624	34.3956	35.6618	35.0290
	1	32.3566	33.8084	31.4819	30.6289	32.8898	31.7800
	10	23.7913	26.7307	22.6194	21.0676	24.6579	23.2221
80%-20%	0	37.8850	37.8850	37.8850	37.8850	37.8850	37.8850
	0.5	33.3619	34.1298	32.9168	32.5021	33.6402	33.0668
	1	30.6252	31.9422	29.8391	29.0888	31.1077	30.1060
	10	23.3713	26.0374	21.9145	20.7527	24.1437	22.4243
100%-0%	0	35.4154	35.4154	35.4154	35.4154	35.4154	35.4154
	0.5	31.3249	32.0137	30.9291	30.5678	31.5739	31.0619
	1	28.8614	30.0383	28.1671	27.5224	29.2913	28.4017
	10	22.5156	24.9286	21.2149	20.4430	23.3858	21.6301

The natural frequency of a simply supported MEE FG microbeam composed of two materials ($BaTiO_3 - CoFe_2O_4$ and *epoxy*). As it is noticed in tables 12-13 there is a decrease in the value of natural frequency with respect to the increase in length-thickness ratio. Also, the natural frequency decrease with the rise of the FG gradation index. The value of natural frequency is higher when the MEE mixture is

composed of 100% $CoFe_2O_4$ and it begins to decrease by increasing the percentage of $BaTiO_3$.

4 Parametric Analysis of the Bilaterally Coated MEE-FGM Microbeam

In this section, the microbeam model is composed of an FG mixture of ($BaTiO_3 - CoFe_2O_4$) and epoxy, from which this mixture is controlled by the power law of FG materials in equation 67. The inner core is an isotropic material and it is composed of epoxy. The physical characteristics of these materials are listed in Table 4.

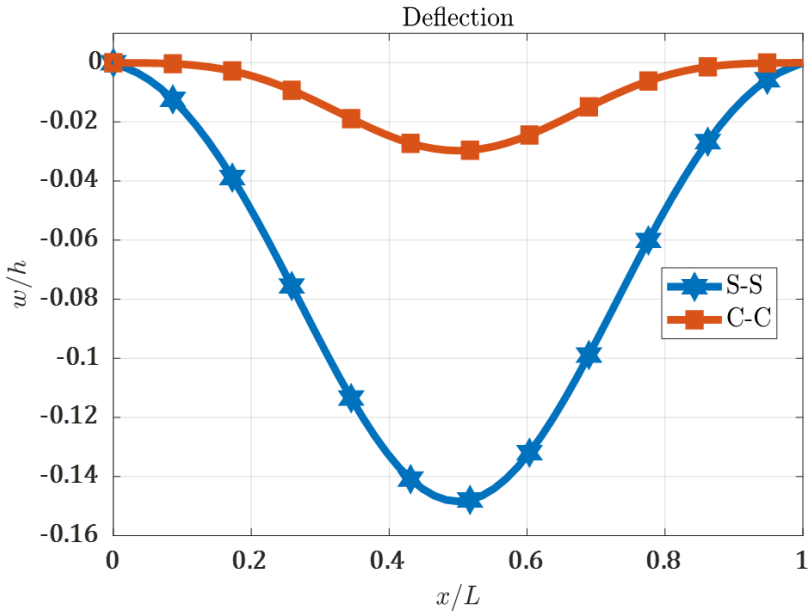


Figure 36: Deflection of MEE bilaterally microbeam with various boundary conditions ($k_z = 1$, $h = 20\mu m$, $b = 2h$, $L = 20h$, $BaTiO_3$ (50%)-$CoFe_2O_4$(50%)

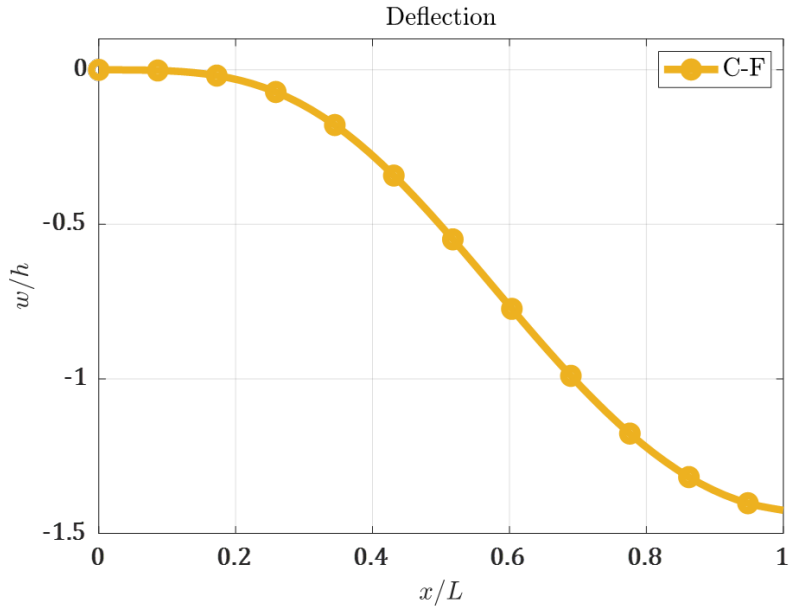


Figure 37: Deflection of MEE bilaterally microbeam with CF boundary conditions ($k_z = 1$, $h = 20\mu m$, $b = 2h$, $L = 20h$, $BaTiO_3$ (50%)-$CoFe_2O_4$(50%)

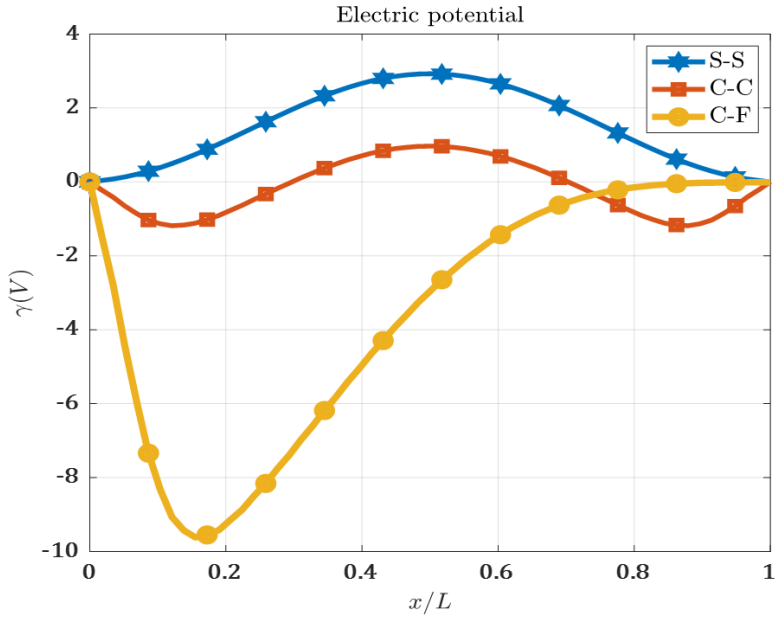


Figure 38: Electric potential of MEE bilaterally microbeam with various boundary conditions ($k_z = 1$, $h = 20\mu m$, $b = 2h$, $L = 20h$, $BaTiO_3$ (50%)-$CoFe_2O_4$(50%)

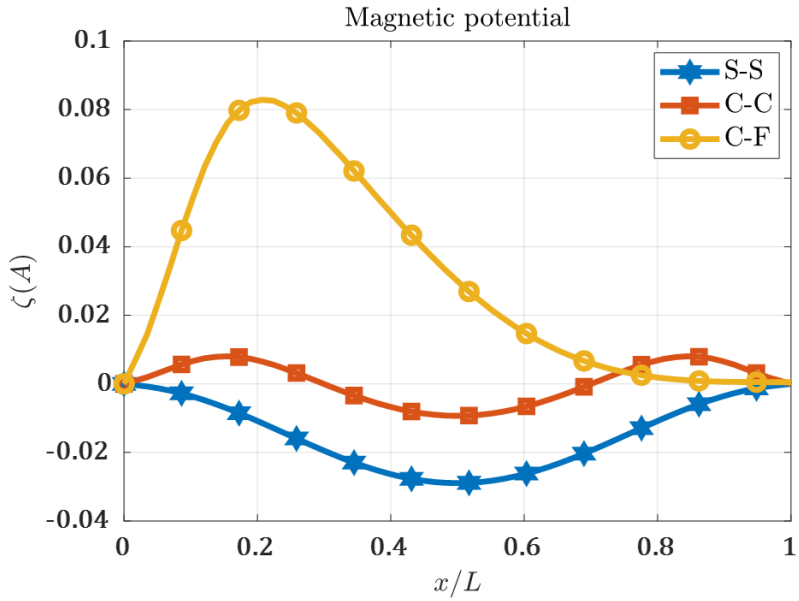


Figure 39: Magnetic potential of MEE bilaterally microbeam with CF boundary conditions ($k_z = 1$, $h = 20\mu m$, $b = 2h$, $L = 20h$, $BaTiO_3$ (50%)-$CoFe_2O_4$(50%)

In Figures 36-37, we demonstrated the bending response of the magneto-electro-elastic (MEE) bilaterally supported microbeam under different boundary conditions (simply supported, clamped, and clamped-free). The observed variations in deflection arise due to differences in constraint stiffness. The simply supported beam experiences the highest deflection as it lacks rotational constraints at the ends, whereas the clamped beam exhibits reduced deflection due to restricted end rotations. The clamped-free (cantilever) configuration shows the highest deflection at the free end due to the absence of support at one end. This deflection pattern influences the distribution of electric and magnetic potentials along the beam length, as illustrated in Figures 38 and 39. The electromechanical coupling in the system arises due to the piezoelectric and piezomagnetic effects. When the beam undergoes bending, the induced strain leads to charge polarization. The regions experiencing compression generate a positive electric charge (due to the direct piezoelectric effect) and a negative magnetic charge (due to the piezomagnetic effect), whereas the tensioned regions exhibit the opposite effect. This explains why, in the simply supported case, the electric potential (V) is uniformly positive (Figures 38), while in the clamped-free case, it is uniformly negative. The clamped configuration results in a more complex charge distribution due to localized constraint effects at the boundaries.

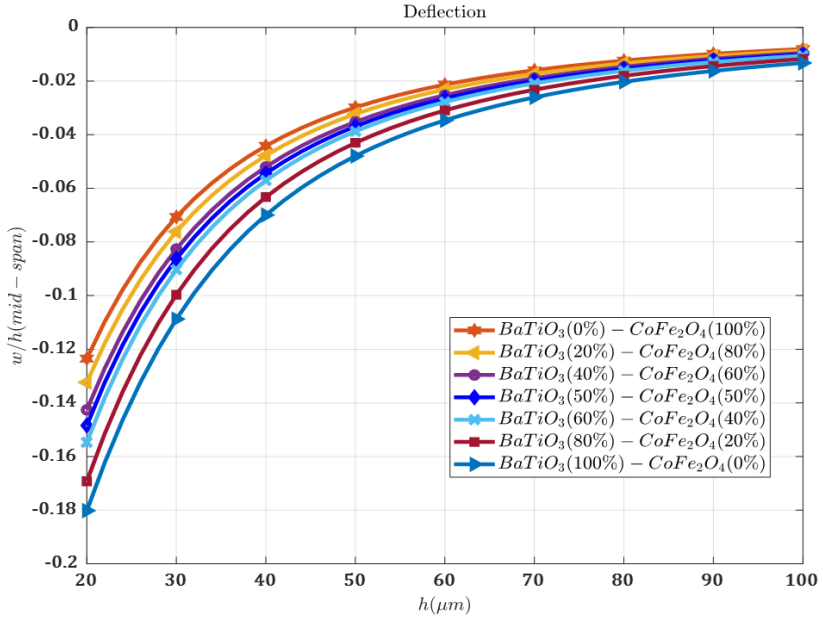


Figure 40: Simply supported microbeam midspan deflection with various thickness and MEE inner material mixture percentage $BaTiO_3 - CoFe_2O_4$ $(k_z = 1, \quad b = 2h, \quad L = 20h,)$

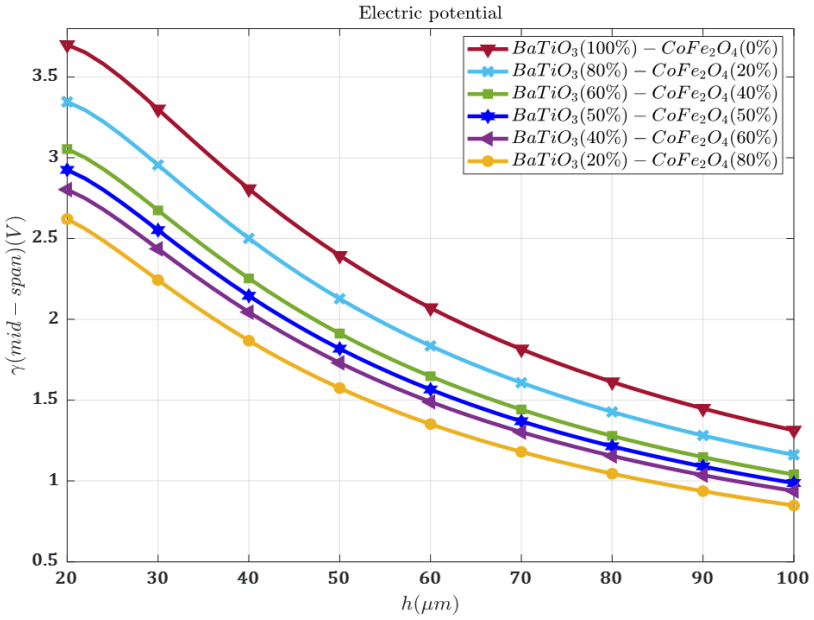


Figure 41: Electric potential at simply supported microbeam midspan with various thickness and MEE inner material mixture percentage $BaTiO_3 - CoFe_2O_4$ $(k_z = 1, \quad b = 2h, \quad L = 20h,)$

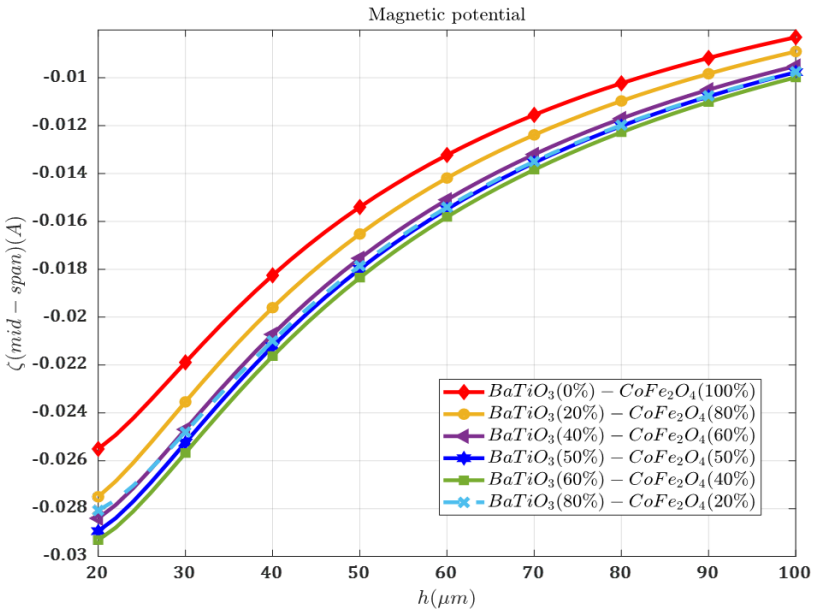


Figure 42: Magnetic potential at simply supported microbeam midspan with various thickness and MEE inner material mixture percentage $BaTiO_3 - CoFe_2O_4$ ($k_z = 1, \quad b = 2h, \quad L = 20h,$)

Figures 40, 41 and 42 illustrate the midspan deflection, electric potential, and magnetic potential as functions of beam thickness and inner material composition. The inverse relationship between thickness and deflection is expected, as thicker beams possess higher flexural rigidity, making them more resistant to deformation under the same applied load. Regarding electromechanical behavior, increasing the proportion of $BaTiO_3$ enhances the piezoelectric response, leading to higher electric potential generation. This occurs because $BaTiO_3$ is a piezoelectric ceramic with a high electromechanical coupling coefficient, meaning it efficiently converts mechanical deformation into electrical energy. Conversely, $CoFe_2O_4$ exhibits strong piezomagnetic properties, leading to higher magnetic potential generation. However, as the beam thickness increases, both electric and magnetic potentials decrease because strain distribution becomes more uniform, reducing localized stress concentrations that drive charge generation. This behavior aligns with the fundamental principles of piezoelectric and piezomagnetic materials, where mechanical strain directly affects charge separation and potential generation.

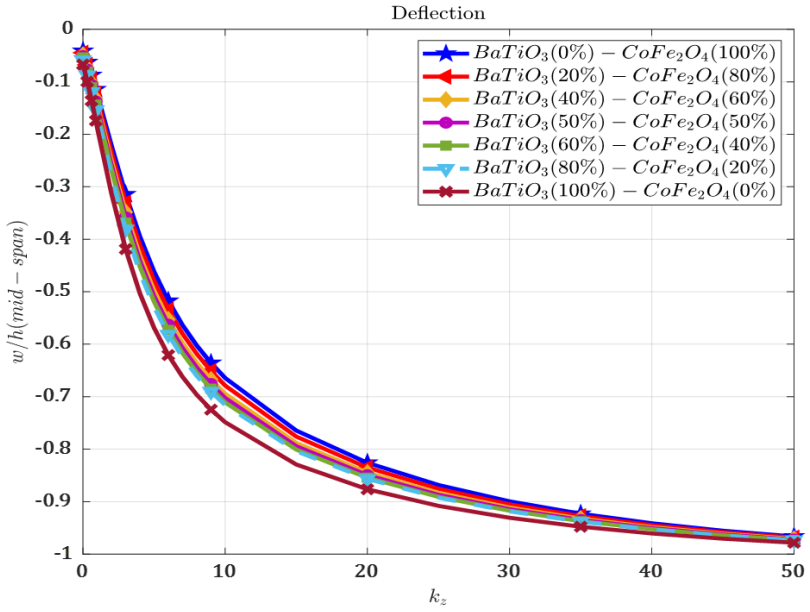


Figure 43: Simply supported microbeam midspan deflection with various FG fraction index and MEE inner material mixture percentage $BaTiO_3 - CoFe_2O_4$ $(h = 20\mu m, \quad b = 2h, \quad L = 20h,)$

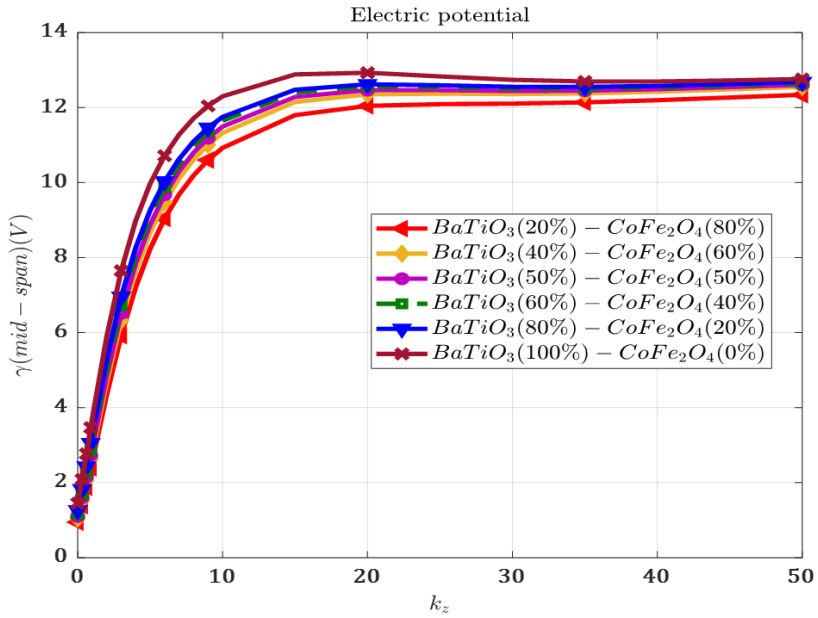


Figure 44: Electric potential at simply supported microbeam midspan with various FG fraction index and MEE inner material mixture percentage $BaTiO_3 - CoFe_2O_4$ $(h = 20\mu m, \quad b = 2h, \quad L = 20h,)$

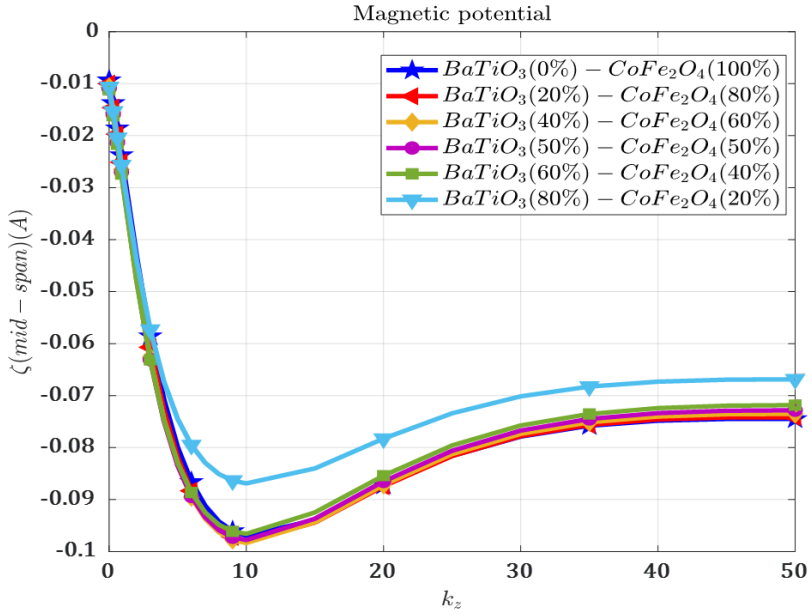


Figure 45: Magnetic potential at simply supported microbeam midspan with various FG fraction index and MEE inner material mixture percentage $BaTiO_3 - CoFe_2O_4$ ($h = 20\mu m, \quad b = 2h, \quad L = 20h,$)

Figures 43, 44 and 45 depict the influence of the functionally graded (FG) material gradation index on the midspan deflection and electromechanical potentials. As the gradation index k_z increases, the beam composition transitions from a fully magneto-electro-elastic core ($BaTiO_3 - CoFe_2O_4$) to an outer epoxy-rich composition. Given that epoxy is significantly more flexible and less dense than the ceramic phases, the beam exhibits increased deflection due to reduced overall stiffness. The electrical and magnetic potentials initially increase with the FG index, peaking at a critical range ($k_z = [6 : 20]$), before stabilizing. This behavior suggests that an optimal material gradation exists where electromechanical efficiency is maximized. The increasing deflection enhances charge generation up to a certain threshold, beyond which further material gradation reduces effective coupling due to the dominance of the epoxy phase. This insight is crucial for optimizing FG microbeam designs to balance mechanical flexibility and electromechanical efficiency.

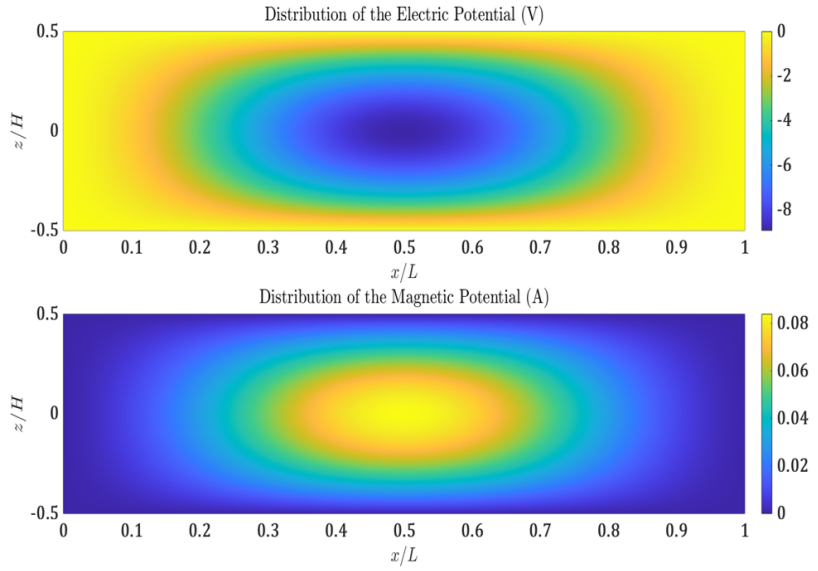


Figure 46: Electric and magnetic potentials distribution of simply supported microbeam with $k_z = 5, \quad h = 20\mu m, \quad b = 2h, \quad L = 20h, \quad BaTiO_3\,(50\%) - CoFe_2O_4\,(50\%)$

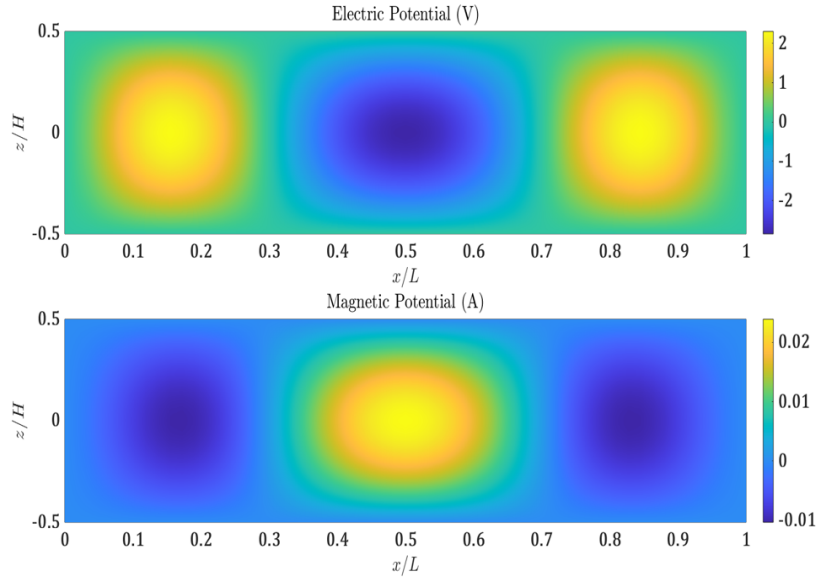


Figure 47: Electric and magnetic potentials distribution of clamped microbeam with $k_z = 5, \quad h = 20\mu m, \quad b = 2h, \quad L = 20h, \quad BaTiO_3\,(50\%) - CoFe_2O_4\,(50\%)$

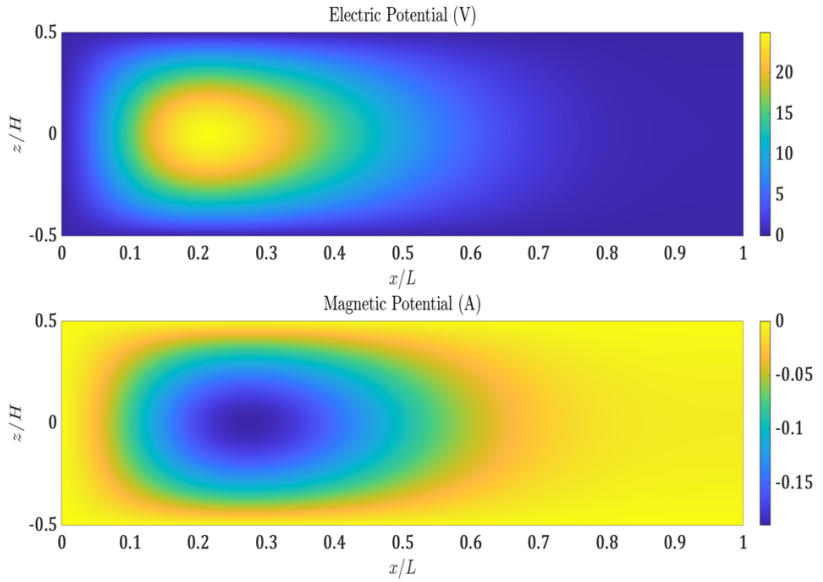


Figure 48: Electric and magnetic potentials distribution of clamped free microbeam with $k_z = 5, \quad h = 20\mu m, \quad b = 2h, \quad L = 20h, \quad BaTiO_3\,(50\%) - CoFe_2O_4\,(50\%)$

Figures 46, 47 and 48 illustrate the distribution of electric and magnetic potentials across the xOz surface of a magneto-electro-elastic microbeam under different boundary conditions: simply supported (Figure 46), clamped (Figure 50), and clamped-free (Figure 48). It is evident that the electric and magnetic potential distributions for the simply supported (Figure 46) and clamped (Figure 47) beams exhibit central symmetry. For the simply supported beam, the maximum values of both electric and magnetic potentials occur at the center. In contrast, for the clamped beam, the highest potentials are found at three locations: near the embedding points and in the center. In the case of the clamped-free beam, the electric and magnetic potentials are primarily concentrated near the embedding location. In conclusion, the high values of electric and magnetic potentials correspond to areas where bending-induced deformations are most significant.

Figure 49-52 presents the variations in deflection, electrical potential, magnetic potential, and natural frequency respectively for different microbeam thicknesses, considering the length-to-thickness ratio in both the current (MCST) and classical models. With $BaTiO_3\,(50\%) - CoFe_2O_4\,(50\%)$. In the numerical analysis, the current model accounts for the couple stress effect, which is incorporated using the Modified Length Scale Parameter (MLSP) $l \neq 0$ (as defined in Equation 44). Conversely, the classical model is derived using the same governing equation but with $l = 0$, meaning

that it does not consider the microstructural effects introduced by MCST. The results indicate that the deflection, electrical potential, and magnetic potential predicted by the current model are consistently lower than those obtained using the classical model across all tested cases. This discrepancy arises due to the inclusion of the couple stress effect in the MCST model, which introduces additional material stiffness at the microscale. As expected, the difference between the two models becomes more pronounced as the microbeam thickness decreases. This behavior is due to the fact that size-dependent effects become more significant at smaller scales, where the influence of microstructural mechanics cannot be neglected. In other words, the classical model, which disregards these effects, tends to overestimate the response of the microbeam in comparison to the MCST-based model. The increasing stiffness introduced by the couple stress theory results in reduced deflection and altered electrical/magnetic responses, as well as higher natural frequencies. Additionally, it is observed that as the length-to-thickness ratio increases, the microbeam becomes more flexible, leading to a greater deflection. This increase in deflection consequently enhances both the electrical and magnetic potentials. On the other hand, the natural frequencies exhibit an inverse relationship with the length-to-thickness ratio, decreasing as the microbeam becomes thinner. This trend is attributed to the reduced stiffness associated with higher length-to-thickness ratios, which lowers the beam's resistance to dynamic vibrations.

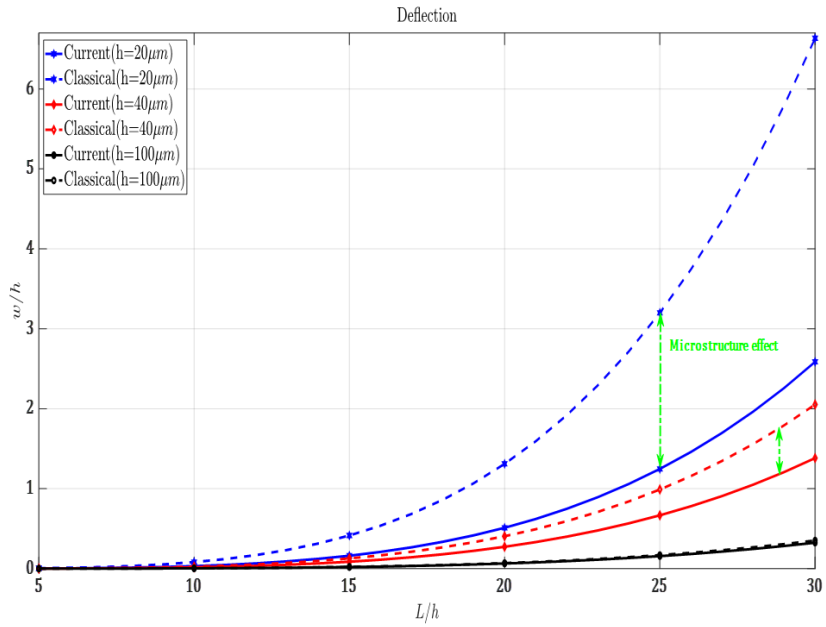


Figure 49: Deflection with respect to length-thickness ratio of simply supported microbeam with $k_z = 5,\ b = 2h$

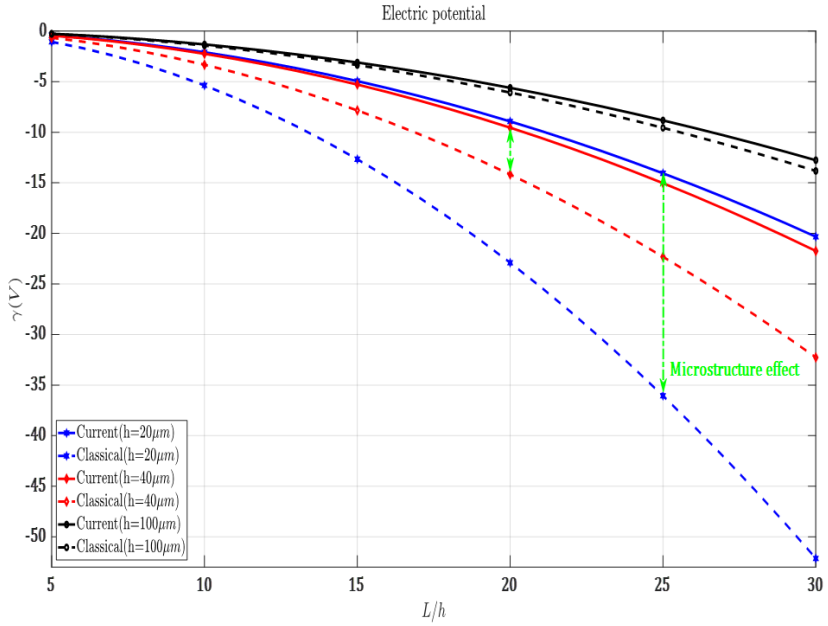


Figure 50: Electric potential with respect to length-thickness ratio of simply supported microbeam with $k_z = 5,\ b = 2h$

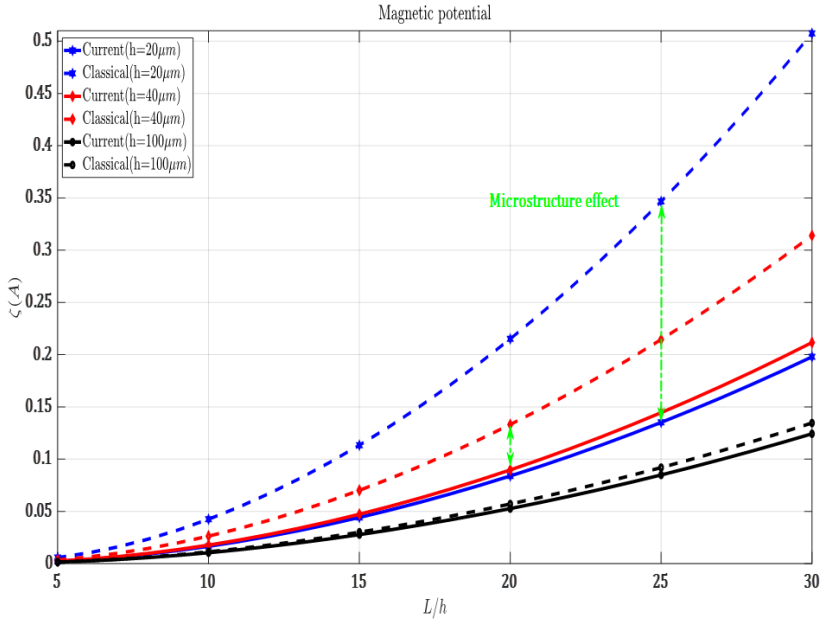


Figure 51: Magnetic potential with respect to length-thickness ratio of simply supported microbeam with $k_z = 5,\ b = 2h$

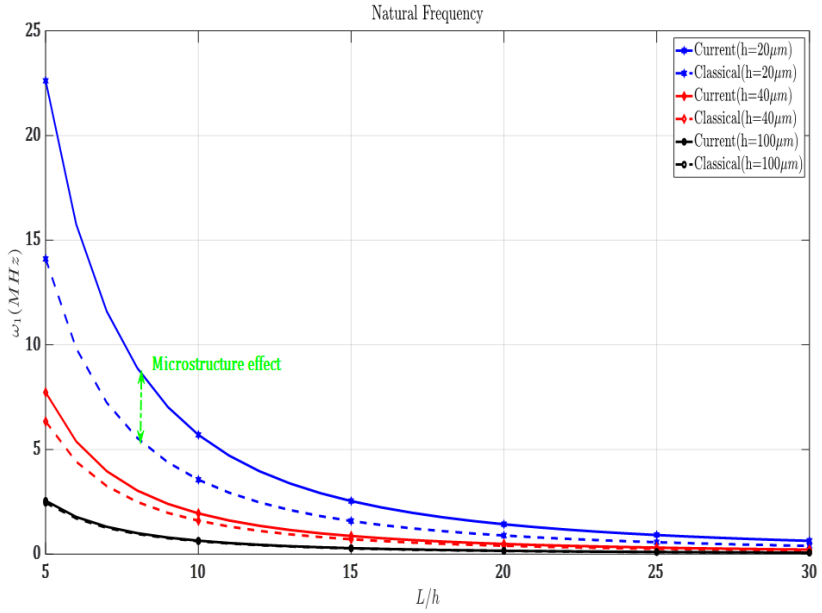


Figure 52: Natural frequencies with respect to length-thickness ratio of simply supported microbeam with $k_z = 5,\ b = 2h$

Table 14 shows the natural frequencies of a simply supported magneto-electro functionally graded microbeam made of $BaTiO_3 - CoFe_2O_4$ and epoxy composite material. Here, natural frequencies are influenced by the thickness $h(\mu m)$ and the power-law compositional gradient index k_z, with different percentages of $BaTiO_3$ and $CoFe_2O_4$. As the thickness $h(\mu m)$ increases from $20\mu m$ to $100\mu m$, the natural frequencies decrease across all material distributions and power-law indices. This is expected as thicker beams generally have lower resonant frequencies due to increased mass and flexibility. The material $BaTiO_3 - CoFe_2O_4$ distribution percentages (ranging from $0\% - 100\%$ to $100\% - 0\%$) also impact the natural frequencies. Generally, as the proportion of $BaTiO_3$ increases, the natural frequency decreases. For instance, at $h = 20\mu m$ and $k_z = 0$, the natural frequency changes from $3.0009MHz$ $(0\% - 100\%)$ to $2.2472MHz$ $(100\% - 0\%)$. This suggests that a higher content of $BaTiO_3$ $(0\% - 100\%)$ corresponds to higher stiffness and thus higher natural frequency, while increasing $CoFe_2O_4$ content $(100\% - 0\%)$ reduces the stiffness, lowering the natural frequency. For each thickness $h(\mu m)$, as k_z increases from 0 to 20, there is a notable decline in natural frequency, regardless of the $BaTiO_3 - CoFe_2O_4$ distribution. For instance, at $h = 20\mu m$, with a $0\% - 100\%$ distribution, natural frequency decreases from $3.0009MHz$ at $k_z = 0$ to $1.3352MHz$ at $k_z = 20$. Higher k_z values indicate a more percentage of epoxy in material gradation composition, which lowers stiffness and

Table 14: Natural frequency (MHz) of simply supported MEE FG microbeam ($b = 2h, \quad L = 20h$)

$h(\mu m)$	k_z	$BaTiO_3 - CoFe_2O_4$						
		0%-100%	**20%-80%**	**40%-60%**	**50%-50%**	**60%-40%**	**80%-20%**	**100%-0%**
20	0	3.0009	2.8571	2.7108	2.6363	2.5613	2.4071	2.2472
	0.5	2.5250	2.4124	2.2975	2.2391	2.1802	2.0589	1.9332
	1	2.2200	2.1283	2.0348	1.9872	1.9393	1.8404	1.7380
	5	1.5182	1.4840	1.4491	1.4313	1.4135	1.3766	1.3386
	10	1.3919	1.3731	1.3539	1.3441	1.3344	1.3141	1.2932
	15	1.3538	1.3411	1.3282	1.3216	1.3150	1.3013	1.2872
	20	1.3352	1.3260	1.3166	1.3118	1.3070	1.2970	1.2867
40	0	1.3578	1.2891	1.2191	1.1836	1.1476	1.0739	0.9974
	0.5	1.0979	1.0449	0.9909	0.9634	0.9356	0.8786	0.8194
	1	0.9270	0.8847	0.8415	0.8196	0.7973	0.7518	0.7045
	5	0.5204	0.5078	0.4950	0.4885	0.4820	0.4687	0.4550
	10	0.4603	0.4548	0.4492	0.4464	0.4436	0.4378	0.4318
	15	0.4502	0.4469	0.4435	0.4418	0.4401	0.4366	0.4330
	20	0.4481	0.4458	0.4435	0.4423	0.4411	0.4387	0.4362
100	0	0.5260	0.4989	0.4713	0.4572	0.4430	0.4139	0.3836
	0.5	0.4189	0.3980	0.3768	0.3660	0.3550	0.3326	0.3092
	1	0.3475	0.3310	0.3141	0.3055	0.2968	0.2789	0.2604
	5	0.1722	0.1677	0.1633	0.1610	0.1587	0.1541	0.1494
	10	0.1473	0.1458	0.1442	0.1434	0.1427	0.1411	0.1395
	15	0.1449	0.1441	0.1433	0.1429	0.1425	0.1417	0.1408
	20	0.1455	0.1450	0.1445	0.1442	0.1440	0.1434	0.1429

thus reduces the natural frequency. In summary, increasing thickness h, higher content of $CoFe_2O_4$, and larger power-law index k_z all contribute to lower natural frequencies. These parameters offer tunability in the design of microbeam resonators by adjusting stiffness through material composition and geometric factors.

5 Parametric Analysis of the Bi-Coated MEE-FGM Microbeam

In this section, the microbeam model is composed of an FG mixture of ($BaTiO_3 - CoFe_2O_4$) and epoxy, from which this mixture is controlled by the power law of FG materials in equations 71-72. The inner core is an isotropic material and it is composed of epoxy. The physical characteristics of these materials are listed in Table 4.

Figures 53-55 shows the bending response of a MEE bi-coated microbeam with

three deferent boundary conditions as simply supported, clamped, and clamped free, for various FG fraction index and $50\% - 50\%$ MEE mixture. As noticed the simply supported example give high deflection then the clamped example, and the clamped free give more important deflection. The nature of the bending response gives deferent electric and magnetic potential distribution along the length of the beam. As represented, electrical potential has positive value in all the points of the microbeam in simply supported case, unlike the clamped free, the electric potential has negative value across all the microbeam. In the clamped example it is noticed that the electric potential has negative value near the boundary ends of the microbeam, but in the middle the value is positive. All that is explained that the uniform load cause mechanical deformation who generate electrical potential across the microbeam. In regions of the microbeam where the material is compressed, the piezoelectric effect generates a positive electric charge (V) and the piezomagnetic effect generates a negative magnetic charge (A), and it is the opposites where the material is stretched, a negative electric and a positive magnetic charge are generated.

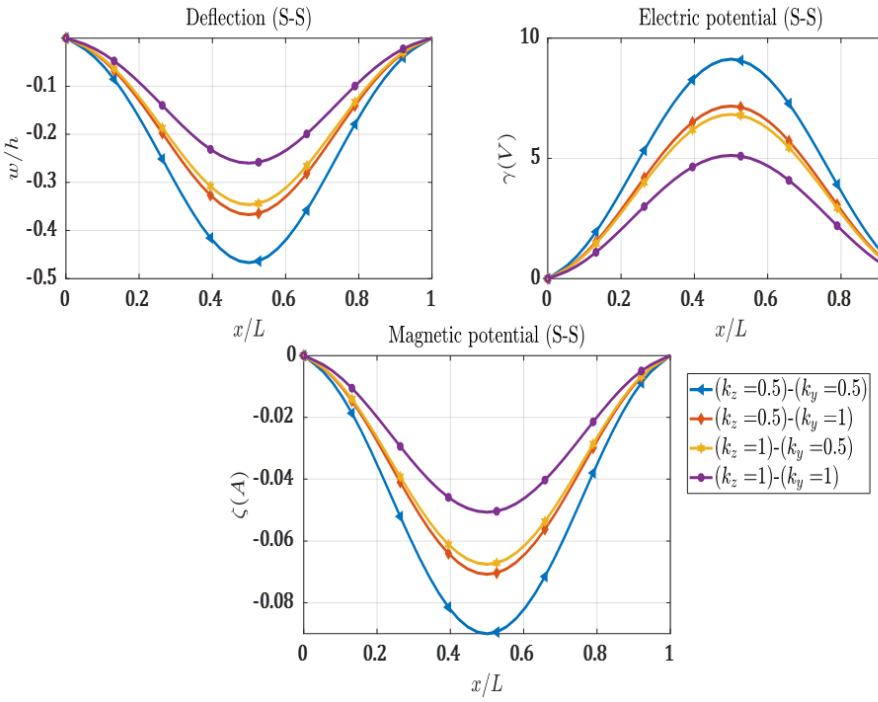


Figure 53: Deflection, electric potential and magnetic potential along the length of Simply supported microbeam with various FG fraction index and $50\% - 50\%$ $BaTiO_3 - CoFe_2O_4$ ($b = 2h$, $L = 20h$)

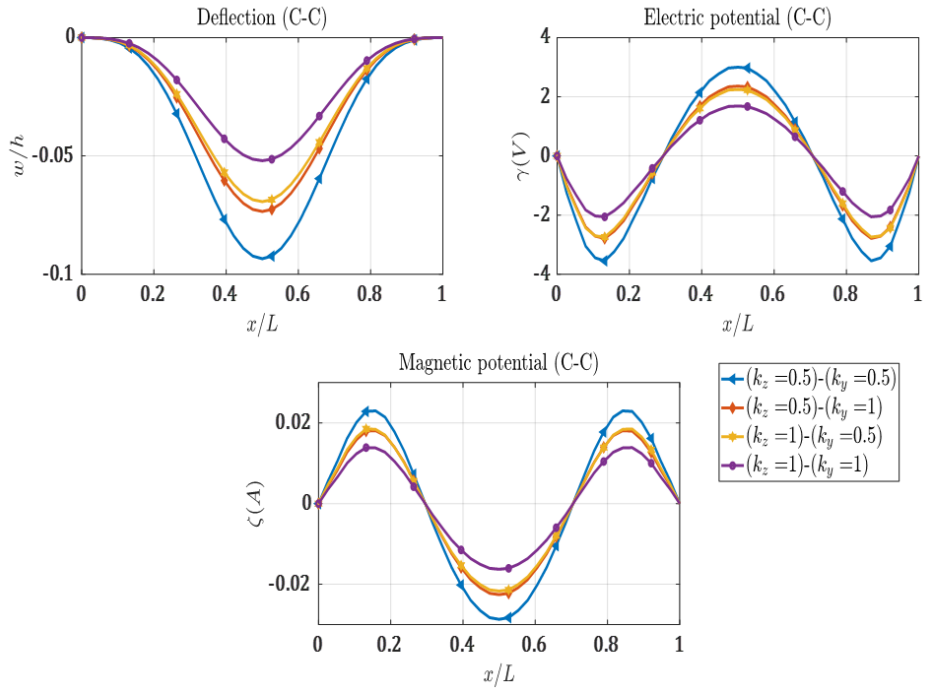


Figure 54: Deflection, electric potential and magnetic potential along the length of clamped microbeam with various FG fraction index and $50\% - 50\%$ $BaTiO_3 - CoFe_2O_4$ ($b = 2h$, $L = 20h$)

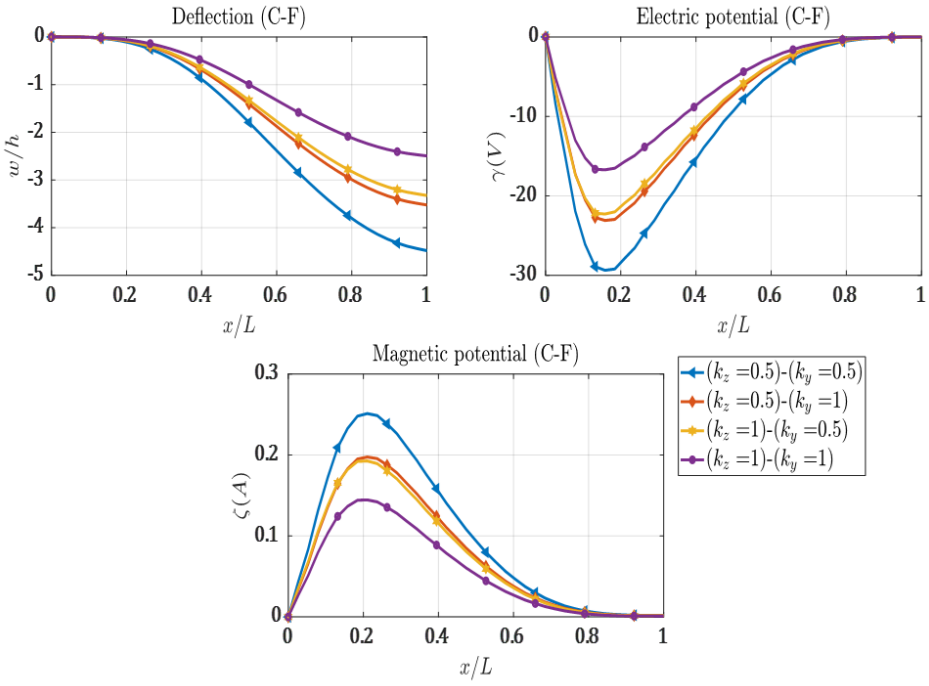


Figure 55: Deflection, electric potential and magnetic potential along the length of clamped free microbeam with various FG fraction index and $50\% - 50\%$ $BaTiO_3 - CoFe_2O_4$ ($b = 2h$, $L = 20h$)

Figures 56-58 illustrates the midspan "deflection, electric potential, and magnetic potential" for a doubly simply supported (figure 56), doubly clamped (figure 57), and clamped free (figure 58) versus the thickness of the beam with various FG gradation index and a $50\%-50\%$ MEE inner material mixture percentage of $BaTiO_3-CoFe_2O_4$. It is noticed that midspan deflection decrease with the augmentation of the thickness, this is physically reasonable because thicker beams tend to be stiffer and can resist bending or deflection more effectively under the same load. It is noticed for the three cases of boundary conditions the more the deflection decreases the less electric and magnetic potential there will be. As the beam becomes thicker, the mechanical strain induced by bending is distributed over a larger cross-sectional area, leading to a reduced deformation. Since the piezoelectric and piezomagnetic effects depends on the deformation, the electric and magnetic potentials decrease with increasing thickness.

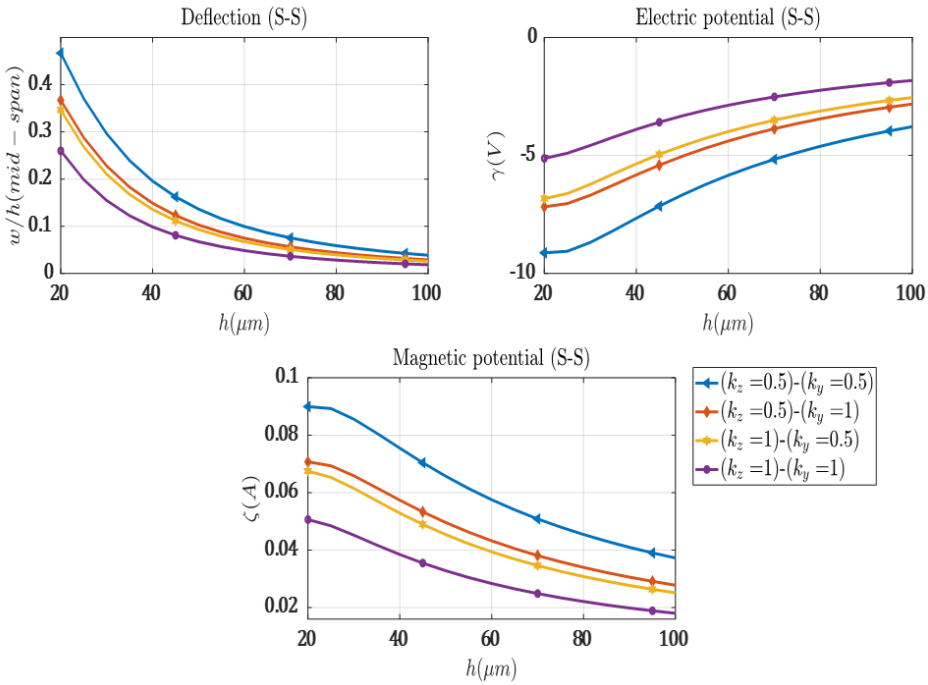


Figure 56: Simply supported microbeam midspan deflection, electric potential and magnetic potential with respect to the thickness, FG fraction index and $50\%-50\%$ $BaTiO_3-CoFe_2O_4$ ($b=2h$, $L=20h$)

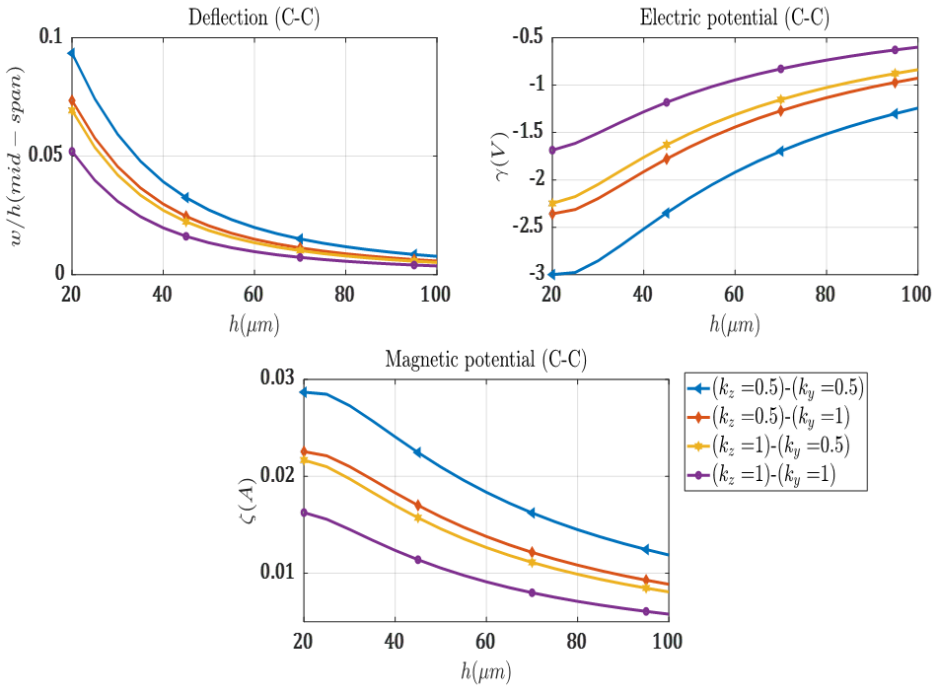


Figure 57: clamped microbeam midspan deflection, electric potential and magnetic potential with respect to the thickness, FG fraction index and $50\%-50\%BaTiO_3-CoFe_2O_4$ ($b=2h, \quad L=20h$)

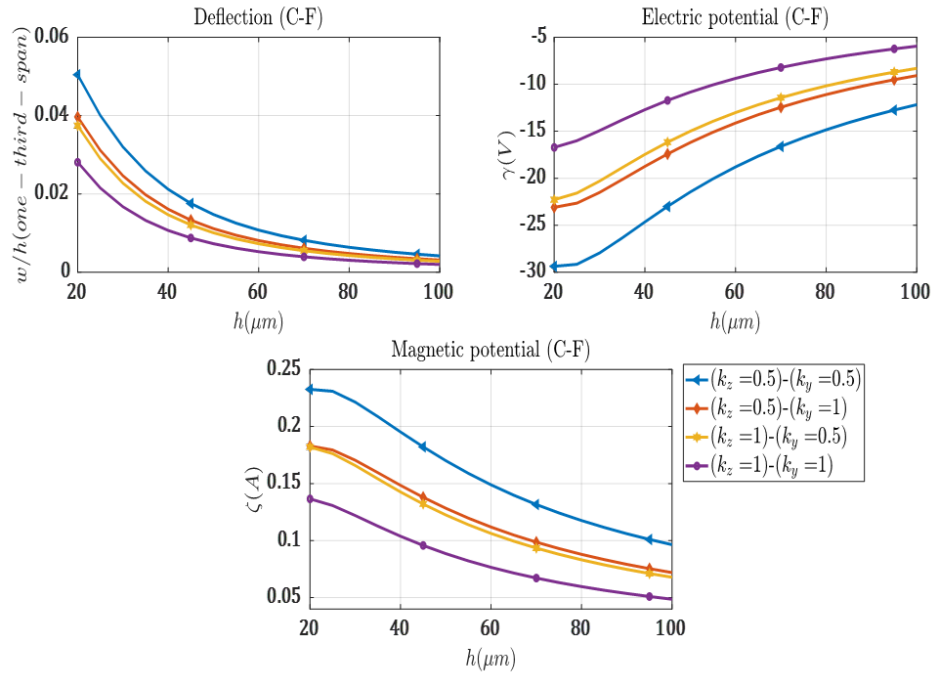


Figure 58: Clamped free microbeam midspan deflection, electric potential and magnetic potential with respect to the thickness, FG fraction index and $50\%-50\%BaTiO_3-CoFe_2O_4$ ($b=2h, \quad L=20h$)

Table 15: Midspan deflection with various FG fraction index and MEE core material mixture percentage $BaTiO_3 - CoFe_2O_4$ ($h = 20\mu m,\ b = 2h,\ L = 20h$).

$BaTiO_3$-$CoFe_2O_4$	k_z	S-S			C-C			C-F		
		$k_y = 0.5$	$k_y = 1$	$k_y = 5$	$k_y = 0.5$	$k_y = 1$	$k_y = 5$	$k_y = 0.5$	$k_y = 1$	$k_y = 5$
20%–80%	0.5	0.4334	0.3363	0.2329	0.0867	0.0673	0.0466	1.4744	1.1443	0.7924
	1	0.3161	0.2345	0.1551	0.0633	0.0470	0.0311	1.0756	0.7980	0.5278
	5	0.1738	0.1224	0.0771	0.0348	0.0245	0.0154	0.5914	0.4165	0.2625
40%–60%	0.5	0.4552	0.3563	0.2489	0.0911	0.0713	0.0498	1.5483	1.2120	0.8470
	1	0.3356	0.2508	0.1671	0.0672	0.0502	0.0335	1.1419	0.8534	0.5685
	5	0.1872	0.1325	0.0839	0.0375	0.0265	0.0168	0.6371	0.4508	0.2854
50%–50%	0.5	0.4668	0.3670	0.2578	0.0934	0.0735	0.0516	1.5878	1.2486	0.8770
	1	0.3463	0.2598	0.1738	0.0693	0.0520	0.0348	1.1779	0.8839	0.5912
	5	0.1947	0.1382	0.0877	0.0390	0.0277	0.0176	0.6625	0.4701	0.2983
60%–40%	0.5	0.4789	0.3784	0.2672	0.0958	0.0757	0.0535	1.6291	1.2873	0.9090
	1	0.3575	0.2694	0.1810	0.0716	0.0539	0.0362	1.2162	0.9166	0.6156
	5	0.2028	0.1443	0.0918	0.0406	0.0289	0.0184	0.6901	0.4911	0.3124
80%–20%	0.5	0.5051	0.4033	0.2881	0.1011	0.0807	0.0577	1.7179	1.3718	0.9801
	1	0.3822	0.2908	0.1972	0.0765	0.0582	0.0395	1.3001	0.9891	0.6707
	5	0.2211	0.1584	0.1014	0.0443	0.0317	0.0203	0.7522	0.5389	0.3448

The results presented in Tables 15 , 16, and 17 provide a comprehensive analysis of the midspan deflection, electric potential, and magnetic potential for a bi-coated FG microbeam composed of an internal MEE core material ($BaTiO_3 - CoFe_2O_4$ mixture) and an external epoxy layer. The analysis reveals that the mechanical and functional properties of the beam are significantly influenced by the FG gradation indices k_y and k_z, as well as the varying percentages of the MEE mixture. Specifically, the midspan deflection increases with higher $BaTiO_3$ content, indicating that greater proportions of $BaTiO_3$ make the beam more flexible. Conversely, increasing the values of k_y and k_z reduces the deflection, suggesting that steeper gradation profiles enhance the stiffness of the microbeam, which means low deflection, because the increase in FG gradation index led to the increase of the $BaTiO_3 - CoFe_2O_4$ mixture proportion and the reduce of the epoxy proportion. Among the boundary conditions, the deflection is smallest for the clamped-free (C-F) condition and largest for the simply supported (S-S) condition, with the clamped-clamped (C-C) condition lying in between. For the electric potential, the absolute values increase with higher $BaTiO_3$ content due to its significant contribution to the piezoelectric effect. Higher k_y and k_z values suppress the piezoelectric response, reducing the absolute value of the electric potential.

Table 16: Midspan Electric potential with various FG fraction index and MEE core material mixture percentage $BaTiO_3 - CoFe_2O_4$ ($h = 20\mu m,\ b = 2h,\ L = 20h$).

$BaTiO_3$-$CoFe_2O_4$	k_z	S-S			C-C			C-F		
		$k_y = 0.5$	$k_y = 1$	$k_y = 5$	$k_y = 0.5$	$k_y = 1$	$k_y = 5$	$k_y = 0.5$	$k_y = 1$	$k_y = 5$
20%–80%	0.5	-8.325	-6.460	-4.473	-2.735	-2.122	-1.470	-8.453	-6.560	-4.541
	1	-6.125	-4.544	-3.005	-2.015	-1.495	-0.989	-6.211	-4.608	-3.047
	5	-3.493	-2.460	-1.550	-1.152	-0.812	-0.512	-3.532	-2.487	-1.568
40%–60%	0.5	-8.878	-6.948	-4.855	-2.917	-2.283	-1.595	-9.014	-7.055	-4.930
	1	-6.604	-4.936	-3.288	-2.173	-1.624	-1.082	-6.696	-5.004	-3.333
	5	-3.821	-2.704	-1.711	-1.261	-0.892	-0.565	-3.863	-2.734	-1.730
50%–50%	0.5	-9.127	-7.176	-5.040	-2.998	-2.358	-1.656	-9.266	-7.286	-5.117
	1	-6.830	-5.125	-3.427	-2.247	-1.686	-1.128	-6.924	-5.196	-3.475
	5	-3.984	-2.827	-1.793	-1.314	-0.933	-0.592	-4.028	-2.858	-1.813
60%–40%	0.5	-9.377	-7.409	-5.231	-3.081	-2.434	-1.719	-9.520	-7.522	-5.311
	1	-7.061	-5.321	-3.574	-2.324	-1.751	-1.176	-7.159	-5.395	-3.623
	5	-4.155	-2.957	-1.881	-1.371	-0.976	-0.621	-4.201	-2.990	-1.902
80%–20%	0.5	-9.901	-7.906	-5.648	-3.253	-2.598	-1.856	-10.051	-8.026	-5.733
	1	-7.558	-5.749	-3.899	-2.487	-1.892	-1.283	-7.662	-5.828	-3.952
	5	-4.535	-3.249	-2.079	-1.496	-1.072	-0.686	-4.585	-3.284	-2.102

Similar to the deflection, the electric potential is most negative for the S-S condition and least negative for the C-F condition. Regarding the magnetic potential, higher $CoFe_2O_4$ content enhances this property, while higher $BaTiO_3$ content reduces it. steeper gradation profiles also decrease the magnetic potential, indicating that these profiles reduce the magnetostrictive effect. The magnetic potential follows a trend similar to the electric potential, with the highest values observed under S-S conditions and the lowest under C-F conditions. Overall, the choice of material composition and gradation indices depends on the specific requirements of the application, balancing mechanical, piezoelectric, and magnetostrictive properties. For applications requiring high piezoelectric response, a higher $BaTiO_3$ content and lower k_y and k_z values are recommended, whereas for applications demanding high magnetostrictive response, a higher $CoFe_2O_4$ content and lower k_y and k_z values are preferred. To minimize deflection for structural integrity, steeper gradation profiles should be used. By carefully selecting these parameters, engineers can optimize the performance of the FG beam for various multifunctional applications, ensuring that the desired mechanical and functional properties are achieved.

Table 17: Midspan Magnetic potential with various FG fraction index and MEE core material mixture percentage $BaTiO_3 - CoFe_2O_4$ ($h = 20\mu m,\ b = 2h,\ L = 20h$).

$BaTiO_3$-$CoFe_2O_4$	k_z	S-S			C-C			C-F		
		$k_y = 0.5$	$k_y = 1$	$k_y = 5$	$k_y = 0.5$	$k_y = 1$	$k_y = 5$	$k_y = 0.5$	$k_y = 1$	$k_y = 5$
20%–80%	0.5	0.0873	0.0677	0.0469	0.0278	0.0216	0.0149	0.0913	0.0708	0.0490
	1	0.0644	0.0478	0.0316	0.0206	0.0153	0.0101	0.0669	0.0496	0.0328
	5	0.0369	0.0260	0.0164	0.0120	0.0085	0.0053	0.0378	0.0266	0.0168
40%–60%	0.5	0.0895	0.0700	0.0489	0.0285	0.0223	0.0156	0.0935	0.0732	0.0511
	1	0.0667	0.0499	0.0332	0.0214	0.0160	0.0107	0.0693	0.0518	0.0345
	5	0.0388	0.0275	0.0174	0.0126	0.0089	0.0057	0.0398	0.0281	0.0178
50%–50%	0.5	0.0900	0.0708	0.0497	0.0287	0.0226	0.0158	0.0940	0.0739	0.0519
	1	0.0675	0.0507	0.0339	0.0217	0.0163	0.0109	0.0700	0.0526	0.0352
	5	0.0396	0.0281	0.0178	0.0129	0.0091	0.0058	0.0405	0.0288	0.0183
60%–40%	0.5	0.0897	0.0709	0.0501	0.0286	0.0226	0.0160	0.0936	0.0740	0.0522
	1	0.0677	0.0511	0.0343	0.0218	0.0164	0.0110	0.0702	0.0529	0.0355
	5	0.0401	0.0285	0.0181	0.0131	0.0093	0.0059	0.0410	0.0292	0.0186
80%–20%	0.5	0.0829	0.0662	0.0473	0.0266	0.0212	0.0152	0.0861	0.0688	0.0491
	1	0.0634	0.0482	0.0327	0.0205	0.0156	0.0106	0.0655	0.0498	0.0338
	5	0.0382	0.0274	0.0175	0.0125	0.0089	0.0057	0.0390	0.0280	0.0179

Figures 59–61 present the results from Tables 15–17, illustrating the electrical and magnetic potentials under various boundary conditions for a $50\% - 50\%$ $BaTiO_3 - CoFe_2O_4$ mixture. It is observed that an increase in k_y and k_z leads to a decrease in electrical and magnetic potentials. This is attributed to the fact that higher values of k_y and k_z correspond to a greater proportion of the magnetoelectric (MEE) $BaTiO_3 - CoFe_2O_4$ composite and a lower content of epoxy. Since $BaTiO_3 - CoFe_2O_4$ is more rigid than epoxy, this results in increased stiffness of the microbeam, reducing its deflection. However, greater flexibility is essential for achieving higher electrical and magnetic efficiency. Therefore, it is concluded that a higher proportion of the MEE material does not necessarily enhance electrical and magnetic output. The presence of epoxy increases flexibility, which, in turn, enhances the electrical and magnetic potentials.

In figure 62-64 the magnetic potential has an optimal value between $50\% - 50\%$ and $60\% - 40\%$ of $BaTiO_3 - CoFe_2O_4$ mixture, and this value increase more with the increase of FG index. The goal in this illustration is to make the mixture $BaTiO_3 - CoFe_2O_4$ more flexible by adding the epoxy material, but keeping the

maximum electrical and magnetic efficiency.

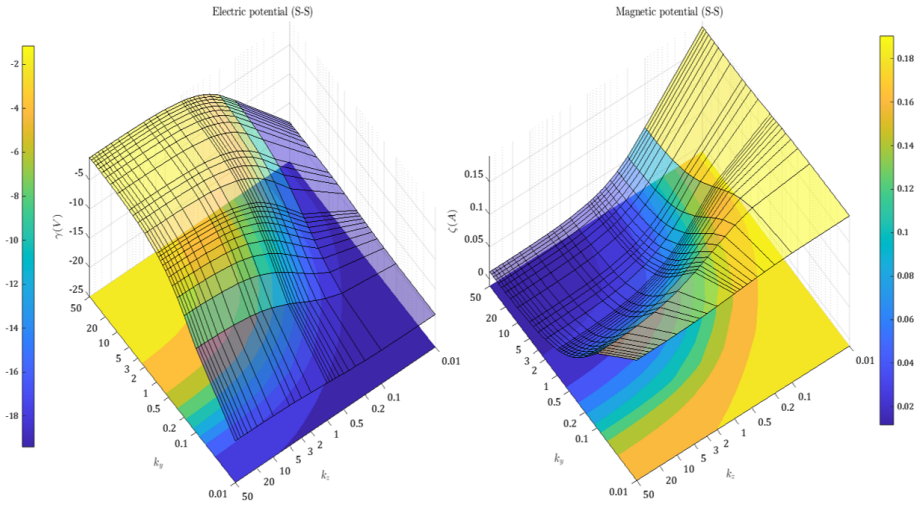


Figure 59: Electric and magnetic potentials at simply supported microbeam midspan with various FG fraction index and $50\% - 50\% BaTiO_3 - CoFe_2O_4$ ($h = 20\mu m, \quad b = 2h, \quad L = 20h$)

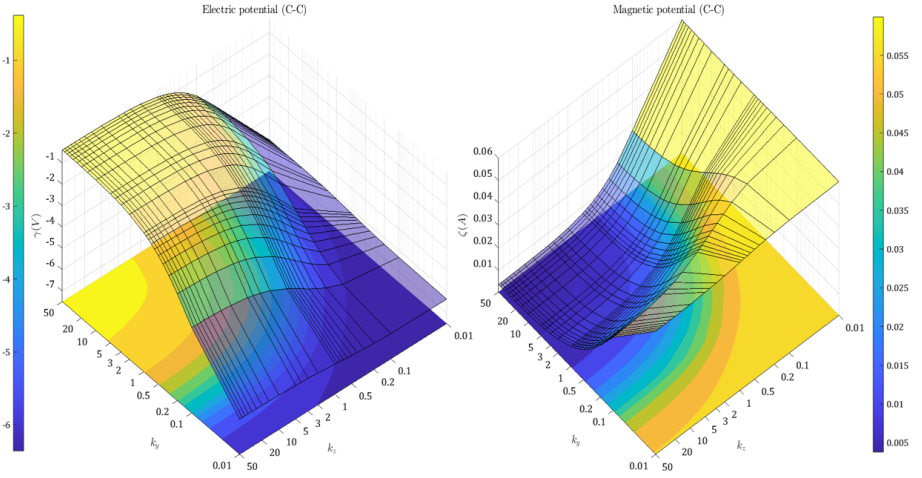


Figure 60: Electric and magnetic potentials at clamped microbeam midspan with various FG fraction index and $50\% - 50\% BaTiO_3 - CoFe_2O_4$ ($h = 20\mu m, \quad b = 2h, \quad L = 20h$)

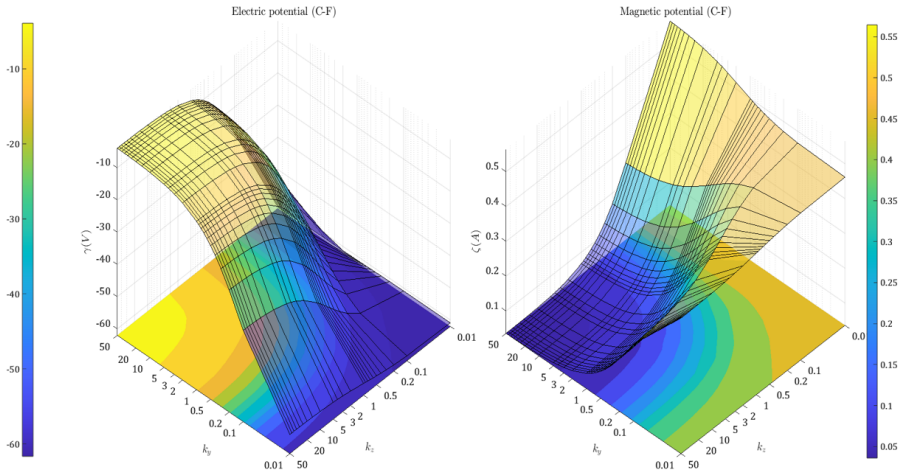


Figure 61: Electric and magnetic potentials at clamped microbeam midspan with various FG fraction index and $50\% - 50\% BaTiO_3 - CoFe_2O_4$ $(h = 20\mu m, \quad b = 2h, \quad L = 20h)$

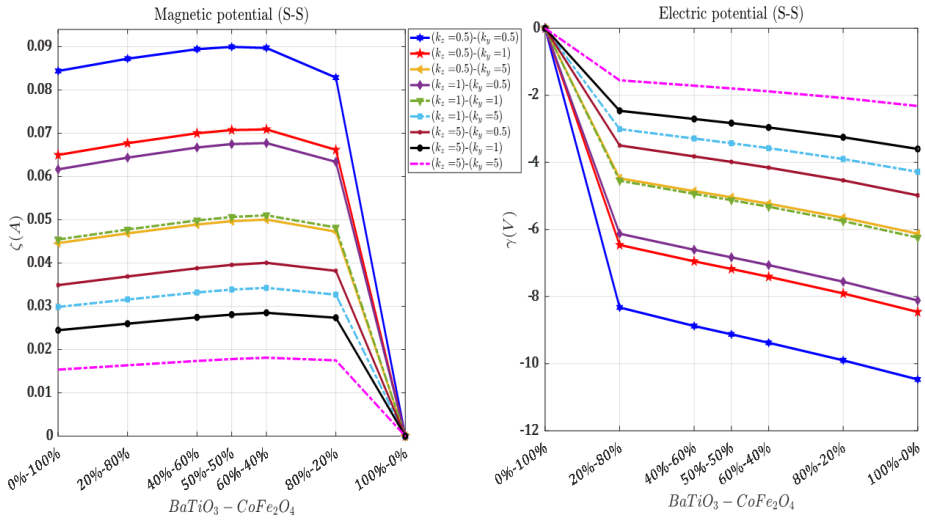


Figure 62: Electric and magnetic potentials at simply supported microbeam midspan with various FG fraction index and MEE inner material mixture percentage $BaTiO_3 - CoFe_2O_4$ $(h = 20\mu m, \quad b = 2h, \quad L = 20h)$

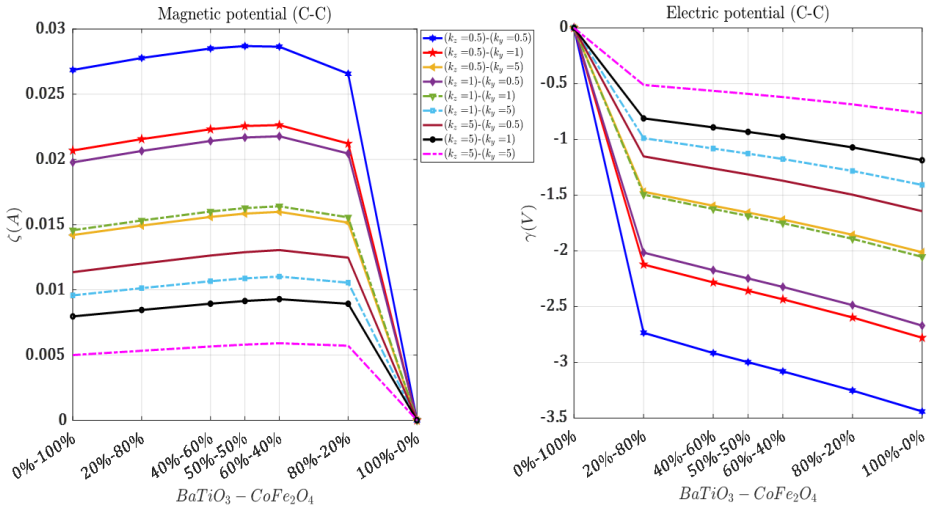


Figure 63: Electric and magnetic potentials at clamped microbeam midspan with various FG fraction index and MEE inner material mixture percentage $BaTiO_3 - CoFe_2O_4$ $(h = 20\mu m, \quad b = 2h, \quad L = 20h)$

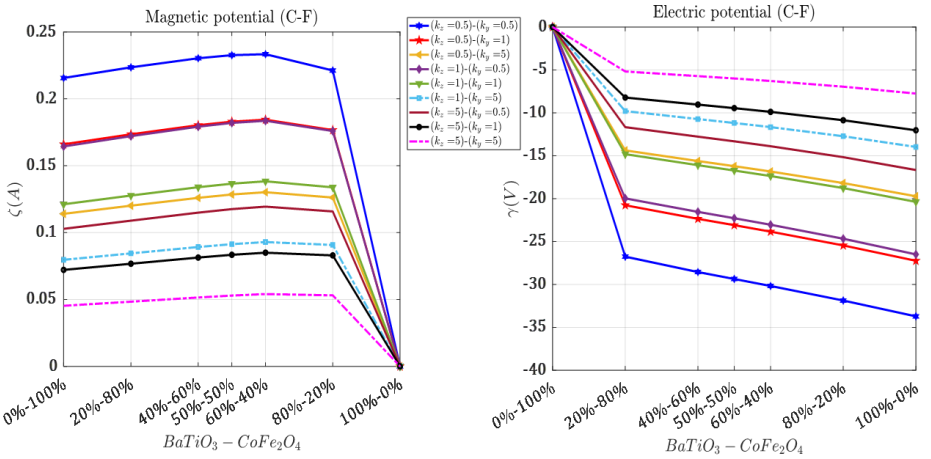


Figure 64: Electric and magnetic potentials at clamped free microbeam third-span with various FG fraction index and MEE inner material mixture percentage $BaTiO_3 - CoFe_2O_4$ $(h = 20\mu m, \quad b = 2h, \quad L = 20h)$

The natural frequency of a simply supported MEE FG microbeam composed of two materials ($BaTiO_3 - CoFe_2O_4$ and epoxy). As it is noticed in tables 18-19 there is a decrease in the value of natural frequency with respect to the increase in length-thickness ratio. Also, the natural frequency decrease with the rise of the FG gradation index. The value of natural frequency is higher when the MEE mixture is composed of $100\%CoFe_2O_4$ and it begins to decrease by increasing the percentage of $BaTiO_3$.

Table 18: Natural frequency (MHz) with various FG fraction index and MEE core material mixture percentage $BaTiO_3 - CoFe_2O_4\,(h = 20\mu m,\ b = 2h,\ \ L = 20h,)$

$BaTiO_3$-$CoFe_2O_4$	k_z	S-S			C-C			C-F		
		$k_y = 0.5$	$k_y = 1$	$k_y = 5$	$k_y = 0.5$	$k_y = 1$	$k_y = 5$	$k_y = 0.5$	$k_y = 1$	$k_y = 5$
20%–80%	0.5	1.6646	1.8223	2.1981	3.7726	4.1301	4.9818	0.5933	0.6495	0.7835
	1	1.7670	1.9402	2.3404	4.0048	4.3973	5.3042	0.6298	0.6915	0.8341
	5	1.9003	2.0802	2.4916	4.3070	4.7146	5.6470	0.6772	0.7413	0.8880
40%–60%	0.5	1.6190	1.7609	2.1054	3.6693	3.9908	4.7716	0.5770	0.6276	0.7504
	1	1.7095	1.8657	2.2336	3.8744	4.2284	5.0621	0.6092	0.6649	0.7961
	5	1.8273	1.9901	2.3696	4.1415	4.5105	5.3706	0.6512	0.7092	0.8445
50%–50%	0.5	1.5961	1.7299	2.0585	3.6174	3.9207	4.6653	0.5689	0.6165	0.7337
	1	1.6805	1.8281	2.1796	3.8088	4.1433	4.9398	0.5989	0.6515	0.7768
	5	1.7905	1.9447	2.3081	4.0581	4.4077	5.2311	0.6381	0.6931	0.8226
60%–40%	0.5	1.5731	1.6988	2.0112	3.5653	3.8502	4.5581	0.5607	0.6055	0.7168
	1	1.6514	1.7904	2.1252	3.7429	4.0578	4.8165	0.5886	0.6381	0.7574
	5	1.7536	1.8991	2.2461	3.9744	4.3044	5.0905	0.6249	0.6768	0.8005
80%–20%	0.5	1.5269	1.6360	1.9152	3.4605	3.7078	4.3406	0.5442	0.5831	0.6826
	1	1.5929	1.7141	2.0148	3.6101	3.8849	4.5663	0.5677	0.6109	0.7181
	5	1.6791	1.8069	2.1203	3.8056	4.0954	4.8056	0.5984	0.6440	0.7557

Table 19: Natural frequency (MHz) with various FG fraction index and MEE core material mixture percentage $BaTiO_3 - CoFe_2O_4\,(h = 20\mu m,\ b = 2h,\ \ L = 5h,)$

$BaTiO_3$-$CoFe_2O_4$	k_z	S-S			C-C			C-F		
		$k_y = 0.5$	$k_y = 1$	$k_y = 5$	$k_y = 0.5$	$k_y = 1$	$k_y = 5$	$k_y = 0.5$	$k_y = 1$	$k_y = 5$
20%80%	0.5	26.2953	28.7982	34.7054	59.4112	65.0726	78.4020	9.4349	10.3308	12.4563
	1	27.9352	30.6836	36.9650	63.1286	69.3460	83.5145	10.0190	11.0025	13.2644
	5	30.0746	32.9288	39.3703	67.9822	74.4386	88.9588	10.7799	11.8013	14.1242
40%60%	0.5	25.5762	27.8282	33.2417	57.7871	62.8813	75.0957	9.1767	9.9826	11.9308
	1	27.0265	29.5065	35.2788	61.0759	66.6866	79.7053	9.6928	10.5802	12.6592
	5	28.9199	31.5046	37.4440	65.3729	71.2198	84.6066	10.3657	11.2907	13.4330
50%50%	0.5	25.2150	27.3396	32.5015	56.9711	61.7776	73.4238	9.0470	9.8072	11.6650
	1	26.5694	28.9134	34.4266	60.0435	65.3465	77.7804	9.5288	10.3674	12.3534
	5	28.3389	30.7873	36.4717	64.0599	69.5986	82.4098	10.1573	11.0334	13.0841
60%40%	0.5	24.8524	26.8483	31.7550	56.1522	60.6677	71.7375	8.9168	9.6308	11.3970
	1	26.1104	28.3168	33.5675	59.0064	63.9986	75.8394	9.3641	10.1534	12.0450
	5	27.7550	30.0657	35.4921	62.7405	67.9677	80.1964	9.9479	10.7747	12.7326
80%20%	0.5	24.1230	25.8567	30.2402	54.5048	58.4276	68.3158	8.6549	9.2749	10.8532
	1	25.1855	27.1116	31.8244	56.9168	61.2752	71.9016	9.0321	9.7210	11.4194
	5	26.5772	28.6075	33.5058	60.0786	64.6718	75.7087	9.5255	10.2519	12.0199

General Conclusion

This thesis presented a comprehensive investigation into the static and dynamic behavior of sandwich, bilaterally coated, and bi-coated functionally graded (FG) magneto-electro-elastic (MEE) microbeams. The study employed a quasi-3D high-order beam theory in combination with the Differential Quadrature Finite Element Method (DQ-FEM), incorporating the Modified Couple Stress Theory (MCST) to account for microstructural effects. The proposed numerical framework was validated against existing literature, demonstrating a high degree of accuracy in predicting deflections, natural frequencies, and electromechanical potentials under various loading and boundary conditions.

The key findings of this research can be summarized as follows:

1. **Microstructural effects and beam thickness:** Incorporating MCST revealed that size-dependent effects introduce additional stiffness at the microscale. Thinner beams exhibited larger deflections and higher electric and magnetic potentials, whereas thicker beams resisted deformation, resulting in lower potentials and increased natural frequencies. The discrepancy between classical and MCST-based models became more pronounced for small-scale beams, highlighting the importance of accounting for microstructural influences in MEE microbeam design.

2. **Material composition and gradation effects:** The proportion of $BaTiO_3$ significantly enhanced the piezoelectric response, increasing

deflections and electric potentials, while $CoFe_2O_4$ content strengthened the magnetostrictive response, raising magnetic potentials. Functionally graded material (FGM) profiles strongly influenced the mechanical and electromechanical properties: steeper gradation increased stiffness, reducing deflection and piezoelectric/magnetic effects, while optimized FG combinations achieved maximum electrical and magnetic outputs.

3. **Boundary conditions and structural configuration:** Boundary conditions significantly impacted both mechanical and electromechanical responses. Simply supported beams exhibited the largest deflections and highest negative electric potentials, while clamped or clamped-free configurations provided more uniform distribution of potentials and higher stiffness. Sandwich, bilaterally coated, and bi-coated configurations displayed distinct behaviors, emphasizing the role of structural layering in tuning MEE responses.

4. **Dynamic behavior:** Natural frequencies were sensitive to beam geometry, FG gradation, and material composition. Increased length-to-thickness ratios or higher $BaTiO_3$ content generally reduced natural frequencies, while $CoFe_2O_4$-rich compositions increased vibrational stiffness. The results confirm that both mechanical and vibrational properties are highly sensitive to material distribution and microstructural effects.

Overall, the findings of this thesis demonstrate that the careful selection of material composition, gradation profile, and beam geometry allows precise control of the mechanical, electrical, and magnetic responses of MEE microbeams. The developed quasi-3D DQ-FEM framework, validated with MCST, provides a robust tool for designing next-generation smart microstructures and functionally graded materials at the microscale.

Future work may include the investigation of nonlinear mechanical and electromechanical effects, temperature-dependent behavior, and experimental validation to further enhance the predictive capability and applicability of the proposed models.

References

[1] M. R. Farajpour, A. R. Shahidi, A. Hadi, and A. Farajpour. Influence of initial edge displacement on the nonlinear vibration, electrical and magnetic instabilities of magneto-electro-elastic nanofilms. *Mechanics of Advanced Materials and Structures*, 26(17): 1469–1481, 2019. ISSN 1537-6494. doi: https://doi.org/10.1080/15376494.2018.1432820. URL https://doi.org/10.1080/15376494.2018.1432820. doi: 10.1080/15376494.2018.1432820.

[2] M. Haghgoo, Mohammad-Kazem Hassanzadeh-Aghdam, and R. Ansari. Effect of piezoelectric interphase on the effective magneto-electro-elastic properties of three-phase smart composites: A micromechanical study. *Mechanics of Advanced Materials and Structures*, 26(23):1935–1950, 2019. ISSN 1537-6494. doi: https://doi.org/10.1080/15376494.2018.1455932. URL https://doi.org/10.1080/15376494.2018.1455932. doi: 10.1080/15376494.2018.1455932.

[3] S. Sahmani and M. M. Aghdam. Nonlocal strain gradient shell model for axial buckling and postbuckling analysis of magneto-electro-elastic composite nanoshells. *Composites Part B: Engineering*, 132:258–274, 2018. doi: 10.1016/j.compositesb.2017.09.004.

[4] Valery G. Yakhno. An explicit formula for modeling wave propagation in magneto-electro-elastic materials. *Journal of Electromagnetic Waves and Applications*, 32(7): 899–912, 2018. ISSN 0920-5071. doi: 10.1080/09205071.2017.1410076. URL https://doi.org/10.1080/09205071.2017.1410076. doi: 10.1080/09205071.2017.1410076.

[5] Wei Chen, Zhi Yan, and Lin Wang. On mechanics of functionally graded hard-magnetic soft beams. *International Journal of Engineering Science*, 157:103391, 2020. ISSN 0020-7225. doi: https://doi.org/10.1016/j.ijengsci.2020.103391. URL https://www.sciencedirect.com/science/article/pii/S0020722520301786.

[6] E. Taati. On buckling and post-buckling behavior of functionally graded micro-beams in thermal environment. *International Journal of Engineering Science*, 128:63–78, 2018. doi: 10.1016/j.ijengsci.2018.03.010.

[7] R. K. Bhangale and N. Ganesan. Free vibration of simply supported functionally graded and layered magneto-electro-elastic plates by finite element method. *Journal of Sound and Vibration*, 294(4):1016–1038, 2006. doi: 10.1016/j.jsv.2005.12.030.

[8] J. Sladek, V. Sladek, S. Krahulec, C. S. Chen, and D. L. Young. Analyses of Circular

Magnetoelectroelastic Plates with Functionally Graded Material Properties. *Mechanics of Advanced Materials and Structures*, 22(6):479–489, 2015. doi: 10.1080/15376494.2013.807448.

[9] Vinyas Mahesh. Porosity effect on the nonlinear deflection of functionally graded magneto-electro-elastic smart shells under combined loading. *Mechanics of Advanced Materials and Structures*, 29(19):2707–2725, 2022. ISSN 1537-6494. doi: 10.1080/15376494.2021.1875086. URL https://doi.org/10.1080/15376494.2021.1875086. doi: 10.1080/15376494.2021.1875086.

[10] G. Y. Zhang, Y. L. Qu, X. L. Gao, and F. Jin. A transversely isotropic magneto-electro-elastic Timoshenko beam model incorporating microstructure and foundation effects. *Mechanics of Materials*, 149:103412, 2020. doi: 10.1016/j.mechmat.2020.103412.

[11] Jun Hong, Shaopeng Wang, Gongye Zhang, and Changwen Mi. On the bending and vibration analysis of functionally graded magneto-electro-elastic timoshenko microbeams. *Crystals*, 11 (10):1206, 2021. ISSN 2073-4352. doi: https://doi.org/10.3390/cryst11101206. URL https://www.mdpi.com/2073-4352/11/10/1206.

[12] Jun Hong, Shaopeng Wang, Xinyuan Qiu, and Gongye Zhang. Bending and wave propagation analysis of magneto-electro-elastic functionally graded porous microbeams. *Crystals*, 12(5): 732, 2022. ISSN 2073-4352. doi: https://doi.org/10.3390/cryst12050732. URL https://doi.org/10.3390/cryst12050732.

[13] Y. L. Qu, P. Li, G. Y. Zhang, F. Jin, and X. L. Gao. A microstructure-dependent anisotropic magneto-electro-elastic Mindlin plate model based on an extended modified couple stress theory. *Acta Mechanica*, 231(10):4323–4350, 2020. doi: 10.1007/s00707-020-02745-0.

[14] D. C. C. Lam, F. Yang, A. C. M. Chong, J. Wang, and P. Tong. Experiments and theory in strain gradient elasticity. *Journal of the Mechanics and Physics of Solids*, 51(8):1477–1508, 2003. doi: 10.1016/S0022-5096(03)00053-X.

[15] A. W. McFarland and J. S. Colton. Role of material microstructure in plate stiffness with relevance to microcantilever sensors. *Journal of Micromechanics and Microengineering*, 15(5): 1060, 2005. doi: 10.1088/0960-1317/15/5/024.

[16] R. D. Mindlin. Influence of couple-stresses on stress concentrations. *Experimental Mechanics*, 3(1):1–7, 1963. doi: 10.1007/BF02327219.

[17] R. D. Mindlin. Micro-structure in linear elasticity. *Archive for Rational Mechanics and Analysis*, 16(1):51–78, 1964. doi: 10.1007/BF00248490.

[18] R. A. Toupin. Elastic materials with couple-stresses. *Archive for Rational Mechanics and Analysis*, 11(1):385–414, 1962. doi: 10.1007/BF00253945.

[19] B.S. Altan and E.C. Aifantis. On Some Aspects in the Special Theory of Gradient Elasticity. *Journal of the Mechanical Behavior of Materials*, 8(3):231–282, 1997. doi: 10.1515/JMBM.1997.8.3.231.

[20] R. D. Mindlin and N. N. Eshel. On first strain-gradient theories in linear elasticity. *International Journal of Solids and Structures*, 4(1):109–124, 1968. doi: 10.1016/0020-7683(68)90036-X.

[21] C. Polizzotto. A hierarchy of simplified constitutive models within isotropic strain gradient elasticity. *European Journal of Mechanics - A/Solids*, 61:92–109, 2017. doi: 10.1016/j.euromechsol.2016.09.006.

[22] A. C. Eringen. On differential equations of nonlocal elasticity and solutions of screw dislocation and surface waves. *Journal of Applied Physics*, 54(9):4703–4710, 1983. doi: 10.1063/1.332803.

[23] F. Ebrahimi and M. R. Barati. Vibration analysis of embedded biaxially loaded magneto-electrically actuated inhomogeneous nanoscale plates. *Journal of Vibration and Control*, 24(16):3587–3607, 2018. doi: 10.1177/1077546317708105.

[24] A. Kiani, M. Sheikhkhoshkar, A. Jamalpoor, and M. Khanzadi. Free vibration problem of embedded magneto-electro-thermo-elastic nanoplate made of functionally graded materials via nonlocal third-order shear deformation theory. *Journal of Intelligent Material Systems and Structures*, 29(5):741–763, 2018. doi: 10.1177/1045389x17721034.

[25] H. Liu and Z. Lv. Vibration performance evaluation of smart magneto-electro-elastic nanobeam with consideration of nanomaterial uncertainties. *Journal of Intelligent Material Systems and Structures*, 30(18-19):2932–2952, 2019. doi: 10.1177/1045389x19873418.

[26] W.-s. Xiao, Y. Gao, and H. Zhu. Buckling and post-buckling of magneto-electro-thermo-elastic functionally graded porous nanobeams. *Microsystem Technologies*, 25(6):2451–2470, 2019. doi: 10.1007/s00542-018-4145-2.

[27] C. W. Lim, G. Zhang, and J. N. Reddy. A higher-order nonlocal elasticity and strain gradient theory and its applications in wave propagation. *Journal of the Mechanics and Physics of Solids*, 78:298–313, 2015. doi: 10.1016/j.jmps.2015.02.001.

[28] X. Li, L. Li, Y. Hu, Z. Ding, and W. Deng. Bending, buckling and vibration of axially functionally graded beams based on nonlocal strain gradient theory. *Composite Structures*, 165:250–265, 2017. doi: 10.1016/j.compstruct.2017.01.032.

[29] M. Şimşek. Nonlinear free vibration of a functionally graded nanobeam using nonlocal strain gradient theory and a novel Hamiltonian approach. *International Journal of Engineering Science*, 105:12–27, 2016. doi: 10.1016/j.ijengsci.2016.04.013.

[30] S. Wang, J. Hong, S. Gu, Z. Xiao, and G. Zhang. A size-dependent isogeometric model for magneto-electro-elastic graded curved beams in advanced structures. *Composite Structures*, 358:118877, 2025. doi: 10.1016/j.compstruct.2025.118877.

[31] Y.-f. Zheng, D.-y. Qu, L.-c. Liu, and C.-p. Chen. Size-dependent nonlinear bending analysis of nonlocal magneto-electro-elastic laminated nanobeams resting on elastic foundation.

International Journal of Non-Linear Mechanics, 148:104255, 2023. doi: 10.1016/j.ijnonlinmec.2022.104255.

[32] B. Alibeigi, Y. Tadi Beni, and F. Mehralian. On the thermal buckling of magneto-electro-elastic piezoelectric nanobeams. *The European Physical Journal Plus*, 133(3): 133, 2018. doi: 10.1140/epjp/i2018-11954-7.

[33] A. Ghobadi, Y. T. Beni, and H. Golestanian. Nonlinear thermo-electromechanical vibration analysis of size-dependent functionally graded flexoelectric nano-plate exposed magnetic field. *Archive of Applied Mechanics*, 90(9):2025–2070, 2020. doi: 10.1007/s00419-020-01708-0.

[34] Y.-f. Zheng, Y. Zhou, F. Wang, and C.-p. Chen. Nonlinear deformation analysis of magneto-electro-elastic nanobeams resting on elastic foundation by using nonlocal modified couple stress theory. *European Journal of Mechanics - A/Solids*, 103:105158, 2024. doi: 10.1016/j.euromechsol.2023.105158.

[35] B. Habibi, Y. T. Beni, and F. Mehralian. Free vibration of magneto-electro-elastic nanobeams based on modified couple stress theory in thermal environment. *Mechanics of Advanced Materials and Structures*, 26(7):601–613, 2019. doi: 10.1080/15376494.2017.1410902.

[36] B. Alibeigi and Y. Tadi Beni. On the size-dependent magneto/electromechanical buckling of nanobeams. *The European Physical Journal Plus*, 133(10):398, 2018. doi: 10.1140/epjp/i2018-12208-6.

[37] Y.-f. Zheng, L.-C. Liu, D.-y. Qu, and C.-p. Chen. Nonlinear postbuckling analysis of magneto-electro-thermo-elastic laminated microbeams based on modified couple stress theory. *Applied Mathematical Modelling*, 118:89–106, 2023. doi: 10.1016/j.apm.2023.01.021.

[38] S. Fattaheian Dehkordi and Y. Tadi Beni. Size-dependent continuum-based model of a truncated flexoelectric/flexomagnetic functionally graded conical nano/microshells. *Applied Physics A*, 128(4):320, 2022. doi: 10.1007/s00339-022-05386-3.

[39] Z. Lyu and M. Ma. Nonlinear dynamic modeling of geometrically imperfect magneto-electro-elastic nanobeam made of functionally graded material. *Thin-Walled Structures*, 191:111004, 2023. doi: 10.1016/j.tws.2023.111004.

[40] S. Wang, J. Hong, D. Wei, and G. Zhang. Bending and wave propagation analysis of axially functionally graded beams based on a reformulated strain gradient elasticity theory. *Applied Mathematics and Mechanics*, 44(10):1803–1820, 2023. doi: 10.1007/s10483-023-3042-6.

[41] S. Wang, J. Hong, S. Yin, and G. Zhang. Isogeometric analysis of magneto-electro-elastic functionally graded Mindlin microplates. *Thin-Walled Structures*, 198:111740, 2024. doi: 10.1016/j.tws.2024.111740.

[42] Ö Civalek, M. Akpınar, B. Uzun, and M. Ö. Yaylı. Dynamics of a non-circular-shaped nanorod with deformable boundaries based on second-order strain gradient theory. *Archive of Applied Mechanics*, 94(11):3555–3572, 2024. doi: 10.1007/s00419-024-02683-6.

[43] B. Uzun, Ö. Civalek, and M. Ö. Yaylı. Torsional and axial vibration of restrained saturated nanorods via strain gradient elasticity. *Archive of Applied Mechanics*, 93(4):1605–1630, 2023. doi: 10.1007/s00419-022-02348-2.

[44] B. Uzun, M. Ö. Yaylı, and Ö. Civalek. Elastic medium and torsional spring effects on the nonlocal dynamic of functionally graded porous nanotubes. *Archive of Applied Mechanics*, 94 (5):1291–1311, 2024. doi: 10.1007/s00419-024-02576-8.

[45] G. T. Luu, Ö. Civalek, and B. Van Tuyen. The mechanical response of nanobeams considering the flexoelectric phenomenon in the temperature environment. *Archive of Applied Mechanics*, 94(3):493–514, 2024. doi: 10.1007/s00419-023-02532-y.

[46] G. Y. Zhang, Z. Z. He, X. L. Gao, and H. W. Zhou. Band gaps in a periodic electro-elastic composite beam structure incorporating microstructure and flexoelectric effects. *Archive of Applied Mechanics*, 93(1):245–260, 2023. doi: 10.1007/s00419-021-02088-9.

[47] V.-H. Dang and Q.-C. Do. Nonlinear vibration and stability of functionally graded porous microbeam under electrostatic actuation. *Archive of Applied Mechanics*, 91(5):2301–2329, 2021. doi: 10.1007/s00419-021-01884-7.

[48] Ö Civalek, B. Uzun, and M. Ö. Yaylı. Size-dependent nonlinear stability response of perforated nano/microbeams via Fourier series. *Archive of Applied Mechanics*, 93(12): 4425–4443, 2023. doi: 10.1007/s00419-023-02501-5.

[49] M. Eroğlu, İ. Esen, and M. A. Koç. Thermal vibration and buckling analysis of magneto-electro-elastic functionally graded porous higher-order nanobeams using nonlocal strain gradient theory. *Acta Mechanica*, 235(2):1175–1211, 2024. doi: 10.1007/s00707-023-03793-y.

[50] K. G. Aktaş. Three-dimensional thermomechanical wave propagation analysis of sandwich nanoplate with graphene-reinforced foam core and magneto-electro-elastic face layers using nonlocal strain gradient elasticity theory. *Acta Mechanica*, 235(9):5587–5619, 2024. doi: 10.1007/s00707-024-04001-1.

[51] M. Arefi and A. M. Zenkour. Transient sinusoidal shear deformation formulation of a size-dependent three-layer piezo-magnetic curved nanobeam. *Acta Mechanica*, 228(10): 3657–3674, 2017. doi: 10.1007/s00707-017-1892-6.

[52] T.-K. Nguyen, T. P. Vo, and H.-T. Thai. Static and free vibration of axially loaded functionally graded beams based on the first-order shear deformation theory. *Composites Part B: Engineering*, 55:147–157, 2013. doi: 10.1016/j.compositesb.2013.06.011.

[53] S.-R. Li and R. C. Batra. Relations between buckling loads of functionally graded Timoshenko and homogeneous Euler–Bernoulli beams. *Composite Structures*, 95:5–9, 2013. doi: 10.1016/j.compstruct.2012.07.027.

[54] T.-K. Nguyen and B.-D. Nguyen. A new higher-order shear deformation theory for static,

buckling and free vibration analysis of functionally graded sandwich beams. *Journal of Sandwich Structures & Materials*, 17(6):613–631, 2015. doi: 10.1177/1099636215589237.

[55] P. Van Vinh. Deflections, stresses and free vibration analysis of bi-functionally graded sandwich plates resting on Pasternak's elastic foundations via a hybrid quasi-3D theory. *Mechanics Based Design of Structures and Machines*, pages 1–32, 2021. doi: 10.1080/15397734.2021.1894948.

[56] B. Adhikari and B. N. Singh. Dynamic response of functionally graded plates resting on a two-parameter-based elastic foundation model using a quasi-3D theory. *Mechanics Based Design of Structures and Machines*, 47(4):399–429, 2019. doi: 10.1080/15397734.2018.1555965.

[57] I. Bensaid and A. Saimi. Dynamic investigation of functionally graded porous beams resting on viscoelastic foundation using generalised differential quadrature method. *Australian Journal of Mechanical Engineering*, pages 1–20, 2022. doi: 10.1080/14484846.2021.2017115.

[58] Mouloud Dahmane, Mourad Benadouda, Ahmed Fellah, Ahmed Saimi, Ait Atmane Hassen, and Ismail Bensaid. Porosities-dependent wave propagation in bi-directional functionally graded cantilever beam with higher-order shear model. *Mechanics of Advanced Materials and Structures*, 31(26):8018–8028, 2024. doi: 10.1080/15376494.2023.2253546. URL https://doi.org/10.1080/15376494.2023.2253546.

[59] S. Ahmed, H. Abdelhamid, B. Ismail, and F. Ahmed. An Differential Quadrature Finite Element and the Differential Quadrature Hierarchical Finite Element Methods for the Dynamics Analysis of on Board Shaft. *European Journal of Computational Mechanics*, 29 (4-6):303–344, 2021. doi: 10.13052/ejcm1779-7179.29461.

[60] I. E. Houalef, I. Bensaid, A. Saimi, and A. Cheikh. An analysis of vibration and buckling behaviors of nano-composite beams reinforced with agglomerated carbon nanotubes via differential quadrature finite element method. *Mechanics of Advanced Materials and Structures*, pages 1–19, 2023. doi: 10.1080/15376494.2023.2185706.

[61] A. Saimi, I. Bensaid, and Ö. Civalek. A study on the crack presence effect on dynamical behaviour of bi-directional compositionally imperfect material graded micro beams. *Composite Structures*, 316:117032, 2023. doi: 10.1016/j.compstruct.2023.117032.

[62] A. Saimi, I. Bensaid, and I. E. Houalef. Dynamic analysis of a porous microbeam model based on refined beam strain gradient theory via differential quadrature hierarchical finite element method. *Advances in materials Research*, 12(2):133–159, 2023. doi: 10.12989/amr.2023.12.2.133.

[63] H. Godfroid. *Métallurgie pour mécaniciens: Propriétés générales des alliages, leur traitement thermique*. Métallurgie pour mécaniciens. Société de publications mécaniques, 1950. URL https://books.google.dz/books?id=aKPVAAAAMAAJ.

[64] R.K. Rajput. *A Textbook of Manufacturing Technology: Manufacturing Processes*. Laxmi, 2007. ISBN 9788131802441. URL https://books.google.com.bd/books?id=6wFuw6wufTMC.

[65] B. Craig. Limitations of alloying to improve the threshold for hydrogen stress cracking of steels. In N. R. Moody and A. W. Thompson, editors, *Hydrogen Effects on Material Behavior*.

[66] Sp.G. Pantelakis and N.D. Alexopoulos. Assessment of the ability of conventional and advanced wrought aluminum alloys for mechanical performance in light-weight applications. *Materials & Design*, 29(1):80–91, 2008. ISSN 0261-3069. doi: https://doi.org/10.1016/j.matdes.2006.12.004. URL https://www.sciencedirect.com/science/article/pii/S026130690600389X.

[67] R.M. Jones. *Mechanics Of Composite Materials*. 500 Tips. Taylor & Francis, 1998. ISBN 9781560327127. URL https://books.google.dz/books?id=oMph2kNG3yAC.

[68] J.N. Reddy. *Mechanics of Laminated Composite Plates and Shells: Theory and Analysis, Second Edition*. Applied and Computational Mechanics. CRC Press, 2003. ISBN 9780203502808. URL https://books.google.dz/books?id=eeUr_AJiGRcC.

[69] R.F. Gibson. *Principles of Composite Material Mechanics*. Mechanical Engineering. CRC Press, 2011. ISBN 9781439850060. URL https://books.google.dz/books?id=y3fRBQAAQBAJ.

[70] An Chen and Julio F. Davalos. A solution including skin effect for stiffness and stress field of sandwich honeycomb core. *International Journal of Solids and Structures*, 42(9):2711–2739, 2005. ISSN 0020-7683. doi: https://doi.org/10.1016/j.ijsolstr.2004.09.042. URL https://www.sciencedirect.com/science/article/pii/S002076830400544X.

[71] S. S. Rao and M. Sunar. Piezoelectricity and its use in disturbance sensing and control of flexible structures: A survey. *Applied Mechanics Reviews*, 47(4):113–123, 04 1994. ISSN 0003-6900. doi: 10.1115/1.3111074. URL https://doi.org/10.1115/1.3111074.

[72] Hyeong Jae Lee, Shujun Zhang, Yoseph Bar-Cohen, and Stewart Sherrit. High temperature, high power piezoelectric composite transducers. *Sensors*, 14(8):14526–14552, 2014. ISSN 1424-8220. doi: 10.3390/s140814526. URL https://www.mdpi.com/1424-8220/14/8/14526.

[73] Sumio Iijima. Helical microtubules of graphitic carbon. *Nature*, 354(6348):56–58, 1991. ISSN 1476-4687. doi: 10.1038/354056a0. URL https://doi.org/10.1038/354056a0.

[74] Jan Sandler, Philipp Werner, Milo S.P Shaffer, Vitaly Demchuk, Volker Altstädt, and Alan H Windle. Carbon-nanofibre-reinforced poly(ether ether ketone) composites. *Composites Part A: Applied Science and Manufacturing*, 33(8):1033–1039, 2002. ISSN 1359-835X. doi: https://doi.org/10.1016/S1359-835X(02)00084-2. URL https://www.sciencedirect.com/science/article/pii/S1359835X02000842.

[75] Xiaoyi Gong, Jun Liu, Suresh Baskaran, Roger D. Voise, and James S. Young. Surfactant-assisted processing of carbon nanotube/polymer composites. *Chemistry of*

Materials, 12(4):1049–1052, 2000. ISSN 0897-4756. doi: 10.1021/cm9906396. URL https://doi.org/10.1021/cm9906396. doi: 10.1021/cm9906396.

[76] Eric W. Wong, Paul E. Sheehan, and Charles M. Lieber. Nanobeam mechanics: Elasticity, strength, and toughness of nanorods and nanotubes. *Science*, 277(5334):1971–1975, 1997. doi: 10.1126/science.277.5334.1971. URL https://www.science.org/doi/abs/10.1126/science.277.5334.1971.

[77] Q. Wang, S.T. Quek, and V.K. Varadan. Torsional buckling of carbon nanotubes. *Physics Letters A*, 367(1):135–139, 2007. ISSN 0375-9601. doi: https://doi.org/10.1016/j.physleta.2007.02.099. URL https://www.sciencedirect.com/science/article/pii/S037596010700360X.

[78] X. Wang and H. Cai. Effects of initial stress on non-coaxial resonance of multi-wall carbon nanotubes. *Acta Materialia*, 54(8):2067–2074, 2006. ISSN 1359-6454. doi: https://doi.org/10.1016/j.actamat.2005.12.039. URL https://www.sciencedirect.com/science/article/pii/S1359645406000620.

[79] S. Suresh and A. Mortensen. *Fundamentals of Functionally Graded Materials: Processing and Thermomechanical Behaviour of Graded Metals and Metal-ceramic Composites*. Book (Institute of Materials (Great Britain))). IOM Communications Limited, 1998. ISBN 9781861250636. URL https://books.google.dz/books?id=ow8pAQAAMAAJ.

[80] Jacob Aboudi, Steven M. Arnold, and Marek-Jerzy Pindera. Response of functionally graded composites to thermal gradients. *Composites Engineering*, 4(1):1–18, 1994. ISSN 0961-9526. doi: https://doi.org/10.1016/0961-9526(94)90003-5. URL https://www.sciencedirect.com/science/article/pii/0961952694900035. Use of Composites in Functionally Graded Materials.

[81] Victor Birman and Larry W. Byrd. Modeling and analysis of functionally graded materials and structures. *Applied Mechanics Reviews*, 60(5):195–216, 09 2007. ISSN 0003-6900. doi: 10.1115/1.2777164. URL https://doi.org/10.1115/1.2777164.

[82] Valmik Bhavar, Prakash Kattire, Sandeep Thakare, Sachin patil, and RKP Singh. A review on functionally gradient materials (fgms) and their applications. *IOP Conference Series: Materials Science and Engineering*, 229(1):012021, sep 2017. doi: 10.1088/1757-899X/229/1/012021. URL https://dx.doi.org/10.1088/1757-899X/229/1/012021.

[83] M. Koizumi. Fgm activities in japan. *Composites Part B: Engineering*, 28(1):1–4, 1997. ISSN 1359-8368. doi: https://doi.org/10.1016/S1359-8368(96)00016-9. URL https://www.sciencedirect.com/science/article/pii/S1359836896000169.

[84] A. Koizumi. *Recent Progress of Functionally Gradient Materials in Japan*, chapter 33, pages 332–347. John Wiley & Sons, Ltd, 1994. ISBN 9780470313954. doi:

https://doi.org/10.1002/9780470313954.ch33. URL https://ceramics.onlinelibrary.wiley.com/doi/abs/10.1002/9780470313954.ch33.

[85] Masayuki Niino. Development of functionally gradient material. *Journal of the Japan Society of Powder and Powder Metallurgy*, 37(2):241–244, 1990. doi: 10.2497/jjspm.37.241.

[86] F. Ebrahimi. *Advances in Functionally Graded Materials and Structures*. IntechOpen, 2016. ISBN 9789535122746. URL https://books.google.dz/books?id=Nm-QDwAAQBAJ.

[87] M Yamanouchi, M Koizumi, T Hirai, and I Shiota. Proceedings of the first international symposium on functionally gradient materials. *Sendai, Japan*, 1990.

[88] H. Okamura. State of the art of material design projects for severe service applications. *Materials Science and Engineering: A*, 143(1):3–9, 1991. ISSN 0921-5093. doi: https://doi.org/10.1016/0921-5093(91)90720-8. URL https://www.sciencedirect.com/science/article/pii/0921509391907208. Structural Materials: Properties, Microstructure and Processing.

[89] B. Kieback, A. Neubrand, and H. Riedel. Processing techniques for functionally graded materials. *Materials Science and Engineering: A*, 362(1):81–106, 2003. ISSN 0921-5093. doi: https://doi.org/10.1016/S0921-5093(03)00578-1. URL https://www.sciencedirect.com/science/article/pii/S0921509303005781. Papers from the German Priority Programme (Functionally Graded Materials).

[90] Agata Strojny-Nędza, Katarzyna Pietrzak, Flavia Gili, and Marcin Chmielewski. Fgm based on copper–alumina composites for brake disc applications. *Archives of Civil and Mechanical Engineering*, 20(3):83, 2020. ISSN 2083-3318. doi: 10.1007/s43452-020-00079-1. URL https://doi.org/10.1007/s43452-020-00079-1.

[91] J. Aboudi, M. J. Pindera, and S. M. Arnold. Higher-order theory for functionally graded materials. *Composites Part B: Engineering*, 30(8):777–832, 1999. ISSN 1359-8368. doi: 10.1016/S1359-8368(99)00053-0. URL https://www.sciencedirect.com/science/article/pii/S1359836899000530.

[92] Debabrata Gayen and Tarapada Roy. Finite element based vibration analysis of functionally graded spinning shaft system. *Proceedings of the Institution of Mechanical Engineers, Part C: Journal of Mechanical Engineering Science*, 228(18):3306–3321, 2014. doi: 10.1177/0954406214527923. URL https://journals.sagepub.com/doi/abs/10.1177/0954406214527923.

[93] J. N. Reddy and C. D. Chin. Thermomechanical analysis of functionally graded cylinders and plates. *Journal of Thermal Stresses*, 21(6):593–626, 1998. ISSN 0149-5739. doi: 10.1080/01495739808956165. URL https://doi.org/10.1080/01495739808956165. doi: 10.1080/01495739808956165.

[94] Mohamad Khaje khabaz, S. Ali Eftekhari, Mohamad Hashemian, and Davood Toghraie.

Optimal vibration control of multi-layer micro-beams actuated by piezoelectric layer based on modified couple stress and surface stress elasticity theories. *Physica A: Statistical Mechanics and its Applications*, 546:123998, 2020. ISSN 0378-4371. doi: https://doi.org/10.1016/j.physa.2019.123998. URL https://www.sciencedirect.com/science/article/pii/S0378437119322137.

[95] Y. M. Ghugal and R. P. Shimpi. A review of refined shear deformation theories for isotropic and anisotropic laminated beams. *Journal of Reinforced Plastics and Composites*, 20(3): 255–272, 2001. doi: 10.1177/073168401772678283. URL https://doi.org/10.1177/073168401772678283.

[96] S.P. Timoshenko. Lxvi. on the correction for shear of the differential equation for transverse vibrations of prismatic bars. *The London, Edinburgh, and Dublin Philosophical Magazine and Journal of Science*, 41(245):744–746, 1921. doi: 10.1080/14786442108636264. URL https://doi.org/10.1080/14786442108636264.

[97] P.R. Heyliger and J.N. Reddy. A higher order beam finite element for bending and vibration problems. *Journal of Sound and Vibration*, 126(2):309–326, 1988. ISSN 0022-460X. doi: https://doi.org/10.1016/0022-460X(88)90244-1. URL https://www.sciencedirect.com/science/article/pii/0022460X88902441.

[98] M. Touratier. An efficient standard plate theory. *International Journal of Engineering Science*, 29(8):901–916, 1991. ISSN 0020-7225. doi: https://doi.org/10.1016/0020-7225(91)90165-Y. URL https://www.sciencedirect.com/science/article/pii/002072259190165Y.

[99] M. Karama, K.S. Afaq, and S. Mistou. Mechanical behaviour of laminated composite beam by the new multi-layered laminated composite structures model with transverse shear stress continuity. *International Journal of Solids and Structures*, 40(6):1525–1546, 2003. ISSN 0020-7683. doi: https://doi.org/10.1016/S0020-7683(02)00647-9. URL https://www.sciencedirect.com/science/article/pii/S0020768302006479.

[100] L. Euler and C. Caratheodory. *Methodus inveniendi lineas curvas maximi minimive proprietate gaudentes sive solutio problematis isoperimetrici latissimo sensu accepti*. Leonhard Euler, Opera Omnia / Opera mathematica. Birkhäuser Basel, 1952. ISBN 9783764314248. URL https://books.google.fr/books?id=zNDdVFZalSAC.

[101] J. N. Reddy. A simple higher-order theory for laminated composite plates. *Journal of Applied Mechanics*, 51(4):745–752, 12 1984. ISSN 0021-8936. doi: 10.1115/1.3167719. URL https://doi.org/10.1115/1.3167719.

[102] P. M. NAGHDI. On the theory of thin elastic shells. *Quarterly of Applied Mathematics*, 14(4): 369–380, 1957. ISSN 0033569X, 15524485. URL http://www.jstor.org/stable/43636014.

[103] N. D. Phan and J. N. Reddy. Analysis of laminated composite plates using a higher-order shear deformation theory. *International Journal for Numerical Methods in Engineering*, 21

(12):2201–2219, 1985. doi: https://doi.org/10.1002/nme.1620211207. URL https://onlinelibrary.wiley.com/doi/abs/10.1002/nme.1620211207.

[104] J. N. Reddy. Analysis of functionally graded plates. *International Journal for Numerical Methods in Engineering*, 47(1-3):663–684, 2000. doi: https://doi.org/10.1002/(SICI)1097-0207(20000110/30)47:1/3<663::AID-NME787>3.0.CO;2-8. URL https://onlinelibrary.wiley.com/doi/abs/10.1002/%28SICI%291097-0207%2820000110/30%2947%3A1/3%3C663%3A%3AAID-NME787%3E3.0.CO%3B2-8.

[105] J. N. Reddy. On refined theories of composite laminates. *Meccanica*, 25(4):230–238, 1990. ISSN 1572-9648. doi: 10.1007/BF01559685. URL https://doi.org/10.1007/BF01559685.

[106] Mallikarjuna and T. Kant. A critical review and some results of recently developed refined theories of fiber-reinforced laminated composites and sandwiches. *Composite Structures*, 23(4): 293–312, 1993. ISSN 0263-8223. doi: https://doi.org/10.1016/0263-8223(93)90230-N. URL https://www.sciencedirect.com/science/article/pii/026382239390230N.

[107] Eric Reissner. The effect of transverse shear deformation on the bending of elastic plates. *Journal of Applied Mechanics*, 12(2):A69–A77, 03 2021. ISSN 0021-8936. doi: 10.1115/1.4009435. URL https://doi.org/10.1115/1.4009435.

[108] R. D. Mindlin. Influence of rotatory inertia and shear on flexural motions of isotropic, elastic plates. *Journal of Applied Mechanics*, 18(1):31–38, 04 2021. ISSN 0021-8936. doi: 10.1115/1.4010217. URL https://doi.org/10.1115/1.4010217.

[109] J.N. Reddy. Nonlocal theories for bending, buckling and vibration of beams. *International Journal of Engineering Science*, 45(2):288–307, 2007. ISSN 0020-7225. doi: https://doi.org/10.1016/j.ijengsci.2007.04.004. URL https://www.sciencedirect.com/science/article/pii/S0020722507000377.

[110] Nuttawit Wattanasakulpong and Variddhi Ungbhakorn. Analytical solutions for bending, buckling and vibration responses of carbon nanotube-reinforced composite beams resting on elastic foundation. *Computational Materials Science*, 71:201–208, 2013. ISSN 0927-0256. doi: https://doi.org/10.1016/j.commatsci.2013.01.028. URL https://www.sciencedirect.com/science/article/pii/S0927025613000414.

[111] Seung-Eock Kim, Huu-Tai Thai, and Jaehong Lee. Buckling analysis of plates using the two variable refined plate theory. *Thin-Walled Structures*, 47(4):455–462, 2009. ISSN 0263-8231. doi: https://doi.org/10.1016/j.tws.2008.08.002. URL https://www.sciencedirect.com/science/article/pii/S0263823108001936.

[112] Huu-Tai Thai and Seung-Eock Kim. Free vibration of laminated composite plates using two variable refined plate theory. *International Journal of Mechanical Sciences*, 52(4):626–633, 2010. ISSN 0020-7403. doi: https://doi.org/10.1016/j.ijmecsci.2010.01.002. URL https://www.sciencedirect.com/science/article/pii/S0020740310000032.

[113] Huu-Tai Thai and Seung-Eock Kim. Levy-type solution for buckling analysis of orthotropic plates based on two variable refined plate theory. *Composite Structures*, 93(7):1738–1746, 2011. ISSN 0263-8223. doi: https://doi.org/10.1016/j.compstruct.2011.01.012. URL https://www.sciencedirect.com/science/article/pii/S0263822311000262.

[114] Huu-Tai Thai and Seung-Eock Kim. A simple quasi-3d sinusoidal shear deformation theory for functionally graded plates. *Composite Structures*, 99:172–180, 2013. ISSN 0263-8223. doi: https://doi.org/10.1016/j.compstruct.2012.11.030. URL https://www.sciencedirect.com/science/article/pii/S026382231200606X.

[115] Abdelouahed Tounsi, Mohammed Sid Ahmed Houari, Samir Benyoucef, and El Abbas Adda Bedia. A refined trigonometric shear deformation theory for thermoelastic bending of functionally graded sandwich plates. *Aerospace Science and Technology*, 24(1):209–220, 2013. ISSN 1270-9638. doi: https://doi.org/10.1016/j.ast.2011.11.009. URL https://www.sciencedirect.com/science/article/pii/S1270963811001945. VFE-2.

[116] S. R. Mahmoud Ahmed Hamidi Mohammed Sid Ahmed Houari and Tounsi Abdelouahed. A sinusoidal plate theory with 5-unknowns and stretching effect for thermomechanical bending of functionally graded sandwich plates. *Steel and Composite Structures*, 18(1):235–253, 2015. ISSN 1229-9367/1598-6233. doi: 10.12989/SCS.2015.18.1.235. URL https://doi.org/10.12989/SCS.2015.18.1.235.

[117] Huu-Tai Thai, Thuc P. Vo, Tinh Q. Bui, and Trung-Kien Nguyen. A quasi-3d hyperbolic shear deformation theory for functionally graded plates. *Acta Mechanica*, 225(3):951–964, 2014. ISSN 1619-6937. doi: 10.1007/s00707-013-0994-z. URL https://doi.org/10.1007/s00707-013-0994-z.

[118] Aicha Bessaim, Mohammed SA Houari, Abdelouahed Tounsi, SR Mahmoud, and El Abbes Adda Bedia. A new higher-order shear and normal deformation theory for the static and free vibration analysis of sandwich plates with functionally graded isotropic face sheets. *Journal of Sandwich Structures & Materials*, 15(6):671–703, 2013. doi: 10.1177/1099636213498888. URL https://doi.org/10.1177/1099636213498888.

[119] Mohammed Bennoun, Mohammed Sid Ahmed Houari, and Abdelouahed Tounsi. A novel five-variable refined plate theory for vibration analysis of functionally graded sandwich plates. *Mechanics of Advanced Materials and Structures*, 23(4):423–431, 2016. doi: 10.1080/15376494.2014.984088. URL https://doi.org/10.1080/15376494.2014.984088.

[120] Ashraf M. Zenkour. A simple four-unknown refined theory for bending analysis of functionally graded plates. *Applied Mathematical Modelling*, 37(20):9041–9051, 2013. ISSN 0307-904X. doi: https://doi.org/10.1016/j.apm.2013.04.022. URL https://www.sciencedirect.com/science/article/pii/S0307904X13002746.

[121] Ashraf M Zenkour. Bending analysis of functionally graded sandwich plates using a simple four-unknown shear and normal deformations theory. *Journal of Sandwich Structures &*

Materials, 15(6):629–656, 2013. doi: 10.1177/1099636213498886. URL https://doi.org/10.1177/1099636213498886.

[122] Ashraf M. Zenkour. Thermal bending of layered composite plates resting on elastic foundations using four-unknown shear and normal deformations theory. *Composite Structures*, 122:260–270, 2015. ISSN 0263-8223. doi: https://doi.org/10.1016/j.compstruct.2014.11.064. URL https://www.sciencedirect.com/science/article/pii/S026382231400645X.

[123] J.L. Mantari, E.V. Granados, M.A. Hinostroza, and C. Guedes Soares. Modelling advanced composite plates resting on elastic foundation by using a quasi-3d hybrid type hsdt. *Composite Structures*, 118:455–471, 2014. ISSN 0263-8223. doi: https://doi.org/10.1016/j.compstruct.2014.07.039. URL https://www.sciencedirect.com/science/article/pii/S0263822314003626.

[124] J. L. Mantari and C. Guedes Soares. A quasi-3d tangential shear deformation theory with four unknowns for functionally graded plates. *Acta Mechanica*, 226(3):625–642, 2015. ISSN 1619-6937. doi: 10.1007/s00707-014-1192-3. URL https://doi.org/10.1007/s00707-014-1192-3.

[125] F. Yang, A.C.M. Chong, D.C.C. Lam, and P. Tong. Couple stress based strain gradient theory for elasticity. *International Journal of Solids and Structures*, 39(10):2731–2743, 2002. ISSN 0020-7683. doi: https://doi.org/10.1016/S0020-7683(02)00152-X. URL https://www.sciencedirect.com/science/article/pii/S002076830200152X.

[126] R. D. Mindlin and H. F. Tiersten. Effects of couple-stresses in linear elasticity. *Archive for Rational Mechanics and Analysis*, 11(1):415–448, 1962. ISSN 1432-0673. doi: 10.1007/BF00253946. URL https://doi.org/10.1007/BF00253946.

[127] Warner T. Koiter. Couple-stresses in the theory of elasticity, i & ii. 1969. URL https://api.semanticscholar.org/CorpusID:123837588.

[128] Amir Mehdi Dehrouyeh-Semnani and Mansour Nikkhah-Bahrami. A discussion on evaluation of material length scale parameter based on micro-cantilever test. *Composite Structures*, 122: 425–429, 2015. ISSN 0263-8223. doi: https://doi.org/10.1016/j.compstruct.2014.11.054. URL https://www.sciencedirect.com/science/article/pii/S0263822314006357.

[129] F Khajueenejad and J Ghanbari. Internal length parameter and buckling analysis of carbon nanotubes using modified couple stress theory and timoshenko beam model. *Materials Research Express*, 2(10):105009, oct 2015. doi: 10.1088/2053-1591/2/10/105009. URL https://dx.doi.org/10.1088/2053-1591/2/10/105009.

[130] S K Park and X-L Gao. Bernoulli–euler beam model based on a modified couple stress theory. *Journal of Micromechanics and Microengineering*, 16(11):2355, sep 2006. doi: 10.1088/0960-1317/16/11/015. URL https://dx.doi.org/10.1088/0960-1317/16/11/015.

[131] S. Kong, S. Zhou, Z. Nie, and K. Wang. The size-dependent natural frequency of

bernoulli–euler microbeams. *International Journal of Engineering Science*, 46:427–437, 2008. doi: 10.1016/j.ijengsci.2007.09.005.

[132] S. Kong, S. Zhou, Z. Nie, and K. Wang. Size effect on the buckling loads of slender columns based on a modified couple stress theory. *Journal of Mechanical Strength*, 31:136–139, 2009. URL https://en.cnki.com.cn/Article_en/CJFDTotal-JXXQ200901032.htm.

[133] W. Xia, L. Wang, and L. Yin. Nonlinear non-classical microscale beams: Static bending, postbuckling and free vibration. *International Journal of Engineering Science*, 48:2044–2053, 2010. doi: 10.1016/j.ijengsci.2010.04.010.

[134] M. Simsek. Nonlinear static and free vibration analysis of microbeams based on the nonlinear elastic foundation using modified couple stress theory and he's variational method. *Composite Structures*, 112:264–272, 2014. doi: 10.1016/j.compstruct.2014.02.014.

[135] H. Farokhi, M.H. Ghayesh, and M. Amabili. Nonlinear dynamics of a geometrically imperfect microbeam based on the modified couple stress theory. *International Journal of Engineering Science*, 68:11–23, 2013. doi: 10.1016/j.ijengsci.2013.03.003.

[136] N. Togun and S.M. Bagdatli. Size dependent nonlinear vibration of the tensioned nanobeam based on the modified couple stress theory. *Composites Part B: Engineering*, 97:255–262, 2016. doi: 10.1016/j.compositesb.2016.04.074.

[137] Y.G. Wang, W.H. Lin, and N. Liu. Nonlinear bending and post-buckling of extensible microscale beams based on modified couple stress theory. *Applied Mathematical Modelling*, 39: 117–127, 2015. doi: 10.1016/j.apm.2014.05.001.

[138] Y.G. Wang, W.H. Lin, C.L. Zhou, and R.X. Liu. Thermal postbuckling and free vibration of extensible microscale beams based on modified couple stress theory. *Journal of Mechanics*, 31: 37–46, 2014. doi: 10.1017/jmech.2014.47.

[139] R. Ansari, M.A. Ashrafi, and A. Arjangpay. An exact solution for vibrations of postbuckled microscale beams based on the modified couple stress theory. *Applied Mathematical Modelling*, 39:3050–3062, 2015. doi: 10.1016/j.apm.2014.11.029.

[140] M. Asghari, M.T. Ahmadian, M.H. Kahrobaiyan, and M. Rahaeifard. On the size-dependent behavior of functionally graded micro-beams. *Materials & Design*, 31:2324–2329, 2010. doi: 10.1016/j.matdes.2009.12.006.

[141] B. Akgoz and O. Civalek. Free vibration analysis of axially functionally graded tapered bernoulli-euler microbeams based on the modified couple stress theory. *Composite Structures*, 98:314–322, 2013. doi: 10.1016/j.compstruct.2012.11.020.

[142] N. Shafiei, M. Kazemi, and M. Ghadiri. Nonlinear vibration of axially functionally graded tapered microbeams. *International Journal of Engineering Science*, 102:12–26, 2016. doi: 10.1016/j.ijengsci.2016.02.007.

[143] M. Simsek. Size dependent nonlinear free vibration of an axially functionally graded (afg) microbeam using he's variational method. *Composite Structures*, 131:207–214, 2015. doi: 10.1016/j.compstruct.2015.05.011.

[144] A.M. Dehrouyeh-Semnani, H. Mostafaei, and M. Nikkhah-Bahrami. Free flexural vibration of geometrically imperfect functionally graded microbeams. *International Journal of Engineering Science*, 105:56–79, 2016. doi: 10.1016/j.ijengsci.2016.05.002.

[145] H.M. Ma, X.L. Gao, and J.N. Reddy. A microstructure-dependent timoshenko beam model based on a modified couple stress theory. *Journal of the Mechanics and Physics of Solids*, 56: 3379–3391, 2008. doi: 10.1016/j.jmps.2008.09.007.

[146] M. Asghari, M.H. Kahrobaiyan, M. Rahaeifard, and M.T. Ahmadian. Investigation of the size effects in timoshenko beams based on the couple stress theory. *Archive of Applied Mechanics*, 81:863–874, 2011. doi: 10.1007/s00419-010-0452-5.

[147] J.V.A. Dos Santos and J.N. Reddy. Free vibration and buckling analysis of beams with a modified couple stress theory. *International Journal of Applied Mechanics*, 4(2):1250026, 2012. doi: 10.1142/S175882511250026X.

[148] A.M. Dehrouyeh-Semnani and M. Nikkhah-Bahrami. A discussion on incorporating the poisson effect in microbeam models based on modified couple stress theory. *International Journal of Engineering Science*, 86:20–25, 2015. doi: 10.1016/j.ijengsci.2014.10.003.

[149] Y.P. Liu and J.N. Reddy. A nonlocal curved beam model based on a modified couple stress theory. *International Journal of Structural Stability and Dynamics*, 11:495–512, 2011. doi: 10.1142/S021945541100416X.

[150] E. Taati, M. Molaei Najafabadi, and H. Basirat Tabrizi. Size-dependent generalized thermoelasticity model for timoshenko microbeams. *Acta Mechanica*, 225:1823–1842, 2014. doi: 10.1007/s00707-013-1011-4.

[151] M. Asghari, M.H. Kahrobaiyan, and M.T. Ahmadian. A nonlinear timoshenko beam formulation based on the modified couple stress theory. *International Journal of Engineering Science*, 48:1749–1761, 2010. doi: 10.1016/j.ijengsci.2010.09.028.

[152] M.H. Ghayesh, H. Farokhi, and M. Amabili. Nonlinear dynamics of a microscale beam based on the modified couple stress theory. *Composites Part B: Engineering*, 50:318–324, 2013. doi: 10.1016/j.compositesb.2013.02.021.

[153] M.H. Ghayesh, M. Amabili, and H. Farokhi. Three-dimensional nonlinear size-dependent behaviour of timoshenko microbeams. *International Journal of Engineering Science*, 71:1–14, 2013. doi: 10.1016/j.ijengsci.2013.04.003.

[154] J.N. Reddy. Microstructure-dependent couple stress theories of functionally graded beams. *Journal of the Mechanics and Physics of Solids*, 59:2382–2399, 2011. doi: 10.1016/j.jmps.2011.06.008.

[155] L.L. Ke, Y.S. Wang, J. Yang, and S. Kitipornchai. Nonlinear free vibration of size-dependent functionally graded microbeams. *International Journal of Engineering Science*, 50:256–267, 2012. doi: 10.1016/j.ijengsci.2010.12.006.

[156] M. Asghari, M. Rahaeifard, M.H. Kahrobaiyan, and M.T. Ahmadian. The modified couple stress functionally graded timoshenko beam formulation. *Materials & Design*, 32:1435–1443, 2011. doi: 10.1016/j.matdes.2010.08.046.

[157] L.L. Ke and Y.S. Wang. Size effect on dynamic stability of functionally graded microbeams based on a modified couple stress theory. *Composite Structures*, 93:342–350, 2011. doi: 10.1016/j.compstruct.2010.09.008.

[158] A. Nateghi and M. Salamat-talab. Thermal effect on size dependent behavior of functionally graded microbeams based on modified couple stress theory. *Composite Structures*, 96:97–110, 2013. doi: 10.1016/j.compstruct.2012.12.009.

[159] M. Şimşek, T. Kocatürk, and Ş.D. Akbaş. Static bending of a functionally graded microscale timoshenko beam based on the modified couple stress theory. *Composite Structures*, 95: 740–747, 2013. doi: 10.1016/j.compstruct.2012.08.016.

[160] W. Chen, L. Li, and M. Xu. A modified couple stress model for bending analysis of composite laminated beams with first order shear deformation. *Composite Structures*, 93(11):2723–2732, 2011. doi: 10.1016/j.compstruct.2011.05.032.

[161] W.J. Chen and X.P. Li. Size-dependent free vibration analysis of composite laminated timoshenko beam based on new modified couple stress theory. *Archive of Applied Mechanics*, 83:431–444, 2013. doi: 10.1007/s00419-012-0689-2.

[162] C.M.C. Roque, D.S. Fidalgo, A.J.M. Ferreira, and J.N. Reddy. A study of a microstructure-dependent composite laminated timoshenko beam using a modified couple stress theory and a meshless method. *Composite Structures*, 96:532–537, 2013. doi: 10.1016/j.compstruct.2012.09.011.

[163] M. Mohammad-Abadi and A.R. Daneshmehr. An investigation of modified couple stress theory in buckling analysis of micro composite laminated euler–bernoulli and timoshenko beams. *International Journal of Engineering Science*, 75:40–53, 2014. doi: 10.1016/j.ijengsci.2013.11.009.

[164] H.T. Thai, T.P. Vo, T.K. Nguyen, and J. Lee. Size-dependent behavior of functionally graded sandwich microbeams based on the modified couple stress theory. *Composite Structures*, 123: 337–349, 2015. doi: 10.1016/j.compstruct.2014.11.065.

[165] A.V. Krysko, J. Awrejcewicz, S.P. Pavlov, M.V. Zhigalov, and V.A. Krysko. Mathematical model of a three-layer micro- and nano-beams based on the hypotheses of the grigolyuk-chulkov and the modified couple stress theory. *International Journal of Solids and Structures*, 117:39–50, 2017. doi: 10.1016/j.ijsolstr.2017.04.011.

[166] H.M. Ma, X.L. Gao, and J.N. Reddy. A nonclassical reddy-levinson beam model based on a modified couple stress theory. *International Journal of Multiscale Computational Engineering*, 8(2):167–180, 2010. doi: 10.1615/IntJMultCompEng.v8.i2.30.

[167] M. Mohammad-Abadi and A.R. Daneshmehr. Size dependent buckling analysis of microbeams based on modified couple stress theory with high order theories and general boundary conditions. *International Journal of Engineering Science*, 74:1–14, 2014. doi: 10.1016/j.ijengsci.2013.08.010.

[168] M. Salamat-talab, A. Nateghi, and J. Torabi. Static and dynamic analysis of third-order shear deformation fg micro beam based on modified couple stress theory. *International Journal of Mechanical Sciences*, 57:63–73, 2012. doi: 10.1016/j.ijmecsci.2012.02.004.

[169] A. Nateghi, M. Salamat-talab, J. Rezapour, and B. Daneshian. Size dependent buckling analysis of functionally graded micro beams based on modified couple stress theory. *Applied Mathematical Modelling*, 36:4971–4987, 2012. doi: 10.1016/j.apm.2011.12.035.

[170] R. Aghazadeh, E. Cigeroglu, and S. Dag. Static and free vibration analyses of small-scale functionally graded beams possessing a variable length scale parameter using different beam theories. *European Journal of Mechanics - A/Solids*, 46:1–11, 2014. doi: 10.1016/j.euromechsol.2014.01.002.

[171] W. Chen, W. Chen, and K.Y. Sze. A model of composite laminated reddy beam based on a modified couplestress theory. *Composite Structures*, 94:2599–2609, 2012. doi: 10.1016/j.compstruct.2012.02.020.

[172] M. Mohammad-Abadi and A.R. Daneshmehr. Modified couple stress theory applied to dynamic analysis of composite laminated beams by considering different beam theories. *International Journal of Engineering Science*, 87:83–102, 2015. doi: 10.1016/j.ijengsci.2014.11.003.

[173] M. Mohammad-Abadi, A.R. Daneshmehr, and M. Homayounfard. Size-dependent thermal buckling analysis of micro composite laminated beams using modified couple stress theory. *International Journal of Engineering Science*, 92:47–62, 2015. doi: 10.1016/j.ijengsci.2015.03.005.

[174] H. Darijani and H. Mohammadabadi. A new deformation beam theory for static and dynamic analysis of microbeams. *International Journal of Mechanical Sciences*, 89:31–39, 2014. doi: 10.1016/j.ijmecsci.2014.08.019.

[175] J. Noori, S.J. Fariborz, and J.P. Vafa. A higher-order micro-beam model with application to free vibration. *Mechanics of Advanced Materials and Structures*, 23:443–450, 2016. doi: 10.1080/15376494.2014.984090.

[176] M. Simsek and J.N. Reddy. Bending and vibration of functionally graded microbeams using a

new higher order beam theory and the modified couple stress theory. *International Journal of Engineering Science*, 64:37–53, 2013. doi: 10.1016/j.ijengsci.2012.12.002.

[177] K. P. Soldatos. A transverse shear deformation theory for homogeneous monoclinic plates. *Acta Mechanica*, 94(3):195–220, 1992. ISSN 1619-6937. doi: 10.1007/BF01176650. URL https://doi.org/10.1007/BF01176650.

[178] M. Karama, K.S. Afaq, and S. Mistou. Mechanical behaviour of laminated composite beam by the new multi-layered laminated composite structures model with transverse shear stress continuity. *International Journal of Solids and Structures*, 40(6):1525–1546, 2003. ISSN 0020-7683. doi: https://doi.org/10.1016/S0020-7683(02)00647-9. URL https://www.sciencedirect.com/science/article/pii/S0020768302006479.

[179] Metin Aydogdu. A new shear deformation theory for laminated composite plates. *Composite Structures*, 89(1):94–101, 2009. ISSN 0263-8223. doi: https://doi.org/10.1016/j.compstruct.2008.07.008. URL https://www.sciencedirect.com/science/article/pii/S0263822308002420.

[180] M. Simsek and J.N. Reddy. A unified higher order beam theory for buckling of a functionally graded microbeam embedded in elastic medium using modified couple stress theory. *Composite Structures*, 101:47–58, 2013. doi: 10.1016/j.compstruct.2013.01.017.

[181] M. Akbarzadeh Khorshidi, M. Shariati, and S.A. Emam. Postbuckling of functionally graded nanobeams based on modified couple stress theory under general beam theory. *International Journal of Mechanical Sciences*, 110:160–169, 2016. doi: 10.1016/j.ijmecsci.2016.03.006.

[182] L.C. Trinh, H.X. Nguyen, T.P. Vo, and T-K. Nguyen. Size-dependent behaviour of functionally graded microbeams using various shear deformation theories based on the modified couple stress theory. *Composite Structures*, 154:556–572, 2016. doi: 10.1016/j.compstruct.2016.07.033.

[183] B. Akgoz and O. Civalek. Thermo-mechanical buckling behavior of functionally graded microbeams embedded in elastic medium. *International Journal of Engineering Science*, 85: 90–104, 2014. doi: 10.1016/j.ijengsci.2014.08.011.

[184] Rameshchandra P. Shimpi. Refined plate theory and its variants. *AIAA Journal*, 40(1): 137–146, 2002. doi: 10.2514/2.1622. URL https://doi.org/10.2514/2.1622.

[185] Huu-Tai Thai and Dong-Ho Choi. Efficient higher-order shear deformation theories for bending and free vibration analyses of functionally graded plates. *Archive of Applied Mechanics*, 83(12):1755–1771, 2013. ISSN 1432-0681. doi: 10.1007/s00419-013-0776-z. URL https://doi.org/10.1007/s00419-013-0776-z.

[186] Huu-Tai Thai and Thuc P. Vo. A new sinusoidal shear deformation theory for bending, buckling, and vibration of functionally graded plates. *Applied Mathematical Modelling*, 37(5): 3269–3281, 2013. ISSN 0307-904X. doi: https://doi.org/10.1016/j.apm.2012.08.008. URL https://www.sciencedirect.com/science/article/pii/S0307904X12004647.

[187] H. Darijani and A. H. Shahdadi. A new shear deformation model with modified couple stress theory for microplates. *Acta Mechanica*, 226(8):2773–2788, 2015. ISSN 1619-6937. doi: 10.1007/s00707-015-1338-y. URL https://doi.org/10.1007/s00707-015-1338-y.

[188] Song Xiang, Yao xing Jin, Ze yang Bi, Shao xi Jiang, and Ming sui Yang. A n-order shear deformation theory for free vibration of functionally graded and composite sandwich plates. *Composite Structures*, 93(11):2826–2832, 2011. ISSN 0263-8223. doi: https://doi.org/10.1016/j.compstruct.2011.05.022. URL https://www.sciencedirect.com/science/article/pii/S0263822311001954.

[189] Mohammed Sobhy and Ahmed F. Radwan. A new quasi 3d nonlocal plate theory for vibration and buckling of fgm nanoplates. *International Journal of Applied Mechanics*, 09(01):1750008, 2017. doi: 10.1142/S1758825117500089. URL https://doi.org/10.1142/S1758825117500089.

[190] Jian Lei, Yuming He, Bo Zhang, Dabiao Liu, Lei Shen, and Song Guo. A size-dependent fg micro-plate model incorporating higher-order shear and normal deformation effects based on a modified couple stress theory. *International Journal of Mechanical Sciences*, 104:8–23, 2015. ISSN 0020-7403. doi: https://doi.org/10.1016/j.ijmecsci.2015.09.016. URL https://www.sciencedirect.com/science/article/pii/S0020740315003434.

[191] Luan C. Trinh, Thuc P. Vo, Huu-Tai Thai, and J.L. Mantari. Size-dependent behaviour of functionally graded sandwich microplates under mechanical and thermal loads. *Composites Part B: Engineering*, 124:218–241, 2017. ISSN 1359-8368. doi: https://doi.org/10.1016/j.compositesb.2017.05.042. URL https://www.sciencedirect.com/science/article/pii/S1359836817304158.

[192] J.N. Reddy and Jinseok Kim. A nonlinear modified couple stress-based third-order theory of functionally graded plates. *Composite Structures*, 94(3):1128–1143, 2012. ISSN 0263-8223. doi: https://doi.org/10.1016/j.compstruct.2011.10.006. URL https://www.sciencedirect.com/science/article/pii/S0263822311003692.

[193] Ngoc-Tuan Nguyen, David Hui, Jaehong Lee, and H. Nguyen-Xuan. An efficient computational approach for size-dependent analysis of functionally graded nanoplates. *Computer Methods in Applied Mechanics and Engineering*, 297:191–218, 2015. ISSN 0045-7825. doi: https://doi.org/10.1016/j.cma.2015.07.021. URL https://www.sciencedirect.com/science/article/pii/S004578251500239X.

[194] G. Y. Zhang, X. L. Gao, and Z. Y. Guo. A non-classical model for an orthotropic kirchhoff plate embedded in a viscoelastic medium. *Acta Mechanica*, 228(11):3811–3825, 2017. ISSN 1619-6937. doi: 10.1007/s00707-017-1906-4. URL https://doi.org/10.1007/s00707-017-1906-4.

[195] Thuc P. Vo, Huu-Tai Thai, Trung-Kien Nguyen, Alireza Maheri, and Jaehong Lee. Finite element model for vibration and buckling of functionally graded sandwich beams based on a refined shear deformation theory. *Engineering Structures*, 64:12–22, 2014. ISSN 0141-0296.

doi: https://doi.org/10.1016/j.engstruct.2014.01.029. URL https://www.sciencedirect.com/science/article/pii/S0141029614000431.

[196] Ahmed Amine Daikh, Mohamed-Ouejdi Belarbi, Abdelhak Khechai, Li Li, Hani M. Ahmed, and Mohamed A. Eltaher. Buckling of bi-coated functionally graded porous nanoplates via a nonlocal strain gradient quasi-3d theory. *Acta Mechanica*, 234(8):3397–3420, 2023. ISSN 1619-6937. doi: 10.1007/s00707-023-03548-9. URL https://doi.org/10.1007/s00707-023-03548-9.

[197] Jiang Yu Li. Magnetoelectroelastic multi-inclusion and inhomogeneity problems and their applications in composite materials. *International Journal of Engineering Science*, 38(18): 1993–2011, 2000. ISSN 0020-7225. doi: https://doi.org/10.1016/S0020-7225(00)00014-8. URL https://www.sciencedirect.com/science/article/pii/S0020722500000148.

[198] G. Y. Zhang and X. L. Gao. Elastic wave propagation in 3-d periodic composites: Band gaps incorporating microstructure effects. *Composite Structures*, 204:920–932, 2018. ISSN 0263-8223. doi: https://doi.org/10.1016/j.compstruct.2018.07.115. URL https://www.sciencedirect.com/science/article/pii/S0263822318318270.

Abstract

This thesis investigates the static bending and free vibration of functionally graded magneto-electro-elastic (FG-MEE) microbeams in sandwich, coated, and bi-coated forms. Refined higher-order and quasi-3D beam theories are combined with the Differential Quadrature Finite Element Method (DQ-FEM) to capture electromechanical coupling. Material gradation is modeled by a power-law distribution, ensuring smooth property transitions between MEE and non-MEE layers. The Modified Couple Stress Theory (MCST) is incorporated to account for size-dependent effects, and governing equations are derived via Lagrange's theorem and Gauss–Lobatto discretization. Validation with published results confirms the model's accuracy and efficiency. Results show that material composition, gradation index, and geometry strongly affect static and dynamic responses. Increasing $BaTiO_3$ enhances piezoelectric deflection, while $CoFe_2O_4$ strengthens magnetostrictive effects. Higher gradation indices and slenderness ratios increase stiffness but reduce electromechanical potentials. Natural frequencies are highly sensitive to boundary conditions. The framework offers an efficient tool for optimizing FG-MEE microbeams in smart microsystems.

keywords: FGMs; magneto-electro-elastic microbeams; higher-order beam theories; MCST; DQ-FEM.

مُلخّص

تتناول هذه الأطروحة دراسة الانحناء الساكن والاهتزاز الحر للعتبات الميكروية المصنوعة من مواد مغناطوكهربومرنة متدرجة وظيفياً (FG-MEE) في تكوينات مختلفة: مركبة، مطلية، ومزدوجة الطلاء. تم اعتماد نظريات متقدمة من الرتبة العليا ونظريات شبه ثلاثية الأبعاد (quasi-3D) مدمجة بطريقة العناصر المتنهية (DQ-FEM) لنمذجة السلوك الكهروميكانيكي. تم تمثيل تدرج المواد وفق قانون القوة لضمان انتقال سلس بين الطبقات، وأُخذت في الاعتبار تأثيرات الحجم باستخدام نظرية إجهاد العزم المعدلة (بِضعة). اشتقت المعادلات عبر مبرهنة لاغرانج ونقاط غاوسلوبيتو، وتم التحقق من صحة النموذج بمقارنة نتائجه مع الأدبيات. أظهرت النتائج أن تركيب المواد، معامل التدرج، والهندسة تؤثر بشكل كبير على الاستجابات. زيادة ($BaTiO_3$) تحسن التأثير الكهروضغطي، بينما يعزز ($CoFe_2O_4$) التأثير المغناطيسي. ارتفاع معامل التدرج يزيد من الصلابة لكنه يقلل من الاستجابات الكهرومغناطيسية. كما أن الترددات الطبيعية شديدة الحساسية للظروف الحدية. يوفر هذا الإطار أداة فعالة لتحسين العتبات الميكروية (FG-MEE) .

الكلمات المفتاحيّة: المواد المتدرجة وظيفياً (FGM) ؛ العوارض الميكروية الكهرومغناطيسية المرنة؛ نظريات العوارض من الرتبة العليا؛ (MCST) ؛ (DQ-FEM) .

Résumé

Cette thèse analyse le flambement statique et les vibrations libres de micro-poutres magnéto-électro-élastiques (FG-MEE) en configurations sandwich, revêtues et bi-revêtues. Des théories de poutres d'ordre supérieur et quasi-3D sont combinées à la méthode DQ-FEM pour modéliser le couplage électromécanique. La gradation est décrite par une loi puissance assurant une transition continue entre matériaux MEE et non-MEE. La théorie des contraintes de couple modifiée (MCST) intègre les effets de taille, et les équations gouvernantes sont établies via le théorème de Lagrange et la discrétisation de Gauss–Lobatto. La validation confirme la précision et l'efficacité du modèle. Les résultats montrent que la composition, l'indice de gradation et la géométrie influencent fortement la réponse. L'augmentation du $BaTiO_3$ amplifie la flexibilité piézoélectrique, tandis que $CoFe_2O_4$ renforce les effets magnétostrictifs. Des indices plus élevés accroissent la rigidité mais réduisent les potentiels électromagnétiques. Les fréquences naturelles sont sensibles aux conditions aux limites. Ce cadre offre un outil efficace pour optimiser les microstructures FG-MEE.

mots-clés: FGM ; micro-poutres magnéto-électro-élastiques ; théories de poutres d'ordre supérieur ; MCST ; DQ-FEM.